

UNIVERSITÉ DE STRASBOURG
ISIS
Laboratoire des Nanostructures

FUNDAMENTAL ASPECTS OF THE ENHANCED
TRANSMISSION PHENOMENON AND ITS APPLICATION
TO PHOTON SORTING

Thèse présentée pour obtenir le grade de
Docteur de l'Université de Strasbourg
Discipline: Physique

par

Eric Laux

Soutenue le 7 Avril 2009 devant la commission d'examen composée de :

PR. MARTÍN-MORENO	L.	Universidad de Zaragoza	Président
DR. FORT	A.	CNRS, Strasbourg	Rapporteur interne
PR. ZAYATS	A.	Queen's University, Belfast	Rapporteur externe
DR. STANLEY	R.	CSEM, Neuchâtel	Rapporteur externe
DR. GENET	C.	CNRS, Strasbourg	Membre invité
PR. EBBESEN	T.W.	Université de Strasbourg	Directeur de Thèse

Résumé

La question de la transmission de la lumière à travers une ouverture est une des plus fondamentales en optique. Il y a environ dix ans, notre compréhension de ce phénomène a été fortement remise en cause par la découverte de la transmission extraordinaire à travers des ouvertures sublongueurs d'onde. En effet, bien que la propagation des ondes lumineuses à travers de telles ouvertures de tailles réduites soit proscrite, leur mise en réseau périodique a fait apparaître des pics très intenses dans le spectre de transmission. Ce phénomène a été associé à l'excitation de modes de plasmons de surface. Ces modes sont des oscillations collectives d'électrons libres et permettent la concentration de l'énergie électromagnétique dans des dimensions réduites. L'intérêt que l'on porte à des structures qui présentent de telles caractéristiques est également motivé par des applications dans les domaines tel que le filtrage optique, les sondes moléculaires, ou encore leur intégration dans des composants optiques ou optoélectroniques.

Le présent travail s'inscrit dans cette continuité et propose une étude approfondie de certaines propriétés fondamentales de la transmission extraordinaire. Ce travail présente en outre une nouvelle application fondée sur le développement de structures plasmoniques permettant le triage de photons.

Les premiers chapitres sont dédiés à l'introduction de différentes notions clés par rapport aux plasmons de surface, aux réseaux de trous et aux trous individuels et décrivent la démarche expérimentale.

Dans le chapitre 5, nous avons étudié la transmission des réseaux de trous sublongueurs d'onde fabriqués au laboratoire à l'aide d'un faisceau à ions focalisés (FIB) pour comprendre l'influence de certains paramètres structuraux. Si l'influence de la

périodicité et de la symétrie est bien établie aujourd'hui, notre étude a mis l'accent sur le facteur de remplissage d'un réseau pour différentes profondeurs de trous (relation entre transmission et diamètre du trou). Un intérêt particulier est porté à la transition qui a lieu quand le trou devient suffisamment grand pour guider des modes optiques propagatifs. Les résultats sont analysés avec la théorie classique des guides d'onde et avec une approche qui tient compte de l'interaction entre le canal de transmission directe et le canal résonant lié à l'excitation d'un mode plasmon. Notre étude permet de déduire que dans le contexte de la transmission exalté à travers des réseaux de trous, la fréquence de coupure intervient pour des trous nettement plus petits que ce qui est prévu par la théorie électromagnétique des guides d'onde. En plus, cette transition induit des changements importants des différentes caractéristiques associées à la transmission comme la position ou la largeur de la résonance. La condition optimale pour exciter les plasmons est aussi associé à cette transition ce qui a des implications importantes pour différentes applications.

Dans le chapitre 6, on s'intéresse au phénomène de diffraction dans le contexte de trous sub-longueurs d'onde dans un métal réel. Cette étude est motivée par des résultats expérimentaux récents qui indiquent que les figures de diffraction de telles structures dévient fortement des prévisions classiques. Afin de vérifier ces indications en détail, un montage expérimental dédié à la caractérisation précise du processus de diffraction à travers des trous aussi petits a été réalisé. Ce montage expérimental est présenté en détail avec le programme Labview qui contrôle l'acquisition automatisée des mesures. Etant donné le temps investi dans la mise en place du dispositif expérimental, il n'a pas été possible de réaliser toutes les mesures prévues. Par conséquent seuls des résultats préliminaires sont présentés. Néanmoins ces mesures confirment déjà les déviations prévues par rapport aux modèles classiques qui traitent les ouvertures uniques. En plus l'influence de la polarisation est mise en évidence sur les figures de diffraction de structures appelées " cibles " constituées de trous uniques entourés de sillons périodiques. Une discussion des différents paramètres qui peuvent influencer la diffraction et des mesures prévues nécessaires pour aboutir à une compréhension précise de ce phénomène clôt le chapitre.

Le chapitre 7 s'intéresse au problème de l'imagerie spectrale et polarimétrique,

c.à.d. aux systèmes qui permettent d'avoir accès à une information spectrale ou polarimétrique à partir de détecteurs CCD. La solution spectrale habituelle repose sur l'utilisation de mosaïques de filtres (filtre " Bayer ") qui permettent d'acquérir différentes gammes spectrales sur des pixels adjacents. Ceci est loin d'être un système parfait étant donné les problèmes de registre et de résolution qui en découlent.

Notre approche veut profiter des propriétés d'antenne et de filtrage de structures composées d'ouvertures uniques entourées de corrugations périodiques. Le but est de fabriquer une structure qui soit en un même endroit sensible à plusieurs longueurs d'onde, ce qu'on réalise en entrelaçant 3 réseaux périodiques, dont chacun est sensible à une gamme de longueur d'onde différente. A chaque structure est associée une ouverture qui transmet la lumière collectée pour un des réseaux entrelacés. En mesurant ainsi la lumière transmise par les ouvertures associées à chaque réseau, on peut évaluer la capacité de ces structures à séparer les photons de différentes longueurs d'onde.

On a pu observer que cette capacité reste largement intacte en fonction du taux de recouvrement, sauf dans la limite des très forts recouvrements. Dans une seconde étape des structures ont été préparées où l'élément de base n'est plus une cible, mais une fente avec des sillons linéaires. Cette architecture est intéressante, car chaque filtre devient également sensible à la polarisation. On a pu démontrer qu'il est possible de trier les photons à la fois suivant la polarisation et suivant 3 gammes spectrales qui peuvent être ajustées individuellement. Les efficacités observées sont de l'ordre de 10 à 15% dépendant des longueurs d'onde et des différents paramètres structuraux. Elles sont certes en-dessous de ce qui est atteint avec des systèmes existants (25%), mais notre approche montre clairement le potentiel des structures plasmoniques, surtout si l'on étend le concept dans le domaine de l'infrarouge où les longueurs de propagations des PS sont plus élevées et les intensités des pics de transmission probablement plus intenses.

Acknowledgements

First of all I would like to thank Thomas Ebbesen for giving me the opportunity to join the Laboratory of Nanostructures. I am very grateful for his advice and guidance that enabled me to grow on a scientific and on a personal level.

I would also like to express my gratitude towards Cyriaque Genet for his availability and his precious advice that was invaluable during these years.

I also address my acknowledgments to Anatoly Zayats, Ross Stanley, Luis Martín-Moreno and Alain Fort for accepting to be members of my thesis jury and for the interest they showed in my work.

I would also like to thank all the participants of the PLEAS project for all the interesting and stimulating discussions, in particular the groups of Pr. Zayats, Dr. Stanley, Pr. García-Vidal, Pr. Martín-Moreno, Pr. Eng and the industrial partners from SAGEM and OSRAM. I would also like to specifically thank Andrea Dunbar, Mickaël Guillaume and Ross Stanley for their hospitality during my stay at CSEM Neuchâtel.

I thank Torbjørn Skauli from FFI for the interesting collaboration that resulted in the idea of using plasmonic structures for photon sorting.

Besides I cannot forget to mention the help of Frédéric Przybilla and Jean-Yves Laluet who took me under their wings when I arrived in the laboratory 4 years ago.

I am also very grateful for all the help that was provided by Eloïse Devaux, José Dintinger, Aurélien Drezet and Marie-Claude Jouaiti. Together with Ous-

Acknowledgements

sama Mahboub, Yantao Pang, Adi Salomon, Emmanuel Lombard, Tal Schwartz, Benedikt Stein and Juemin Yi, they generated the nice and stimulating atmosphere in the laboratory during all those years. A big thank also goes out to all the other people of ISIS that I had the chance to meet and get to know.

I would also like to thank all my friends and my family, in particular my girlfriend Michelle for all the support during this chapter of my life.

Contents

1	Introduction: “nano?”	1
2	Surface plasmons	11
2.1	Definition of surface plasmons	11
2.2	Condition of existence of surface plasmons	11
2.3	The dispersion relation of surface plasmons in a real metal	14
2.4	Energy confinement and propagation length of the SPs	16
2.5	How to excite SPs	18
2.5.1	Coupling using Attenuated Total Reflection	18
2.5.2	Grating coupling	21
2.6	Localized surface plasmons	21
3	The transmission of light through small holes	25
3.1	Classical theories on the transmission of light through single apertures: The Fraunhofer-Fresnel diffraction and the Bethe model	25
3.2	Coupling light to surface plasmons with hole arrays	28
3.3	Other parameters influencing the transmission	34
4	Description of the experimental procedures	37
4.1	Preparing the metal films	37
4.2	Nanostructuring using FIB	38
4.3	Acquisition of transmission spectra	40
5	Enhanced optical transmission at the cutoff transition	47
5.1	Optical characterization of hole arrays	48
5.2	The nanohole as a waveguide	51
5.3	Fano analysis	54

5.4	Conclusion	61
6	Diffraction of single apertures in a real metal	63
6.1	The experimental setup	65
6.1.1	The optics	66
6.1.2	Automatizing the acquisition process	67
6.1.3	Validation of the equipment	69
6.2	Towards the study of single subwavelength apertures	71
6.2.1	Spectral characterization	71
6.2.2	First experimental measurements of diffraction	73
7	Plasmonic photon sorters for spectral and polarimetric imaging	79
7.1	Spectral imaging using SPs	81
7.1.1	Concept of plasmonic photon sorting	83
7.1.2	First tests on bi-eye and tri-eye structures : the need for groove depth gradient	83
7.1.3	Single and multiple bull's eye structures with groove depth gradient	86
7.2	Imaging polarimetry using SPs	92
7.2.1	The subwavelength slit as polarization analyzer	93
7.3	Combining slits in a honeycomb array	98
8	Conclusion and outlook	107
A	Acquisition of dispersion curves	109
B	Transmission through hole arrays with index-matching liquid	113
C	Labview program control panels and code schemes	117

Chapter 1

Introduction: “nano?”

In recent years, the word nano has spread from the world of science to society. It usually refers to properties and objects at length scales around the $1/1000000000$ part of one meter, a nanometer. The emergence of Nano-optics in the late 20th century would not have been possible without all the previous achievements in classical optics, going back all the way to antiquity.

The fundamental question how light shines through a hole interested Chinese thinkers already in the fifth century BC and there are documents [1] that show that image formation by pinholes [2] were already known to the philosopher Mozi [3] ($\sim 480 - \sim 390$ BC) (or Motsu [4]). In the western hemisphere, Aristotle (384 – 322 BC) also took an interest in the optical effects of a pinhole [5], but he could not find a satisfactory explanation for his observations.

In the 10th century, the studies of Ibn al-Haytham (965 – 1039) [7], also known by his western name Alhazen, spread the knowledge of optical elements such as pinholes [2] in the Arabic world (see Fig. 1.1a). His *Book of Optics* [8] summarized his findings and his scientific method which concentrated on observation, mathematical analysis and interpretation of experimental data. His writings inspired Europeans such as the Englishmen Robert Grosseteste (1175 – 1253) [9] and Roger Bacon (1214 – 1294) [10]. Although their works helped to promote the magnifying properties of curved glasses and also spread the knowledge of the camera obscura, the Middle Ages provided few breakthroughs in optics.

Things changed in the Renaissance era as the printing of books improved the communication of knowledge and also of optics. Precise drawings of camera obscura were then published as shown in Fig. 1.1b, taken from the book *De Radio Astro-*

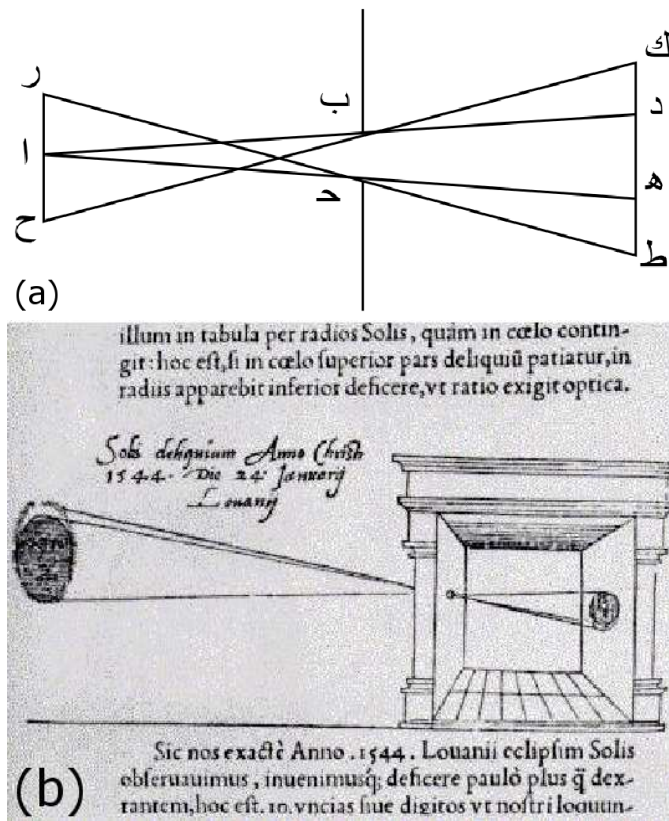


Figure 1.1: (a) Sketch of a pinhole by Alhazen from his *Book of Optics* (1011–1021)
 (b) Draw of a camera obscura in the book from Gemma Frisius [6] in 1544.



Figure 1.2: Drawing of an optical microscope by Hooke in his book *Micrographia* from 1665 [11].

nomica et Geometrica (1544) by the Dutchman G. Frisius [6]. As a consequence of the increased communication during this period and the spreading of scientific methodology, the understanding of optics evolved rapidly during the 16th and 17th century.

Phenomena like the laws of refraction were precisely documented by Snell (1580–1626) in the Netherlands and Descartes (1596 – 1650) in France, while at the same time in Italy, Galileo (1564 – 1642) helped promote optics by improving the telescope, who according to some was invented by Zacharias (1580 – 1638) [12–15]. Microscopes as the one shown in Fig. 1.2 also appeared in the beginning of the 17th century and became an important tool for scientists.

There are some hints [16] that Leonardo da Vinci (1452 – 1519) had observed what is nowadays known as diffraction already in the 15th century, but he never gave a thorough description. It is Grimaldi (1618 – 1663) who is generally credited with the discovery of diffraction and for introducing the term “diffraction”. More precisely, he noted that light, when transmitted through an aperture, casts a spot that is larger than expected from purely geometrical optics considerations as illustrated in Fig. 1.3. His works were only published after his death in 1665. Finding the correct explanation for his observations was hindered by the widely accepted corpuscular theory of light put forward by Newton (1643 – 1727). As a

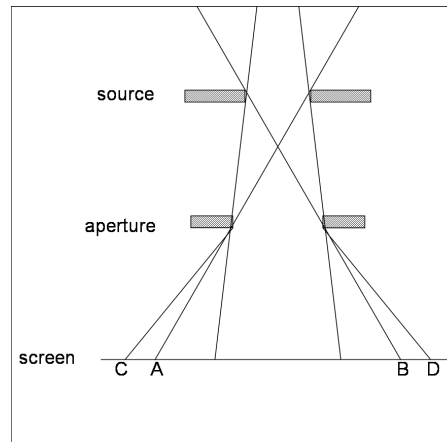


Figure 1.3: First observation of the phenomenon of diffraction by Grimaldi. The shadow that is cast by an aperture (CD) is larger than expected from a geometrical construction (AB).

consequence, the wavefront theory that had been previously introduced by Hooke (1635–1703) and Huygens (1629–1695) was overshadowed until the works of Young (1773 – 1829) and Fresnel (1788 – 1827). The famous double slit experiment by Young introduced the notion of interference of waves, and when Fresnel combined the wavefront model with the concept of interference to explain the phenomenon of diffraction, it was difficult to argue against light propagating as waves. The basic idea of the Huygens-Fresnel principle is that each point of a wavefront can be seen as a source of secondary spherical wavelets (Huygens) and that the intensity at any point can be determined by the interfering sum of all these point sources (Fresnel).

Kirchhoff (1824 - 1887) put this principle in a solid mathematical context and developed a scalar theory of diffraction, which is still considered valid for apertures large compared to the wavelength. Generally a distinction is made if the theory is applied to diffraction in the near-field (Fresnel type) or the far-field (Fraunhofer type) of an aperture.

The phenomenon of diffraction has important consequences for any image forming device such as a microscope. Lord Rayleigh (1842–1919) and Abbe (1840–1905) pointed out that for any imaging system there exists a minimum distance between two points that can be distinguished due to the diffraction. This defines a resolving power of the apparatus, known as the Abbe limit.

This resolution limit has for a long time hindered the visualization of objects

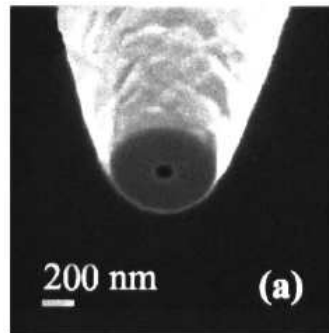


Figure 1.4: Tip of a metal coated optical fibre, with an aperture that has been fabricated by FIB milling [18].

small compared to the wavelength. The limit can be related to the Heisenberg uncertainty principle but there is no fundamental physical law that prohibits setups with smaller resolutions [17]. Nevertheless overcoming this limit poses major challenges.

The first documentation of a setup to overcome this diffraction limit was presented by Synge in 1928 [19]. His proposition was extremely simple: a small sub-wavelength diffractive object such as a particle (or an aperture) is placed very near a sample surface, and a microscopic setup with a photoelectric cell is aligned in such a way that the only light that is collected comes from the diffraction at the particle. By scanning the particle or the aperture over the sample it is possible to record an image which is not limited by diffraction. Nevertheless it was only after discussions with Einstein that he was convinced to publish his ideas, as he was aware of the great experimental challenges that needed to be overcome in order to realize such a setup. One of the main difficulties in subwavelength optics is the small amount of light available for detection. This is the reason why for many years Synge's ideas were nearly forgotten.

While in acoustics a resolution not limited by diffraction was achieved in 1956 [20], the first near-field measurement of electromagnetic waves was reported in 1972 [21]. However this was in the GHz range and it was not until 1984 that the first scanning near-field optical measurements (SNOM) were achieved by Pohl and co-workers [22]. In their experiment they put an aperture close enough to the surface to be sensitive to the evanescent field and by scanning it over the sample it was possible to map the surface with a resolution defined by the size of the aperture



Figure 1.5: The Lycurgus Cup with different illuminations showing plasmonic resonances.

and not by the wavelength. Significant improvements in SNOM technology were achieved in the early 90s with the use of apertures fabricated in metal coated optical fibers [23] and shear-force techniques to control the movement of the fiber. [24,25].

Since surface plasmons (SPs) are evanescent waves at a metal-dielectric interface, their study has greatly benefitted from techniques such as SNOM [15,26,27]. SPs are electron density oscillations and can be understood in a simple way as electromagnetic waves trapped at such metal-dielectric interfaces. They can exist both as local oscillations (e.g. on metallic nanoparticles) or as delocalized propagating waves.

When illuminating metallic nanoparticles, the scattering of light generates localized surface plasmons, which can result in specific colorful shades. Although people were not aware of the microscopic reasons for this effect, nanoparticles were for a long time embedded in glass in order to give it a specific color. One of the most famous examples is the Lycurgus cup shown in Fig. 1.5, which dates from the 4th century AD and is composed of a glass that contains silver and gold nanoparticles. This cup appears green if illuminated from the outside (i.e. in reflection) and gives a variety of colors when the light source is placed inside.

The precise explanations of such observations were only made possible centuries later with the development of rigorous electromagnetic theory. Using Maxwell's equations, Mie [28] was able to realize a rigorous description of light scattering at small particles in 1908 explaining the origin of the visible colorful shades. Nearly at the same time Debye found an equivalent solution, while trying to understand

the effects of light pressure on metallic spheres [29].

At the same period, Sommerfeld [30] and Zenneck [31] described the propagation of electromagnetic waves on surfaces in the context of telecommunications which bear close resemblance to today's propagating plasmonic waves.

Half a century later, Ritchie [32] calculated that the diffraction of an electronic beam inside a metal can not only excite bulk plasmons, but also surface waves. Experimental confirmation of this prediction soon followed and the word surface plasmon was coined. In 1968, the independent works of Otto [33] and Kretschmann and Raether [34] showed how the phenomenon of total internal reflection on a prism can be used to launch surface plasmons by optical coupling. These techniques facilitated the fundamental studies of surface plasmons and their use. In particular, the adsorption of molecules on a metal surface modifies the light to surface plasmon coupling conditions and this knowledge was used to develop a new class of sensors called SPR (for surface plasmon resonance) [35]. In the 70's the observation that Raman scattering can be strongly enhanced if the molecules are adsorbed on rough metallic surfaces [36, 37] led to the development of the field of SERS (Surface Enhanced Raman Spectroscopy). The field has since evolved to the extent that it is now possible to observe the Raman signal of single molecules [38, 39].

Although SP were useful for such sensing applications, in the field of optics and photonics they were rather seen as a nuisance and a source of damping and losses. This perception changed in the 90's as fabrication and characterization techniques evolved and it became possible to precisely control the properties of SPs by shaping metallic surfaces at the nanoscale as illustrated by the examples in Fig. 1.6 and Fig. 1.7. This has led to a wide interest in plasmonics in recent years in fields as diverse as quantum optics, waveguiding, imaging, medicine, spectroscopy or data storage [40–46].

The present thesis concentrates on different aspects of plasmonics. The next two chapters are dedicated to introducing the key notions in regards to surface plasmons, hole arrays and individual apertures. Chapter 4 explains the experimental procedures of the measurements reported in the following chapters. In Chapter 5 we concentrate on some fundamental aspects of the light transmission through subwavelength hole arrays. In particular, the enhanced transmission is studied as a function of hole size and depth. Of specific interest is the cutoff transition, which occurs when the hole size is large enough to sustain propagating modes. Chapter

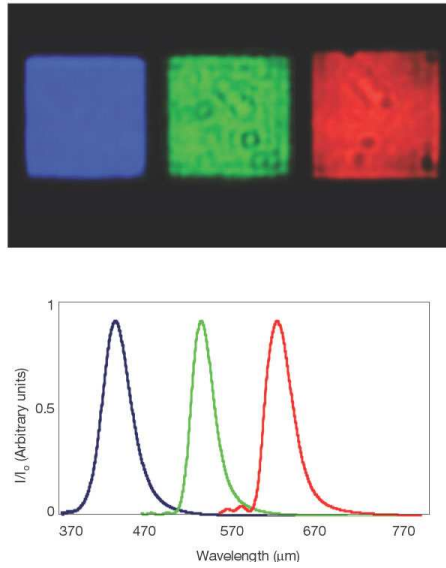


Figure 1.6: Normal incidence transmission images (top) and spectra (bottom) for three square arrays of subwavelength holes. The figure shows that nanostructures can control the resonant wavelength of SP phenomena. Figure from [40].

6 addresses one of the most fundamental questions in optics, diffraction, in the context of subwavelength apertures. For this purpose, a new experimental system had to be built and it is explained in detail together with some preliminary results. The last chapter is dedicated to developing plasmonic structures for spectral and polarimetric imaging purposes. By overlapping different plasmonic structures, it is possible to create a very small device that enables the simultaneous spectral and polarimetric filtering of light.

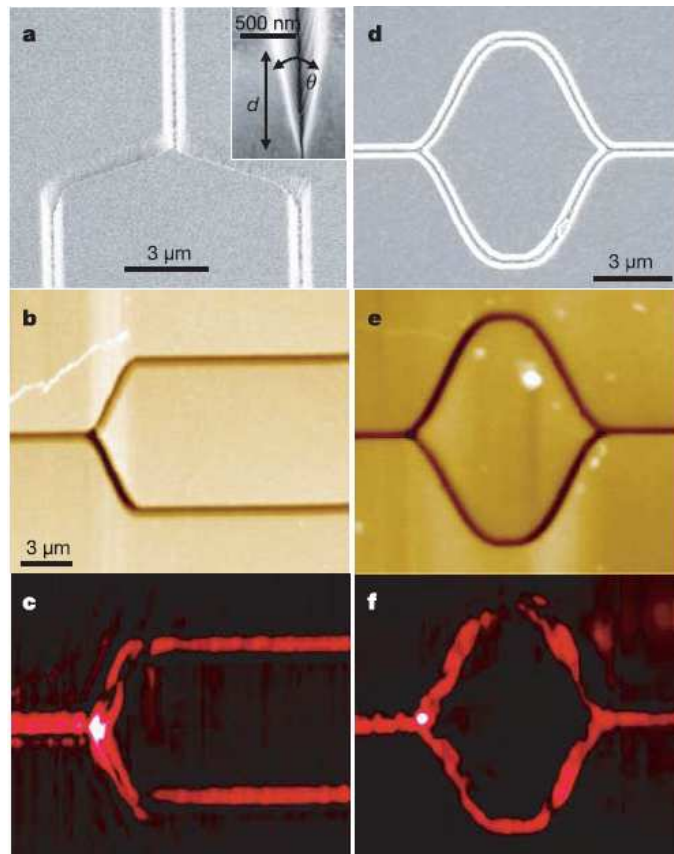


Figure 1.7: Plasmonic Y-splitter and MachZehnder (MZ) interferometer realized using a V groove profile enabling large propagation lengths. Figure from [44].

Chapter 2

Surface plasmons

2.1 Definition of surface plasmons

The structure of any crystalline metal can be explained in terms of a gas of free electrons embedded in an array of positively charged ions (the crystal). These free electrons do not only lead to well-known electronic characteristics like conductivity, but they can also exhibit other interesting electromagnetic properties. Of particular interest is their ability to sustain collective density oscillations which are quantified and known as plasmons [47].

The symmetry breaking at a metal interface can lead to specific oscillation modes that are bound to the surface known as surface plasmons (SP). In this chapter we will discuss the conditions necessary for their existence together with their properties that are relevant for this thesis.

2.2 Condition of existence of surface plasmons

Let us consider the interface shown in Fig. 2.1 between a metal characterized by a complex dielectric constant $\varepsilon_m = \varepsilon_{m1} + i\varepsilon_{m2}$ and a dielectric medium with only a real ε_d . Both media are supposed to be isotropic and homogenous, the interface being the only discontinuity. We also define a cartesian coordinate system such that the $z = 0$ plane coincides with the interface. The half space defined by $z < 0$ corresponds to the metallic layer, whereas the half space $z > 0$ corresponds to the dielectric layer. In the following we will describe the properties for an plasmonic surface wave

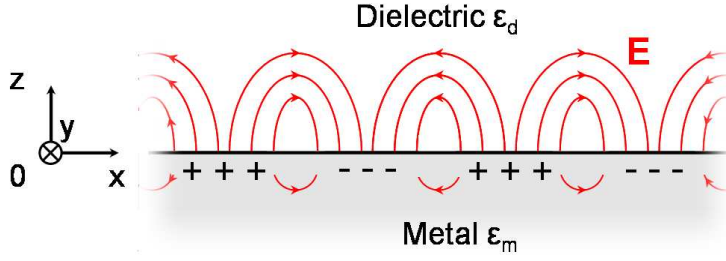


Figure 2.1: Surface plasmon polariton propagation on a metal dielectric surface.

characterized by electron density oscillations at the interface and exponentially evanescent electromagnetic fields as illustrated in Fig. 2.1.

By applying the boundary conditions defined by the interface to Maxwell's equation it can be shown that surface wave solutions exist only for specific cases [15, 26, 27]. For instance no bound surface wave exists with a TE polarization. For TM polarization, the system of equations can be solved and corresponding electromagnetic fields (\mathbf{E} , \mathbf{H}) are given by:

- for $z < 0$ (metal)

$$\mathbf{E}(x, y, z, t) = E_0 \begin{pmatrix} 1 \\ 0 \\ \frac{k_{SP}}{k_{zm}} \end{pmatrix} e^{-ik_{zm}z} e^{i(k_{SP}x - \omega t)}$$

$$\mathbf{H}(x, y, z, t) = E_0 \begin{pmatrix} 0 \\ -\frac{\varepsilon_0 \varepsilon_m \omega}{k_{zm}} \\ 0 \end{pmatrix} e^{-ik_{zm}z} e^{i(k_{SP}x - \omega t)}$$
(2.1)

- for $z > 0$ (dielectric)

$$\begin{aligned} \mathbf{E}(x, y, z, t) &= E_0 \begin{pmatrix} 1 \\ 0 \\ \frac{k_{SP}}{k_{zd}} \end{pmatrix} e^{-ik_{zd}z} e^{i(k_{SP}x - \omega t)} \\ \mathbf{H}(x, y, z, t) &= E_0 \begin{pmatrix} 0 \\ -\frac{\varepsilon_0 \varepsilon_d \omega}{k_{zd}} \\ 0 \end{pmatrix} e^{-ik_{zd}z} e^{i(k_{SP}x - \omega t)} \end{aligned} \quad (2.2)$$

In these equations, k_{SP} is the component of the wavevector that is parallel to the surface and a conserved quantity across the interface, whereas k_{zd} and k_{zm} are the different components normal to the interface into the dielectric and the metallic layer respectively. These wavevectors are not independent and linked by the relations:

- for $z < 0$ (metal)

$$\varepsilon_m \left(\frac{\omega}{c} \right)^2 = k_{SP}^2 + k_{zm}^2 \quad (2.3)$$

- for $z > 0$ (dielectric)

$$\varepsilon_d \left(\frac{\omega}{c} \right)^2 = k_{SP}^2 + k_{zd}^2 \quad (2.4)$$

If these relations are combined with the boundary conditions that are defined by the interface, it is possible to determine the in-plane wavevector of the SPs, giving the dispersion relation of the surface plasmon [15, 26, 27]:

$$k_{SP}^2 = \left(\frac{\omega}{c} \right)^2 \frac{\varepsilon_m \varepsilon_d}{\varepsilon_m + \varepsilon_d} \quad (2.5)$$

The other wavevector components normal to the interface k_{zm} and k_{zd} can also be expressed as a function of the dielectric constants of the system by combining Eq.(2.3), (2.4) and (2.5).

- for $z > 0$ (dielectric)

$$k_{zd}^2 = \left(\frac{\omega}{c} \right)^2 \frac{\varepsilon_d^2}{\varepsilon_d + \varepsilon_m} \quad (2.6)$$

- for $z < 0$ (metal)

$$k_{zm}^2 = \left(\frac{\omega}{c}\right)^2 \frac{\varepsilon_m^2}{\varepsilon_d + \varepsilon_m} \quad (2.7)$$

A surface wave is characterized by a real in-plane wavevector to enable propagation along the surface as well as a normal wavevector component that is purely imaginary to ensure that the wave is bound to the surface. This particular solution imposes certain restrictions on the dielectric constants at the interface. To simplify this discussion, we can assume that the imaginary part of the complex dielectric function of the metal is small compared to the absolute value of the real one ($|\varepsilon_{m1}| \gg \varepsilon_{m2}$). In this case a real k_{sp} can only be obtained if the sum and the product of the dielectric constants are either both positive or both negative (Eq.(2.7)). We can further conclude from Eq.(2.8) and (2.9) that the sum $\varepsilon_1 + \varepsilon_m$ needs to be negative to ensure imaginary k_{zm} and k_{zd} . Thus the conditions that need to be fulfilled by the interface in order to sustain a surface plasmon oscillation can then be expressed as:

$$\begin{cases} \varepsilon_{m1} \cdot \varepsilon_d < 0 \\ \varepsilon_{m1} + \varepsilon_d < 0 \end{cases} \quad (2.8)$$

In general this is verified for an interface between a metal and a dielectric since metals have a negative ε_{m1} . For studies in the visible, the most commonly used metals are noble ones such as Au or Ag, and the dielectric layer usually consists of air or glass.

2.3 The dispersion relation of surface plasmons in a real metal

The SP dispersion relation given by Eq.(2.7) is well illustrated by the case of Ag. It can be calculated using tabulated values for the dielectric constants [48] and plotted together with the corresponding dispersion curve of freely propagating light as shown in Fig. 5.3 at both air and glass interfaces.

The curves of both interfaces follow the same evolution, which illustrates the fact

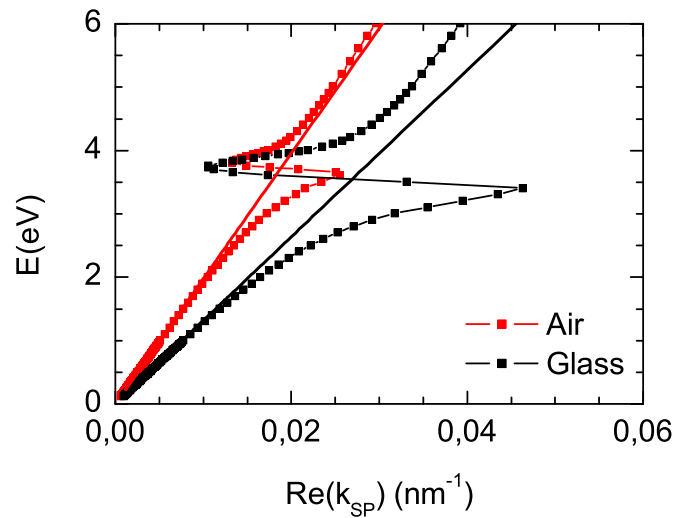


Figure 2.2: Dispersion relation for surface plasmons at an Ag-air interface (black curve) and an Ag-glass interface (red curve). The curves have been plotted using tabulated data for the dielectric constants given by Palik [48].

that the dispersion is mainly determined by the dielectric properties of the metal, whereas the dielectric material mainly modifies the overall slope of the curve.

Below 3.5 eV, the SP solution corresponds to an evanescent wave having a larger momentum than the freely propagating light. In the range of very small energies, the SP dispersion is not very different from the one of freely propagating light. As a consequence the SP is similar to a grazing wave and only weakly bound to the interface. In this case the electromagnetic field of the SP is to a large extent localized inside the dielectric medium. For larger energies (i.e. shorter wavelengths), the momentum of the SP increases as the coupling between the electromagnetic field and the density charge oscillation becomes stronger. As a result the wave is more strongly bound to the surface. This dual nature of the oscillation is the reason why in this frequency range SPs are often denoted as polaritons (surface plasmon polariton or SPP).

Around 3.5 eV, an interband transition occurs between electronic states inside the metal inducing a drastic change in the dielectric constants and consequently in the dispersion. It marks the transition into the non-evanescent sector, where the wave is no longer bound to the surface.

2.4 Energy confinement and propagation length of the SPs

The electromagnetic field associated with the SP follows an exponential decrease normal to the interface as given by Eq.(2.6) and (2.7). The extensions δ_m and δ_d into the metal and the dielectric can be determined respectively from k_{zm} and k_{zd} [26]:

$$\delta_m = \frac{1}{|k_{zm}|} \quad (2.9)$$

$$\delta_d = \frac{1}{|k_{zd}|} \quad (2.10)$$

δ_m is known as the skin depth and for a noble metal such as Ag is on the order of tens of nanometers for wavelengths in the visible (see Fig. 2.3). Inside the dielectric layer the SP field extends much further, typically a couple of hundred nanometers. This implies that the energy of the electromagnetic field associated with the SP is confined to a subwavelength thickness at the interface. This property together with the sensitivity on the refractive index of the interface makes the SPs very sensitive to surface features such as adsorbates, hence the use of surface plasmon for sensing molecules [35].

When discussing the conditions necessary to sustain SPs, we neglected the imaginary part ε_{m2} of the dielectric constant of the metal. This imaginary part ε_{m2} describes the absorption in the metal which affects the life time and the propagation length of the SP. As a result the intensity of the SP is expected to decay exponentially as a function of the displacement x . By determining the imaginary part of k_{sp} using Eq.(2.7), it is possible to define a propagation length for the SP as follows:

$$L_{sp} = \frac{1}{2\text{Im}(k_{sp})} \quad (2.11)$$

In Fig. 2.4, this propagation length is shown as a function of wavelength for a SP wave propagating along a plane Ag film. It can be seen that the propagation length is an increasing function of wavelength mainly due to the decreasing absorption by the metal. While for instance at 600nm, the propagation length is around $5\mu\text{m}$ for an Ag-glass interface and close to $20\mu\text{m}$ for an Ag-air interface, it can reach

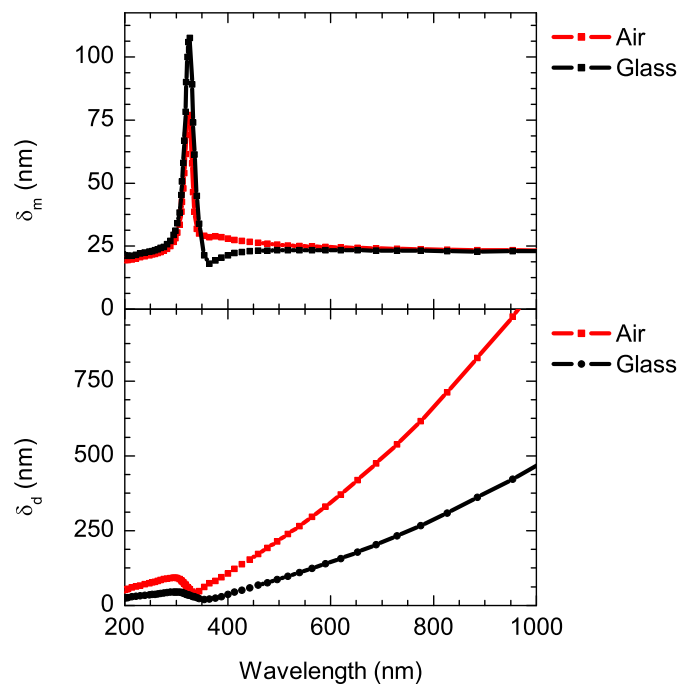


Figure 2.3: Extension of the electromagnetic fields for a SPs at an Ag-air interface (black curve) and an Ag-glass interface (red curve). The curves have been plotted using tabulated data for the dielectric constants given by Palik [48].

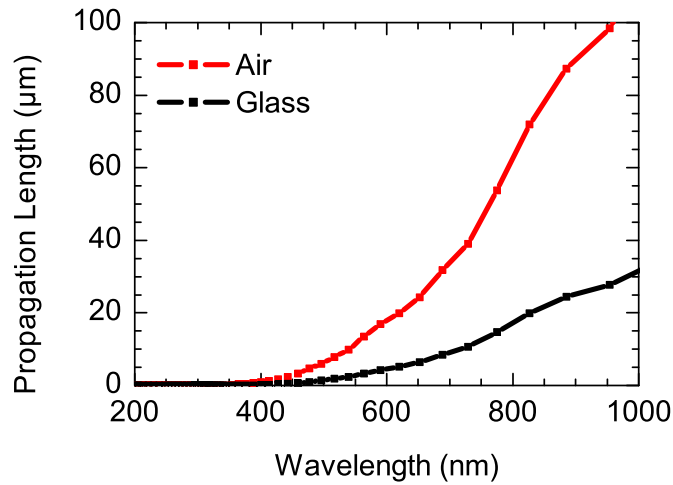


Figure 2.4: Propagation Length of SPPs at an Ag-air interface (black curve) and an Ag-glass interface (red curve). The curves have been plotted using tabulated data for the dielectric constants given by Palik [48].

the millimeter scale in the IR. This has stimulated much research into surface plasmon circuitry [42].

2.5 How to excite SPs

As it was noted while discussing the dispersion of SPs, their momentum is larger than that of freely propagating light at the same wavelength. This is why SPs can not be excited just by illuminating a metal-dielectric interface with a plane wave. Coupling between photons and SPs requires therefore specific conditions in order to ensure momentum conservation. Although there are several approaches to achieve momentum matching involving for example near-field tips [49] or fluorescent molecules [50], the most common techniques are based on ATR (attenuated total reflection) or grating coupling as presented below.

2.5.1 Coupling using Attenuated Total Reflection

Historically, the first techniques that were developed to optically excite SPs, were proposed by Otto [33], Raether and Kretschmann [34, 51] around 1970. In both approaches a metal surface is illuminated through a prism consisting of a dielectric

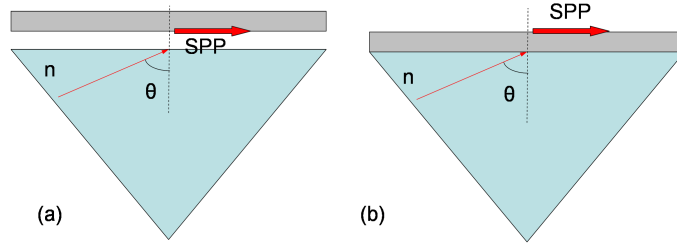


Figure 2.5: Excitation of SPPs using attenuated total internal reflection in the Otto (a) and in the Kretschmann-Raether (b) configuration.

of higher index n such as glass which increases the momentum of light \mathbf{k}_0 . The phenomenon of total internal reflection at the top surface gives rise to evanescent fields. In the Otto configuration [33] shown in Fig. 2.5a, a metal film is brought close enough to the this surface to be sensitive to the evanescent field. In this case coupling between the evanescent field and SPs (wavevector \mathbf{k}_{SP}) on the metal surface becomes possible and the corresponding condition can be found by projecting the different wavevectors on surface plane according to Eq.(2.12):

$$k_{sp} = nk_0 \sin\theta \quad (2.12)$$

The approach presented by Kretschmann and Raether [34, 51] is based on the same principles, but the metal film is directly deposited on the metal film as shown in Fig. 2.5b. In this case the evanescent coupling through the metal film is however only possible for very thin films.

Such evanescent coupling through a higher index prism can also be reversed and used for imaging purposes. If a surface plasmon propagates along a metal interface, radiation can leak into a higher index substrate if the metal film is thin enough to enable evanescent coupling as illustrated in Fig. 2.6a. This leakage radiation can be measured for example with an photographic plate (see Fig. 2.6b) as originally proposed by Simon and Guha [53] in 1976. Leakage radiation microscopy has since become an interesting tool to measure the propagation of SPs and can be used to reveal information that would only be accessible through complicated near-field measurements [52].

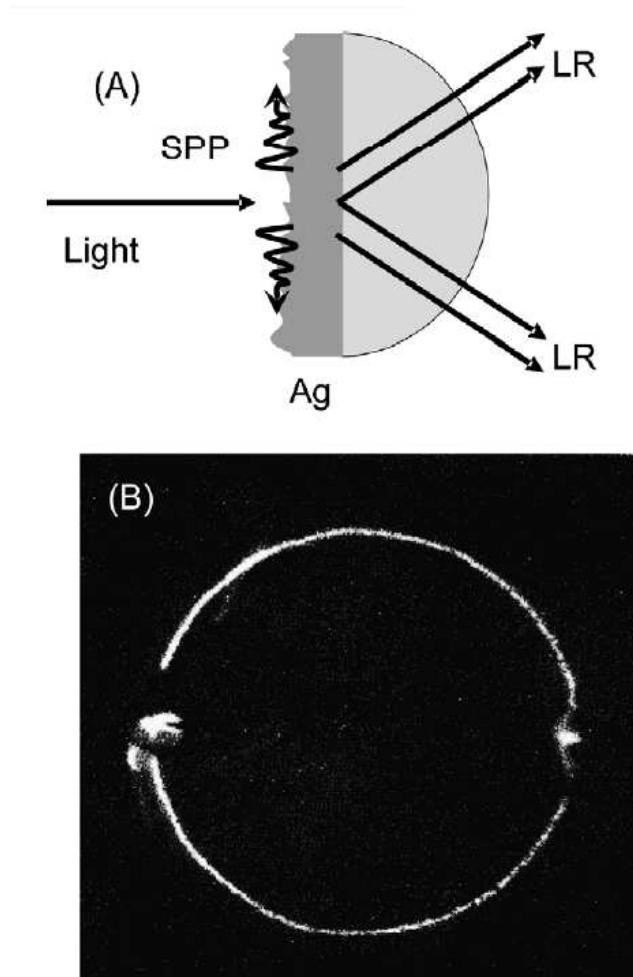


Figure 2.6: Observation of leakage radiation through a rough thin silver film, (A) SPPs are launched from surface roughness at the Ag-air interface and its radiation leaks through the glass substrate. Image from [52]. (B) Photography of the leakage radiation detected using a photographic plate. From the original work of Simon and Guha [53].

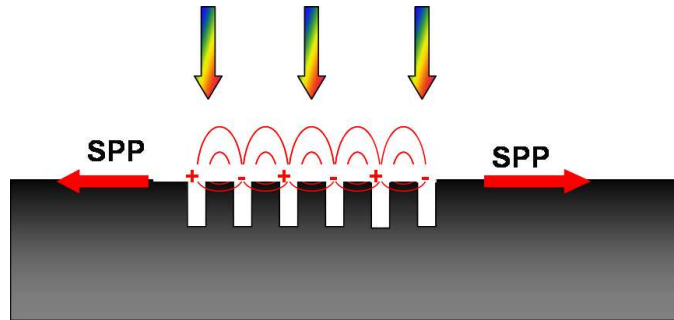


Figure 2.7: Excitation of SPPs using a periodic structure on a metal-dielectric interface.

2.5.2 Grating coupling

Another way to achieve optical SP excitation is to diffract the incoming light on a surface grating. In this case, the difference in momentum between the illuminating light \mathbf{k}_0 and \mathbf{k}_{sp} is matched through the reciprocal wavevector \mathbf{G} of the grating. Consequently the characteristics of the grating determine to a large extent the wavelengths of the SP that can be excited. The coupling condition for a simple $1D$ as the one shown in Fig. 2.7 can be expressed as follows:

$$\mathbf{k}_{sp} = \mathbf{k}_0 \pm \mathbf{G} \quad (2.13)$$

In the case where the grating consists of an array of subwavelength holes, the transmission through such holes can be strongly enhanced due to surface plasmon resonances at the surface [41]. This phenomenon known as the extraordinary optical transmission will be at the center of more detailed discussions in the following chapters.

2.6 Localized surface plasmons

It should be noted that surface plasmons do not only exist as delocalized propagating waves. When placing small metallic particles in an electromagnetic field, they can also sustain density charge oscillations as shown in Fig. 2.8 [54]. These oscillations called localized surface plasmons (LSP), can not propagate as the electron movements are limited to the nanoparticle. The characteristic scattering signature

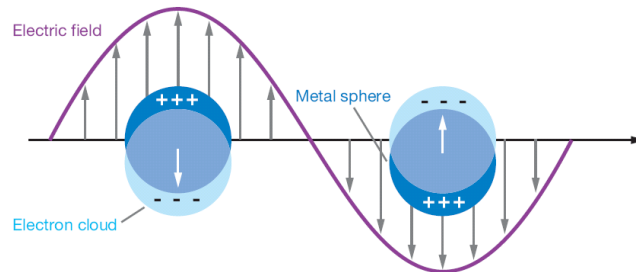


Figure 2.8: Localized Surface Plasmon at a metal nanoparticle. From [54].

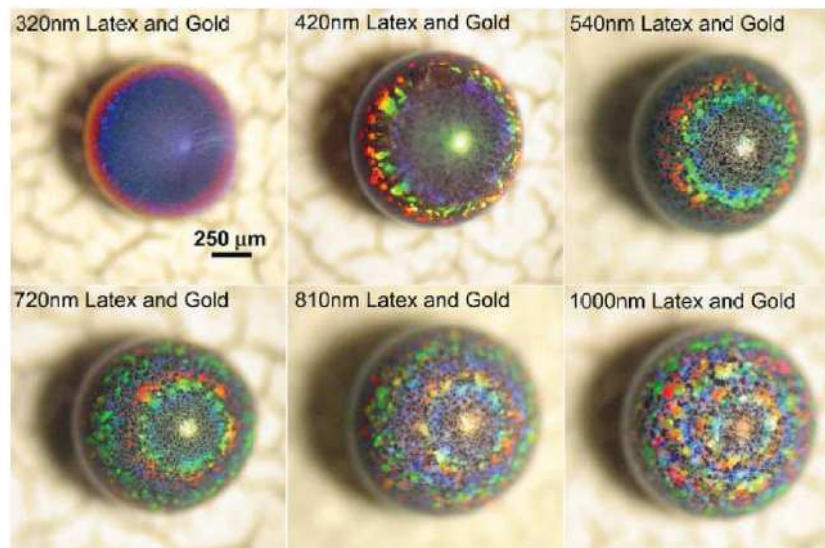


Figure 2.9: Optical microscopy images of latex and gold nanoparticle opal balls containing microspheres of varying sizes [55].

of these modes depends strongly on the size and shape of the nanoparticles and can result in beautiful colorful patterns in the diffracted far-field as illustrated in Fig. 2.9.

It is worth noting that such localized modes can also be excited for other types of individual scattering elements. For instance studies on the transmission through isolated apertures [56] and through apertures in periodic arrays [57–59] have provided several observations of localized resonances depending the shape and size of the individual holes.

Chapter 3

The transmission of light through small holes

As discussed in the introductory chapter, understanding the process of light transmission through small openings is of fundamental importance for optics and in particular for nano-optics. In this chapter we will therefore review the classical models describing this process for circular apertures either smaller or larger than the wavelength. Of particular interest in the context of this thesis are periodic arrangements of subwavelength holes as their transmission spectra feature very high transmission peaks related to the extraordinary optical transmission (EOT) [41]. We will discuss the role of surface plasmons in this process and review how some of the different structural parameters of such a hole array influence the transmission [40, 43, 45].

3.1 Classical theories on the transmission of light through single apertures: The Fraunhofer-Fresnel diffraction and the Bethe model

A theoretical description of diffraction was first achieved for circular apertures having a radius a much larger than the wavelength ($\lambda \ll a$) in an infinitely thin screen. In this context a good approximation of the experimentally visible emission pattern is given by the Fresnel-Kirchhoff diffraction integral [13, 14]. In addition to the Huygens-Fresnel principle, the key hypothesis of this approach is that the presence of the infinitely thin screen does not influence the electromagnetic field distribu-

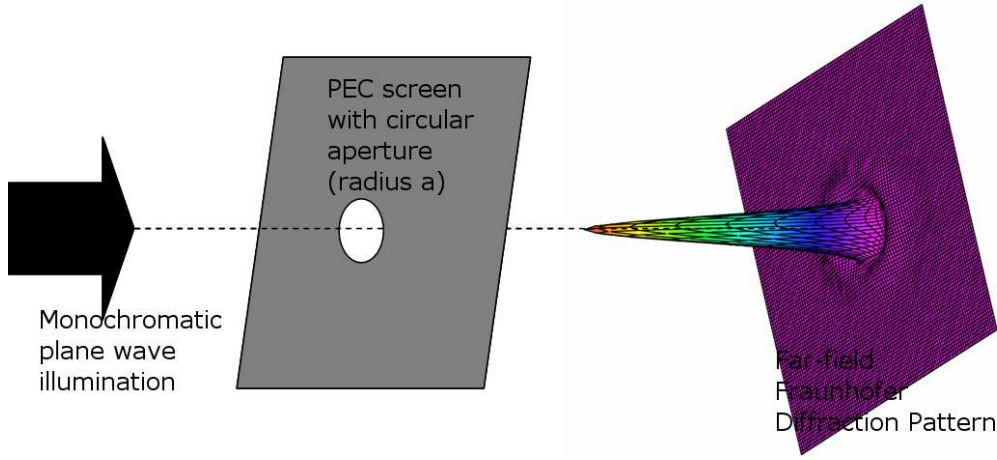


Figure 3.1: Fraunhofer far-field diffraction for a circular aperture in an opaque screen.

tion inside the aperture. The light intensity at a point $P(x, y)$ on the observation plane placed at a distance d from the diffracting aperture is then given by Eq.(3.1) provided that the Fresnel number N_F ($N_F = (x^2 + y^2) / \lambda d$) is sufficiently small ($N_F \ll 1$) [60].

$$I(x, y) = I(0) \left[\frac{2J_1 \left(\frac{2\pi a \sqrt{x^2 + y^2}}{\lambda d} \right)}{\frac{2\pi a \sqrt{x^2 + y^2}}{\lambda d}} \right]^2 \quad (3.1)$$

This diffracted light pattern is related to the Fourier transform of the illuminated aperture [13, 14, 60] and consists of a central bright spot, the Airy disc with several concentric rings, as illustrated on Fig. 3.1. The central disc contains already 84% of the total amount of transmitted light, and this intensity reaches up to 91% if the first ring is included.

In nano-optics where the apertures are typically smaller than the wavelength, a different model is necessary. In particular apertures smaller than half the wavelength ($a < \lambda/2$) do not allow the existence of a propagating electromagnetic field inside the opening [13, 61]. In the context of holes much smaller than the wavelength, a solution of Maxwell's equations was calculated by Bethe in 1944 [62]. He found that a subwavelength hole of radius a in an infinitely thin perfect electric conductor (PEC) screen can be described as a combination of a magnetic and electric

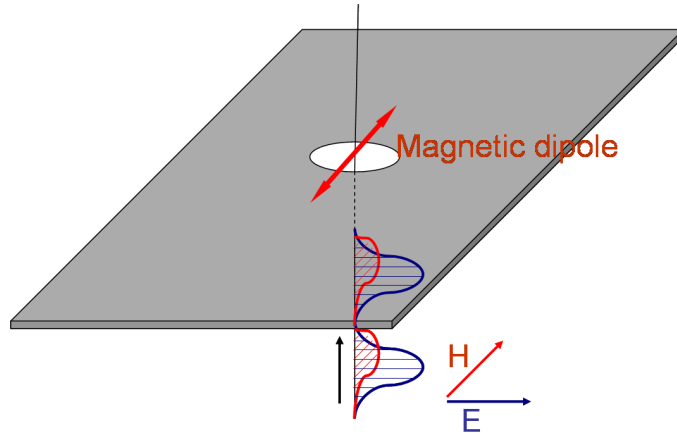


Figure 3.2: Dipole induced by illuminating a subwavelength hole by an electromagnetic field at normal incidence.

dipoles. Upon normal illumination, the electric dipole can not be excited, reducing the hole in this model to a purely magnetic dipole. This magnetic dipole lies in the plane of the aperture and its direction is determined by the polarization of the incident electromagnetic field as illustrated in Fig. 3.2.

The intensity of the transmitted electromagnetic field through the aperture consequently depends on the strength of this induced dipolar moment and is a function of the radius of the aperture a and the illumination wavevector k_0 :

$$T = \frac{64}{27\pi^2} (k_0 a)^4 \quad (3.2)$$

Given the dependance on $k_0 a$, it is to be expected that this transmission is very weak for holes much smaller than the wavelength ($k_0 a \ll 1$). It should also be noted that this model was later refined by Bouwkamp. [63,64]. He introduced higher order correction terms for the transmittance of such a subwavelength hole in $(k_0 a)^P$ with $p > 6$.

A specific diffraction pattern is also associated with a radiating magnetic dipole. In the normal plane perpendicular to the magnetic dipole, this radiation should be isotropic, whereas parallel to the dipole, it should follow a $\cos^2\theta$ dependance (θ being the angular deviation from the normal to the surface) [62].

However, a real metal has a more complicated optical response than that expected in the PEC approximation [56, 65–69]. Indeed a few experimental studies

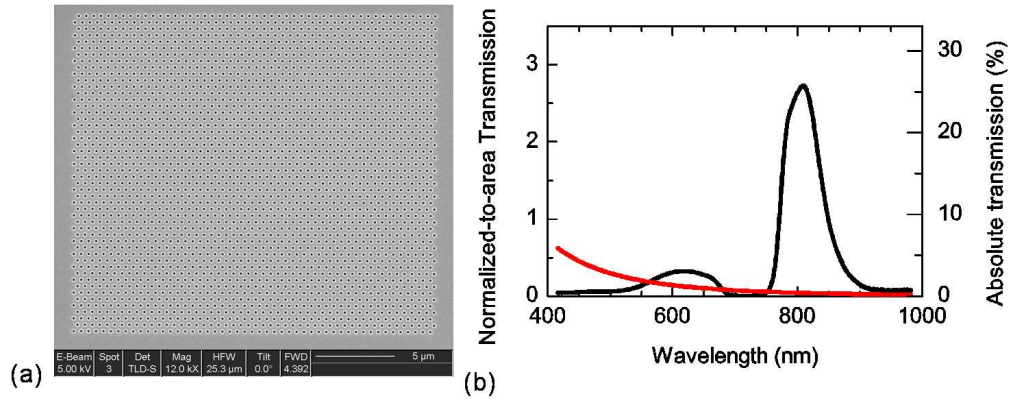


Figure 3.3: (a) Scanning electron microscope image of an array of subwavelength holes in a periodic hexagonal lattice. The hole arrays was fabricated by FIB milling in a 170nm thick Au film. The period of the lattice is 520nm and the hole diameter is 170nm. (b) Transmission spectrum of the same hole array when covered with an index-matching liquid (black line). The red line shows the expected transmission from Bethe's formula (Eq.(3.4)).

indicate that the diffraction of subwavelength holes in metal films deviate from the above predictions [56, 70–72]. This has motivated our study of the diffraction of subwavelength circular holes in Chapter 6.

3.2 Coupling light to surface plasmons with hole arrays

The Bethe model was widely accepted in the scientific community until the 90's when technology evolved and considerably improved the fabrication of nanoscale apertures. Of specific interest was the observation that the transmission through subwavelength holes can be largely increased if they are placed in a periodic array [41] (see Fig. 3.3). Upon normal illumination, such transmission spectra feature peaks at specific wavelengths depending on the periodicity of the structure. The transmission at these peaks is strongly enhanced compared to what is expected from the Bethe model and can even surpass unity if normalized to the area occupied by the the holes (see Fig. 3.3), justifying the name extraordinary optical transmission (EOT).

The peaks in the transmission spectrum can be related to the excitation of

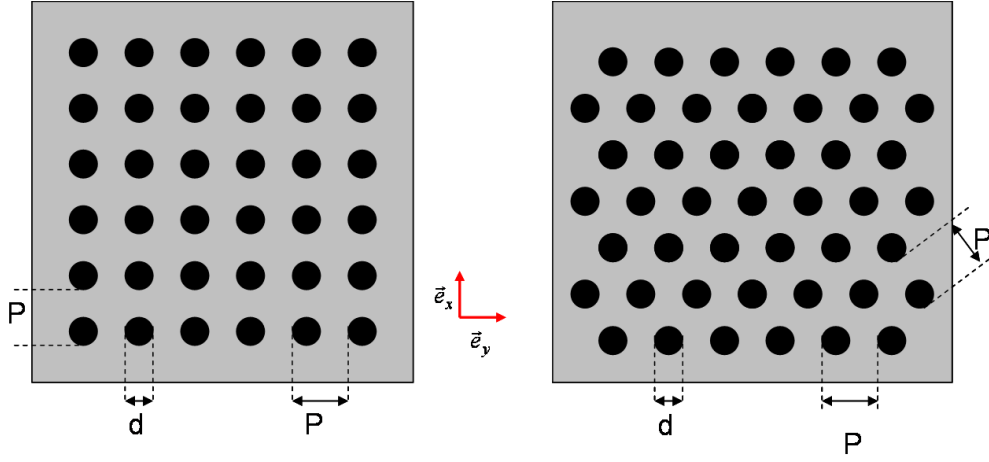


Figure 3.4: Hole arrays in two different configurations: square array and hexagonal array.

surface plasmons (SP) at the metal interface. As already stated in Chapter 2, at a given frequency SPs have a larger wavevector (\mathbf{k}_{sp}) than freely propagating light (\mathbf{k}_0). The grating momentum provided by the periodic arrangement of holes can overcome this momentum mismatch. Thus the light to SP coupling condition can be written as follows:

$$\mathbf{k}_{sp} = \mathbf{k}_0 + \mathbf{G}(i, j) \quad (3.3)$$

where $\mathbf{G}(i, j)$ is the reciprocal wavevector (or grating momentum) of the array and i and j denote the different scattering orders.

Hole arrays can be realized in different symmetries, for instance in a square or a hexagonal array as illustrated in Fig. 3.4. For these symmetries, the different reciprocal wavevectors $\mathbf{G}(i, j)$ are related to periodicity P of the array as follows:

for the square array,

$$\mathbf{G}(i, j) = i \frac{2\pi}{P} \vec{e}_x + j \frac{2\pi}{P} \vec{e}_y \quad (3.4)$$

for the hexagonal array,

$$\mathbf{G}(i, j) = \left(i - \frac{1}{2}j \right) \frac{2\pi}{P} \vec{e}_x + \frac{\sqrt{3}}{2} j \frac{2\pi}{P} \vec{e}_y \quad (3.5)$$

By combining this reciprocal wavevector with Eq.(3.3) at normal incidence, it

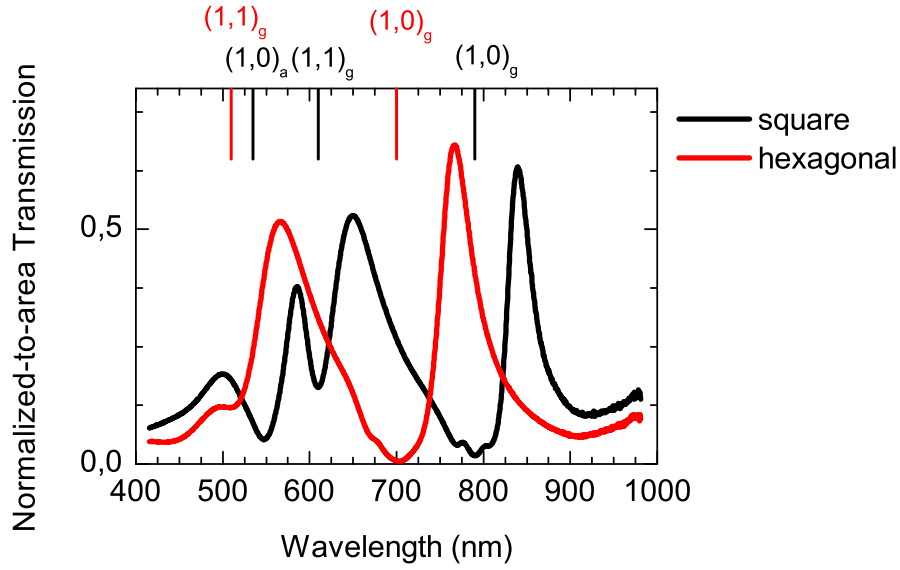


Figure 3.5: Transmission spectra for two hole arrays milled in an optically thick Au film (200nm) of period 500nm and of hole diameter 190nm. The black curve corresponds to a square array of holes and the red one a hexagonal one. The vertical lines give the theoretical peak position as given by Eq.(3.6) and (3.7).

is possible to determine the resonance wavelengths for any given mode and array symmetry:

for the square array,

$$\lambda(i, j) = \frac{P}{\sqrt{i^2 + j^2}} \sqrt{\frac{\epsilon_m \epsilon_d}{\epsilon_m + \epsilon_d}} \quad (3.6)$$

and for the hexagonal array,

$$\lambda(i, j) = \frac{P \frac{\sqrt{3}}{2}}{\sqrt{i^2 + j^2 - ij}} \sqrt{\frac{\epsilon_m \epsilon_d}{\epsilon_m + \epsilon_d}} \quad (3.7)$$

First it should be noted that both relations define a certain number of resonances as a result of the different scattering orders denoted by (i, j) . In Fig. 3.5, these theoretical resonance positions can be visualized together with transmission spectra of two different hole arrays having the same geometrical parameters (film thickness h , period P , hole diameter d) but different symmetry.

In all cases, the predicted theoretical resonances are near the minima located at slightly shorter wavelengths than the experimental peaks. This displacement

has been studied both theoretically and experimentally and it has been explained as a result from an interference effect between a resonant contribution (SP) and a non-resonant one (light scattered at the hole) [73–77].

By comparing both spectra in Fig. 3.5, it can be observed that for the hexagonal array the peaks are shifted to the shorter wavelengths than for the square one, as expected from Eq.(3.6) and (3.7).

It should also be noted that for each spectrum there are two series of peaks corresponding to the two interfaces of the metal: metal-glass and metal-air. The difference in the ε_d at the two interfaces translates to a shift in the peak positions according to Eq.(3.6) and (3.7). As the difference in the refractive index of the dielectric material on either side decreases, it is possible to induce coupling between the SP modes on both sides of the metal film which can result in much higher transmission intensities [78]. For instance when the hole array is covered with an index-matching liquid (Fig. 3.3), there is only one series of peaks, but their intensities are typically much higher.

It should also be noted that the different modes denoted by the indices (i, j) are degenerated at normal incidence. For instance in the case of a square array with 4-fold symmetry, there are four degenerate modes giving the same resonance wavelength: $(1, 0)$, $(0, 1)$, $(-1, 0)$ and $(0, -1)$. The difference between the modes lies in their propagation direction. By illuminating the array with polarized light it is possible to specifically control which SP modes are excited [79]. These has been used to launch or disperse SP waves in well-defined directions [80–82] offering possibilities for SP-based integrated circuits [42].

Another way to lift the degeneracy is to illuminate the array at an angle [79, 83]. This shifts the different modes with respect to each other, splitting the transmission peaks. By measuring the transmission spectra as a function of angle, it is possible to acquire the dispersion of the SPs on the array as illustrated in Fig. 3.6. The bending of the theoretical resonance curves that can be observed for energies around 2.6eV can be related to interband transitions in the Au film. As discussed in the previous chapter the SP propagation length is strongly reduced near such a transition and consequently the enhanced transmissions is suppressed. The highest transmissions are found when modes on each side of the metal film are excited simultaneously as already observed by Krishnan *et al.* [78].

Although the excitation of SPs on hole arrays is generally characterized by its

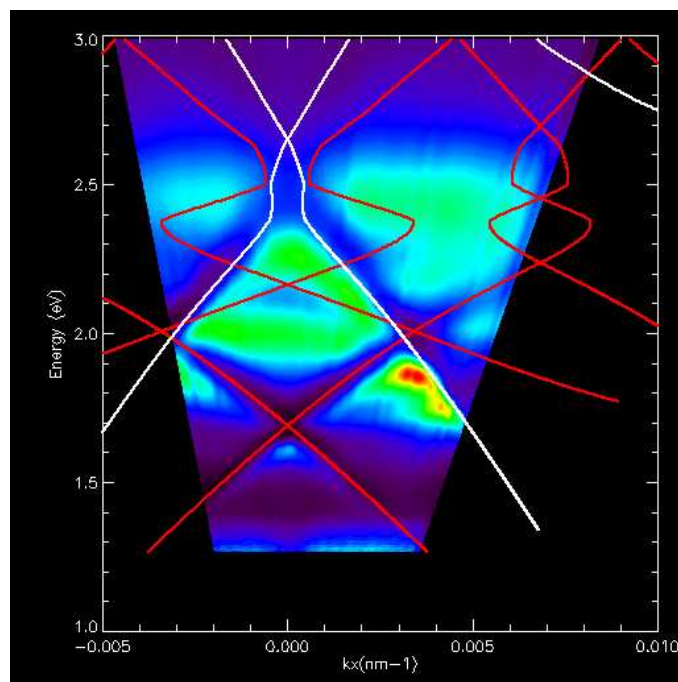


Figure 3.6: Dispersion of SP modes on a hole array. The hole array consists of 30×30 holes of diameter 150nm in a 180nm thick Au film with periodicity 460nm. The transmission spectra were acquired for different illumination angles by tilting the metal film with respect to the optical axis using polarized light normal to the rotation axis. The red and white lines correspond to the theoretical resonance position according to Eq.(3.3) and (3.6) for the metal-glass and metal-air interface respectively.

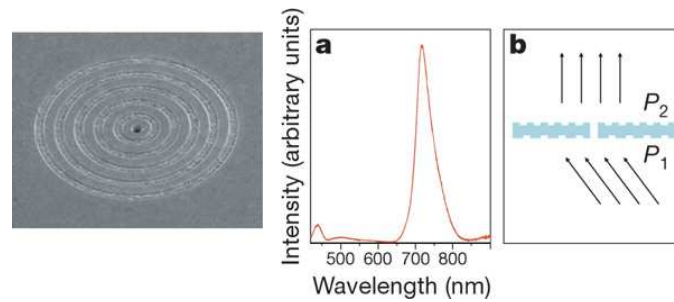


Figure 3.7: (a) Transmission spectrum of a single hole surrounded by periodic corrugations (left) prepared by focused ion beam (hole diameter 300nm, period 650nm). b, Schematic illustration of redirecting beam by single-slit aperture surrounded by grooves of different periodicity on the input (P_1) and output (P_2) surfaces (taken from [45]).

transmission, the reflection spectrum can also provide valuable insight into the phenomenon. Different studies [46, 79, 84] have shown that transmission peaks are associated with minima in the corresponding reflection spectrum. By combining the information based on the transmitted and reflected light, it is possible to relate the enhanced transmission to enhanced absorption and thus confirming the fundamental role of the SP modes in the EOT process.

It should be noted that EOT can also be observed in other configurations than hole arrays. For instance the 1D counterpart of a hole array consisting of an array of subwavelength slits also features high SP-related transmission peaks [85–87]. In this case, SP excitation and the resulting EOT is very sensitive to the polarization [85]. The slit is propagative for perpendicular polarization and it sustains Fabry-Perot modes which enrich the transmission phenomenon.

Furthermore if a single hole is placed in an array of dimples [88, 89] or surrounded by periodic grooves [45, 89–91], it is possible to enhance the transmission through the single aperture as illustrated in Fig. 3.7. This effect can be related to surface plasmon resonances at the surface. As illustrated in Fig. 3.8, the grating converts the incoming light to SPs which concentrate the electromagnetic field above the hole enhancing the transmission. The resonance condition is determined by the grating period P and the dielectric properties of the interface (metal: complex ϵ_m and dielectric : real ϵ_d) as in the case of hole arrays and can be approximated by the formula:

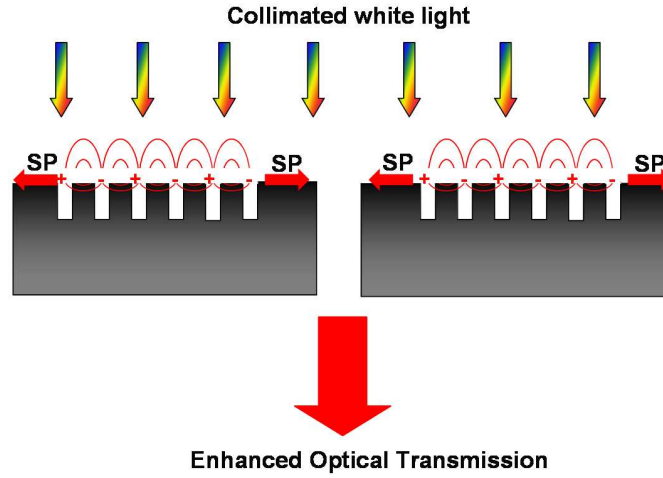


Figure 3.8: Enhanced transmission through a bull's eye structure.

$$\lambda_{sp} = P \sqrt{\frac{\epsilon_m \epsilon_d}{\epsilon_m + \epsilon_d}} \quad (3.8)$$

The corresponding 1-D configuration is also possible by combining a single slit with linear grooves [92]. Of particular interest are the effects of such corrugations on the emission pattern of single holes. As will be discussed in more detail in Chapter 6, the grating at the exit side on a single aperture leads to interesting beaming effects [93–95].

3.3 Other parameters influencing the transmission

Although the SP resonance condition is to a large extent determined by the periodicity of the grating, the enhanced transmission also strongly depends on other array characteristics.

As already discussed in Chapter 2, existence and propagation of SP waves is only possible if certain conditions imposed on the interface are met. Experimental and theoretical studies [96–100] have addressed the role of the metal on the SP properties. As can be seen on Fig. 3.9, noble metals such as Au, Cu or Ag lead to high peak intensities in the visible/near IR range, whereas the transmission signals

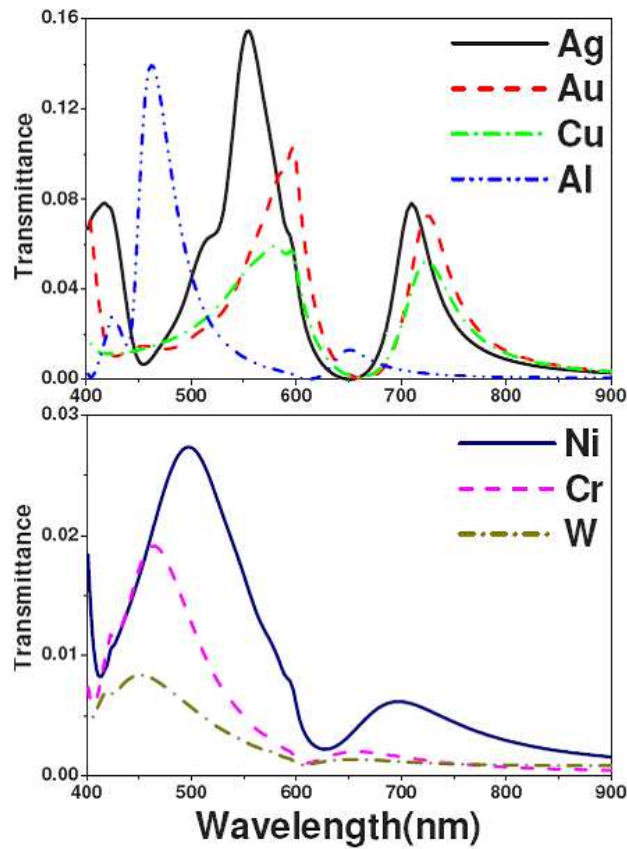


Figure 3.9: Simulated transmission spectra for holes arrays milled in different metallic films (taken from [100]).

are much weaker for transition metals (Ni, W, Cr). In the UV part of the spectrum, Al is a good choice for enhanced transmission [100, 101]. We stress here that for a given wavelength of interest, the choice of the metal can be crucial and that EOT is only possible for a metal presenting the right dielectric properties.

Furthermore the overall size of the hole array, i.e. the number of holes, also influences the transmission [72]. In particular the peak intensities increase with the hole array until a saturation occurs which depends on the size of the individual holes. This is related to the propagation length of the SPs on such an array, which is higher for the smaller holes enabling many more holes to contribute to the plasmonic field in the array.

Various studies [102–105] have also addressed the influence of the aspect ratio (h/d) of the holes on the transmittance. For instance if the film is sufficiently

thin and the two dielectric media have the same dielectric properties, the modes on either side of the metal film can couple and lead to the appearance of 2 new transmission peaks [103]. For thicker films or non-symmetric dielectric environment, increasing the hole size generally leads to a higher transmission and a redshift of the peaks [72, 102, 103, 105]. In Chapter 5, such variations are discussed in more detail in the specific context when the hole diameter changes relative to the cutoff wavelength.

As the transmission spectrum depends on the size of the holes, it is not surprising that their shape also significantly modifies the transmittance. This can be related to various contributions: first, the cutoff attenuation of the hole is modified [57–59, 67, 68] and secondly, localized modes emerge at the individual holes [57, 66]. Such effects related to the hole geometry are much more important if only one hole is considered as in the absence of a delocalized SP mode resulting from an array, the transmission properties depend solely on the features of the single aperture. Different theoretical studies [65–69] have addressed this issue and it has been shown that optical behavior of subwavelength apertures is more complicated than Bethe’s dipole model. Such results on the spectral behavior of individual apertures have also motivated the study presented in Chapter 6.

Chapter 4

Description of the experimental procedures

In this chapter we will describe the different experimental setups and procedures involved in the present thesis. This starts with the preparation of metal films through sputtering. In a second step they are structured using FIB milling. Finally they are optically characterized through the acquisition of transmission spectra. We also define the different figures of merit that are used to evaluate the data.

4.1 Preparing the metal films

All the metal films were deposited on glass substrates. These substrates, which typically consist of 1 mm thick microscope slides, are cleaned in progressive ultrasound baths with a commercially available soap (Hellmannex II), purified water and pure ethanol. After rinsing them again in purified water, they are dried before the deposition. This cleaning procedure is necessary as any dirt or impurity present on the substrate will result in roughness for the metal film and consequently limit the propagation of SPs.

The metal films are deposited on the cleaned substrates using the Emitech K575x magnetron DC sputterer shown in Fig. 4.1. Inside the vacuum chamber of the sputterer, a metallic target (in our case mostly Au or Ag) is fixed to a Peltier cooled cathode, on which a tension of several kV can be applied. The substrate is positioned at a second electrode (the anode), situated only a couple of centimeters away from the target. Argon gaz is then introduced into the chamber and at low



Figure 4.1: Emitech K575x Turbo Sputter Coater during deposition.

pressure ($9 \cdot 10^{-3} \text{ mbar}$) a potential difference is applied between the electrodes. This generates a plasma by ionizing the gas. Under the effect of the electric field, the ions are accelerated towards the target from which they eject metal atoms upon impact. The ejected metal then deposits everywhere inside the chamber, in particular on the sample. The flux of argon ions on the target is controlled through 2 concentric magnets. This magnetron system enables high quality sputtering at low vacuum. Another important feature is the fact that the sample stage is cooled by a water circuit making sure the temperature fluctuations are kept to a minimum during sputtering.

The roughness of the sputtered films was characterized by AFM measurements and was found to be below 1 nm rms. This very low roughness ensures that surface wave can propagate with minimal scattering.

4.2 Nanostructuring using FIB

The different structures that are presented in this work were all fabricated using focused-ion-beam (FIB) milling. For this purpose, our laboratory disposes of a FEI DualBeam FIB/SEM Strada 235 shown in Fig. 4.2. In addition to the ion beam,

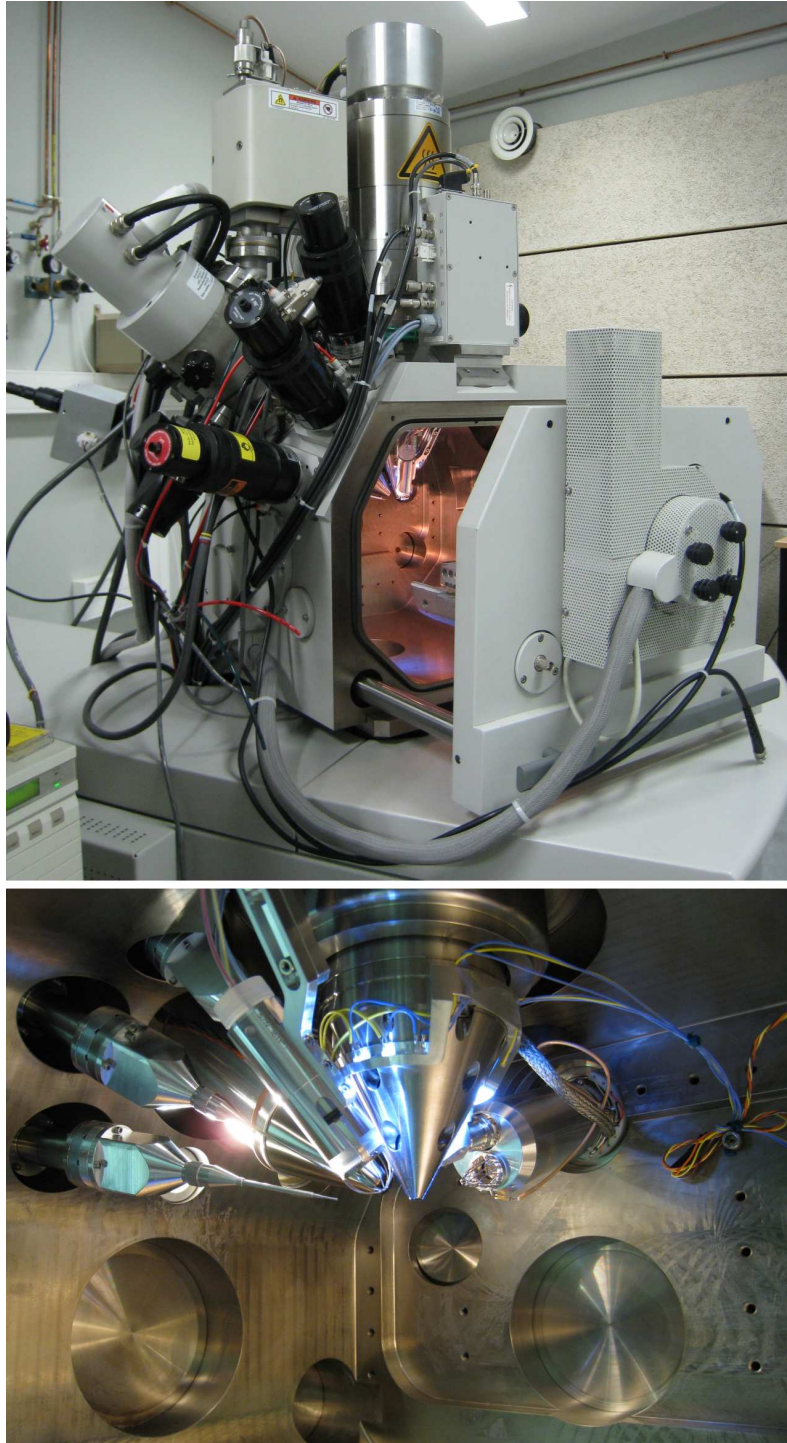


Figure 4.2: FEI DualBeam Strada 235. (a) Outside of the FIB chamber with the E-Beam (top) and I-Beam (at 52) columns as well as different gas injectors (b) inside of the chamber with the tips of the E-Beam and I-Beam columns as well as different injectors and detectors.

this particular model includes an electron beam which enables SEM imaging in the same vacuum chamber.

The milling with a FIB system relies on the impact of highly accelerated Ga^+ ions on the metal surface. The ions are extracted from a liquid metal ion source ("LMIS"), accelerated by a high tension to an energy around $30keV$ and focused by several electrostatic lenses. The intensity and beam width can be adjusted using several diaphragms.

It should be noted that the impact of the beam on the surface generates signals that can be collected using different detectors for imaging purposes. This is based on the same fundamental principle as the scanning electron microscopy (SEM). However when scanning a metal surface, the ion beam damages the surface much more than an electron beam.

In order to mill the different structures, the movement of the ion beam needs to be precisely controlled. This is achieved through stream files (see Fig. 4.3) which basically consist of pixel coordinates telling the machine which pixels are milled and which are to be left untouched. The choice of the different parameters that are selected during this preliminary programming is crucial for the the quality of structures. Furthermore during the milling, the I-Beam current, the magnification and the number of times each pixel is milled also need proper adjustment according to film thickness and structure size. For all these reasons a number of tests are required to balance these different parameters. When the whole system is properly configured, high quality structures can milled as can be seen on the SEM image in Fig. 4.4.

4.3 Acquisition of transmission spectra

As discussed in the previous chapter, the study of the transmission is of particular interest for nanostructures such as hole arrays. The acquisition of transmission spectra is realized using an inverted microscope (Nikon TE 200), which is connected to a spectrometer (Acton SpectraPro 300i) and a Si charge-coupled-device (CCD) (Princeton Instrument VersArray 1300B).

For the measurements, the structure is aligned on the optical axis of the microscope and illuminated with collimated white light. The light transmitted by the nanostructure is then collected using a microscope objective. Here a difference

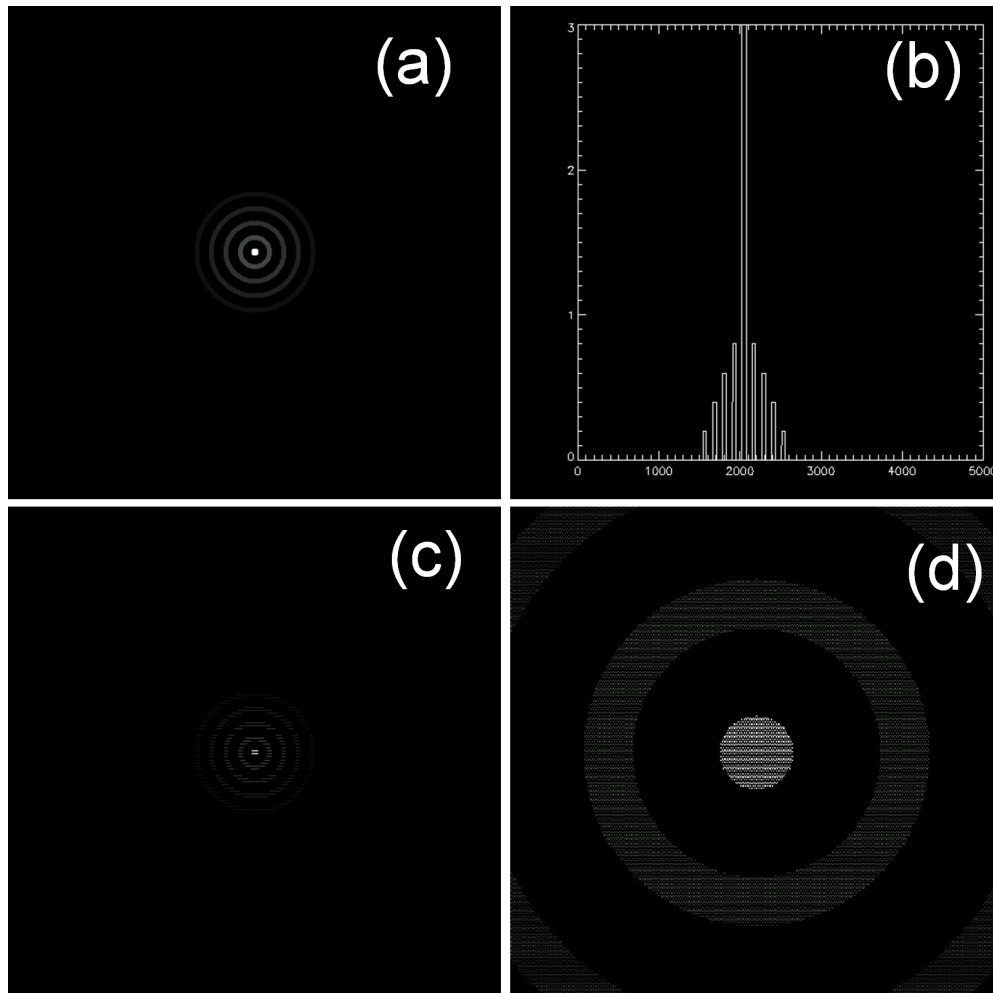


Figure 4.3: The different steps of streamfile programming. (a) First the structure to be milled (in this case a bull's eye , i.e. a hole with concentric grooves) is defined, with different pixel densities (represented as different shades of gray) for different milling depths (grooves get shallower with distance from centre). (b) crosscut of the defined structure, illustrating the different depths of the hole and the grooves (c) same structure when pixelized (d) close up of the central hole (the pixelization is not to scale as the real structure is defined over a matrix of 4096x4096 pixels and had to be resized for this illustration).

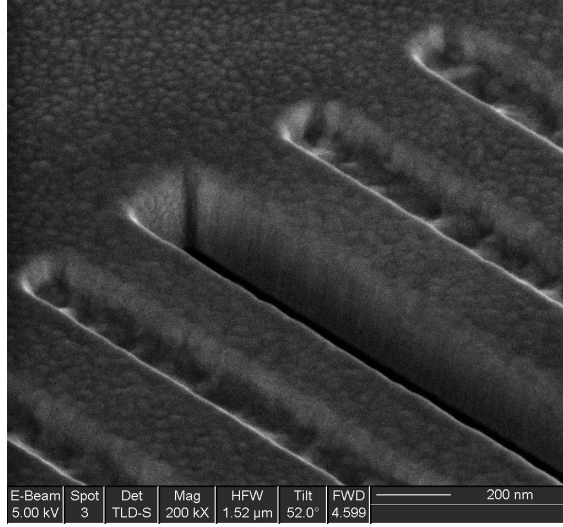


Figure 4.4: Nanostructure milled by FIB in a 250nm thick Au film. The structure from which only one end is visible consists of a slit (width 200nm) surrounded by periodic grooves (period 550nm) of depth 80nm and width 150nm. The crystalline structure of the metal film is visible.

needs to be made between arrays and single aperture structures. The transmission through arrays leads to the emergence of a plane wave that can be entirely collected by the microscope objective in the case of the lowest energy peak since it only gives rise to zero order diffraction. However single aperture structures diffract the light [56, 72] and consequently not all the emitted light can be collected due to the low numerical aperture (NA) of the objective. This needs to be considered when evaluating the transmission intensity of such structures.

The maximum angle θ of the collected solid angle Ω can be deduced from the NA:

$$NA = n \sin \theta \quad (4.1)$$

and the solid angle Ω is then given by:

$$\Omega = 2\pi(1 - \cos \theta) = 2\pi \left(1 - \cos \left(\arcsin \frac{NA}{n} \right) \right) \quad (4.2)$$

where n is the refractive index of the medium through which the light is collected. However most samples are measured through a glass substrates, which means that

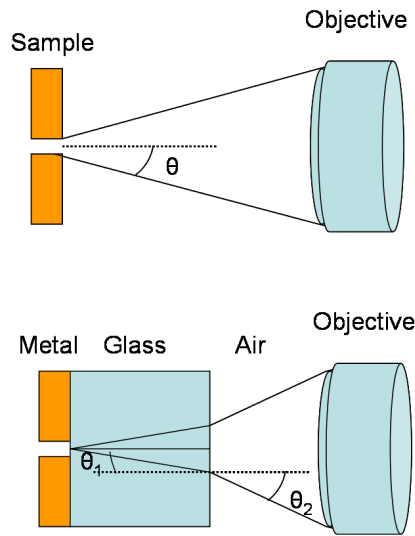


Figure 4.5: Solid angle of collection for a small aperture, whose transmission is measured directly (upper figure) or through a glass substrate.

the light that is emitted by the structures gets refracted at the interface between the glass (refractive index n_1) and the air (refractive index n_2) (see Fig. 4.5). In this case the solid angle of collection of the objective (θ_2) is different from the solid angle of the transmission (θ_1), but it can be determined using the Snell-Descartes law of refraction and the numerical aperture of the objective:

$$n_1 \sin \theta_1 = n_2 \sin \theta_2 = NA \quad (4.3)$$

In this case the solid angle of collection is given by:

$$\Omega = 2\pi(1 - \cos \theta_1) = 2\pi \left(1 - \cos \left(\arcsin \frac{NA}{n_1} \right) \right) \quad (4.4)$$

For the 2 different objectives that were used (Nikon Plan Fluor 40x and 20x), the different solid angles and also the ratio between the collected solid angle and the total solid angle are shown in table 1.

	NA	direct measurement			through Glass substrate		
		θ	Ω	Collection %	θ_1	Ω	Collection %
20x	0.45	0.47	0.67	10.7%	0.30	0.29	4.61%
40x	0.60	0.64	1.26	20%	0.41	0.52	8.35%

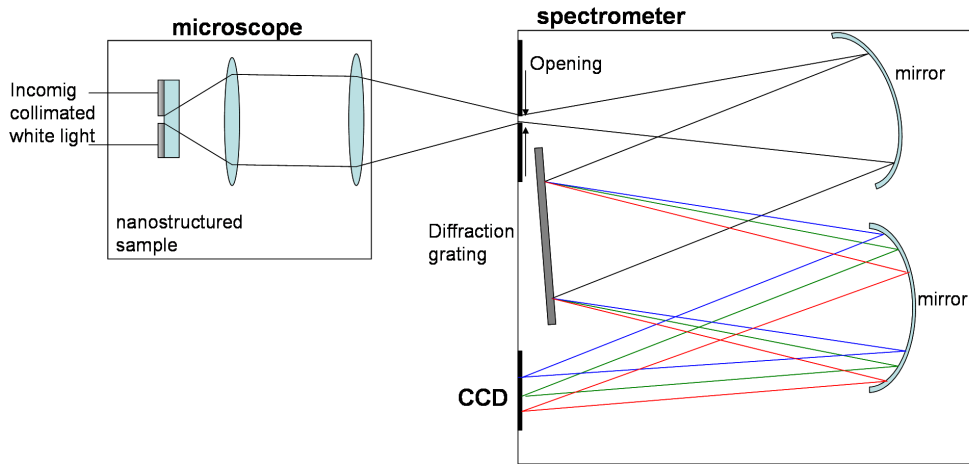


Figure 4.6: Microscope coupled to spectrometer and CCD. The light emitted from the structure is spectrally resolved by the Czerny-Turner monochromator and acquired by the CCD.

Based on the small collection % of this setup (8% for structure on glass substrate and 40x objective), the raw intensities collected by the objective are strongly underestimated. However it is clear that precise knowledge of the diffractive properties of single apertures is also needed to properly evaluate the transmission of such structures (Chapter 6).

For each structure, the light collected by the objective forms an enlarged image at the entrance slits of the spectrometer. The width of this opening can be adjusted to change the window of detection and the resolution of the apparatus. Our spectrometer is designed following the Czerny-Turner configuration as illustrated in Fig. 4.6: The light passing through the slits is first reflected on a mirror before being diffracted by a grating. Using a second mirror the dispersed light is redirected to the CCD. Furthermore, a small motor inside the spectrometer can be used to change the position of the grating such that a non dispersive order is imaged on the next mirror. In this case, the system can be used for imaging purposes and it is a useful tool to precisely align and focus the structure on the CCD.

The dispersion curves of SP on hole arrays can be measured with the same microscope and spectrometer/CCD. In this case, the sample is mounted on a goniometer which enables the rotation of the sample with respect to the optical path.

The maximum rotation that can be achieved is in this case limited by practical experimental issues such as the sample touching the objective during the measurement. That is why in this case it is preferable to use an objective with a larger working distance.

In order to evaluate the transmission efficiency of nanostructures, we stress the importance of clearly defined figures of merit in addition to the precise experimental procedure. In our study there are two different figures of merit that are used to quantify the transmission.

The first is the intensity "normalized-to-area" (INTA) and defines the ratio between the light that illuminates an aperture and the light that is emitted by the structure. We emphasize the fact that in this case only the light illuminating the aperture is considered and not that impinging on the surrounding metal. Physically this intensity corresponds to a scattering cross section and is dimensionless. In certain cases this INTA can be larger than unity, giving rise to the EOT. It is also interesting to characterize the absolute transmission of aperture arrays. It is generally given in percent and corresponds to the ratio between the light that is transmitted by apertures and the total amount of light that impinges on the structure. In summary these figures of merit are especially important to characterize the photon sorting structures in Chapter 7.

Chapter 5

Enhanced optical transmission at the cutoff transition

As discussed in Chapter 3, over the past decade hole arrays in metal films have been extensively studied both for fundamental issues and for their potential applications in a variety of fields [40, 43, 45, 106–108]. Nevertheless there are still some aspects that are not yet fully understood requiring detailed experimental and theoretical studies. For instance, the EOT phenomenon has been analyzed generally in the limit of hole diameters small compared to the resonance wavelength. In this subwavelength regime, it has been shown that the electromagnetic fields decay exponentially inside the hole with the hole depth [102, 103]. For holes large compared to the wavelength, light can propagate freely through the holes. The transition between these two regimes is defined by the cutoff conditions of the aperture which has been far less studied [76, 109].

In this chapter we analyze the EOT through this transition. For this purpose, the hole diameter is varied relative to the period and therefore to the transmission peak wavelength of the array. By repeating such measurements for different hole depths and by analyzing the results according to different models, the underlying physics of the transition is revealed. Among other things, the optimal condition for surface plasmon excitation are found at the cutoff which is important for designing structures for many applications.

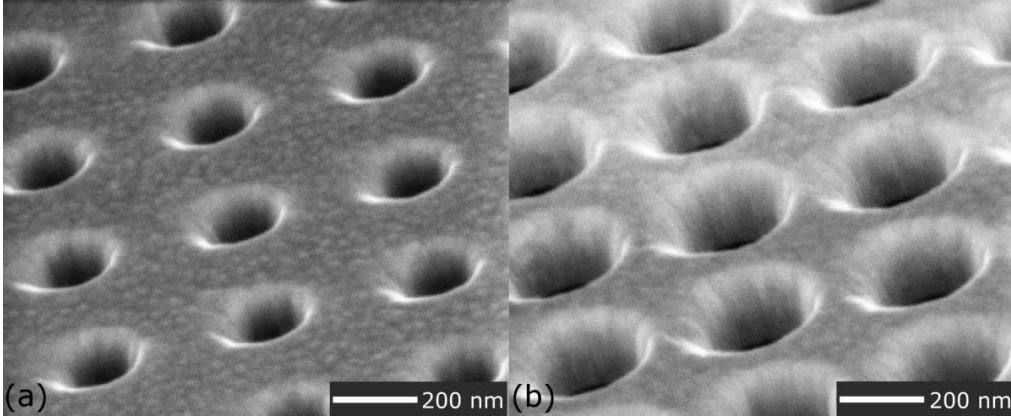


Figure 5.1: SEM images (magnification 65kx) of holes in a square array (period $P = 460\text{nm}$) made from 30×30 holes, milled through a 260nm thick Au film, with hole diameters $d = 150\text{nm}$ (a) and $d = 250\text{nm}$ (b).

5.1 Optical characterization of hole arrays

In this study, the hole arrays are milled in a Au film deposited on a glass substrate using the FIB as discussed in Chapter 4. As can be seen on Fig. 5.1, the holes are not perfectly cylindrical, but have a slightly conical form. This is related to the fact that during milling, part of the ejected metal can redeposit inside the hole. By measuring cross-sections of the holes it was possible to estimate an error of $\pm 5\%$ for the hole diameter. Array period was fixed at 460nm and the hole diameter for each array was gradually increased from 100 to 400nm for various film thickness.

The asymmetric dielectric environment (i.e. the dielectric media on both sides of the film are different, air and glass) ensures that longest wavelength SP mode is spectrally isolated. This avoids the additional variable introduced by coupling between modes of the two interfaces [102–104].

The transmission spectra recorded for a given hole depth h are shown in Fig. 5.2. Such spectra are characterized by a set of peaks as explained in Chapter 3 and we will focus on the one corresponding to the $(i, j) = (1, 0)$ mode of the glass-metal interface for the reasons just discussed. The peak intensity increases with the hole diameter and the peak position shifts first to the red. For the hole diameters larger than 250nm , the peaks broaden and appear to double.

The dispersion curves of the SPs on such arrays were also analyzed to better understand the spectra [41, 79, 83]. This was achieved by measuring the transmit-

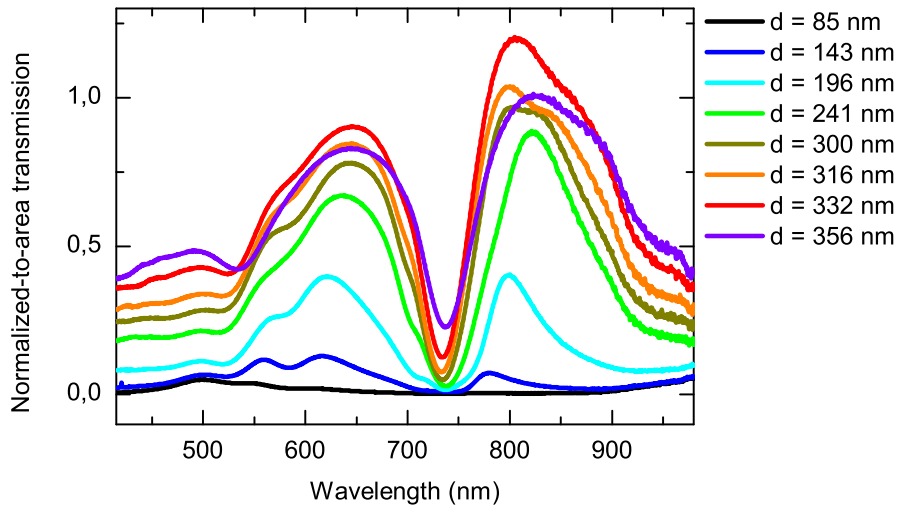


Figure 5.2: Normalized transmission spectra of square arrays of circular holes (30×30 holes) with a period of 460 nm milled through an Au film of thickness 180 nm deposited on a glass substrate. The color scale corresponds to different hole diameters.

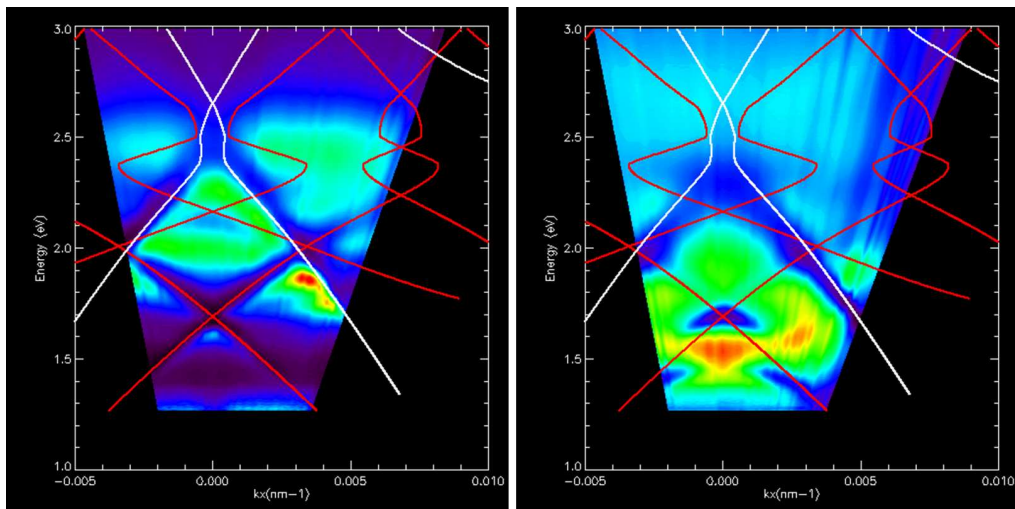


Figure 5.3: Dispersion curves ($I = f(E, k_x)$) of different hole arrays (period $P = 460 \text{ nm}$) in a metal film deposited on a glass substrate together with the theoretical peak positions for the metal-air (white line) and the metal-glass (red-line) interface as explained in Appendix A. (a) hole diameter $d = 150 \text{ nm}$, hole depth $h = 180 \text{ nm}$, (b) $d = 350 \text{ nm}$ and $h = 180 \text{ nm}$. The color scale is different for each dispersion curve and optimized to produce the best possible contrast. For the corresponding intensities of the different curves the reader is referred to Fig. 5.2 and 5.4.

tance while rotating the sample with respect to the optical axis and the acquired data points were processed as explained in Appendix A. The corresponding data are shown in Fig. 5.3 together with the theoretical resonance positions for two hole arrays having different hole diameters. As can be seen in Fig. 5.3, the theoretical resonance positions are in very good agreement with the minima and this is observed for all the modes on the different hole arrays. The experimental maxima are typically redshifted compared to the calculated values and this can be explained by a Fano-type coupling between the direct and indirect (SP) contributions to the transmission as will be discussed in detail further down [73–75]. For the larger hole diameter in Fig. 5.3, the high energy peak becomes dominant and a non dispersive mode appears around 1.55eV. This is a signature of a localized mode related to the hole and not to the array. It further coincides with the presence of a double peak in the normal incidence spectra in Fig. 5.2 for similar hole diameters. These observations could be explained by a localized mode emerging for these specific parameter values. Although such localized effects are of much higher importance in the context of individual holes [56, 65, 66, 68, 110], it is to be expected that they affect in some way the transmission through arrays of holes. It is possible that the (1,0) SP mode is coupling with this localized one in a similar way as can be observed for delocalized SPs on opposite sides of hole arrays [102, 103]. Further experiments beyond the scope of this study would be necessary to analyze this spectral feature and determine if there is any coupling.

Next we focus our study on the evolution of the transmission intensity as a function of hole diameter. Since the transmission also depends strongly on the hole depth [102], measurements such as those in Fig. 5.2 were repeated for a large range of film thicknesses (hole depths) $h = 140 - 560\text{nm}$. In Fig. 5.4, the (1,0) transmission peak intensity has been plotted as a function of the hole diameter for each hole depth. These curves show a sigmoidal shape with 0 and 1 as the natural limits when the hole area becomes respectively very small and very large as compared to the period. For the thinner films, the transmission can exceed unity before dropping back to 1 as the holes diameter approaches the period. Some modulation are apparent in the curves and will be discussed in more detail later. As the films become thicker, the transmission is strongly reduced. Next we analyze these evolutions using different models.

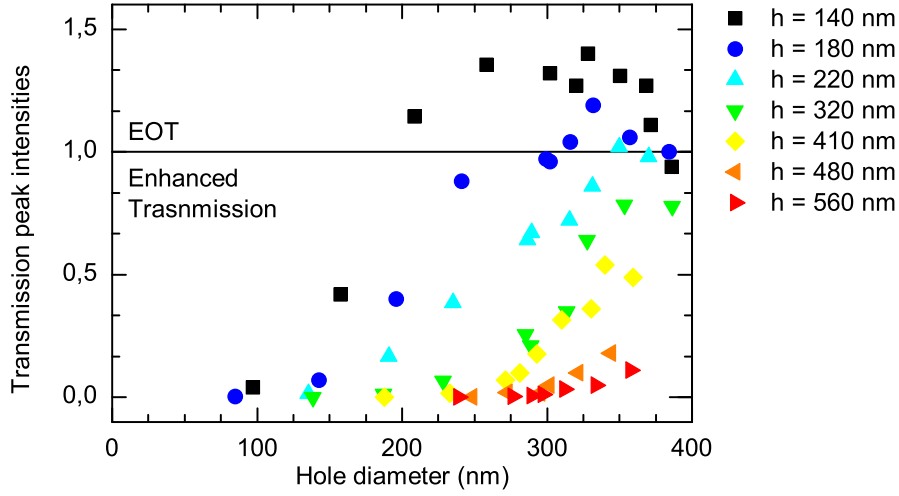


Figure 5.4: Normalized transmission peak intensities associated to the $(1, 0)$ SP mode excited on the metal-glass interface for different film thickness h as a function of hole diameter. This resonance enhances the transmission through the holes. For certain arrays, the normalized transmission can exceed unity (black horizontal line): the regime of EOT.

5.2 The nanohole as a waveguide

A simple waveguide model can already help in understanding the evolution of peak intensities of Fig. 5.4. Considering each hole as a waveguide of diameter d in a perfect metal conductor (PEC), the transmission is determined by guided modes and the associated wavevectors. Of particular interest are the modes for which the electric (TE modes) or the magnetic (TM modes) field has only a transverse component. Furthermore in our case the holes are small compared to the wavelength and consequently the fundamental modes dominate the process. Therefore we only need to consider the corresponding wavevectors which can be determined from Maxwell's equations [61, 111]:

$$k = \sqrt{\left(\frac{2\pi}{\lambda}\right)^2 - \left(\frac{2z}{d}\right)^2} \quad (5.1)$$

In this case the solutions depend on the roots z of Bessel functions, and for the fundamental modes corresponds to 1.841 ($TE_{1,1}$ mode) or 2.405 ($TM_{0,1}$ mode) [61].

The cutoff condition which is defined by the solution $k = 0$ links the incident

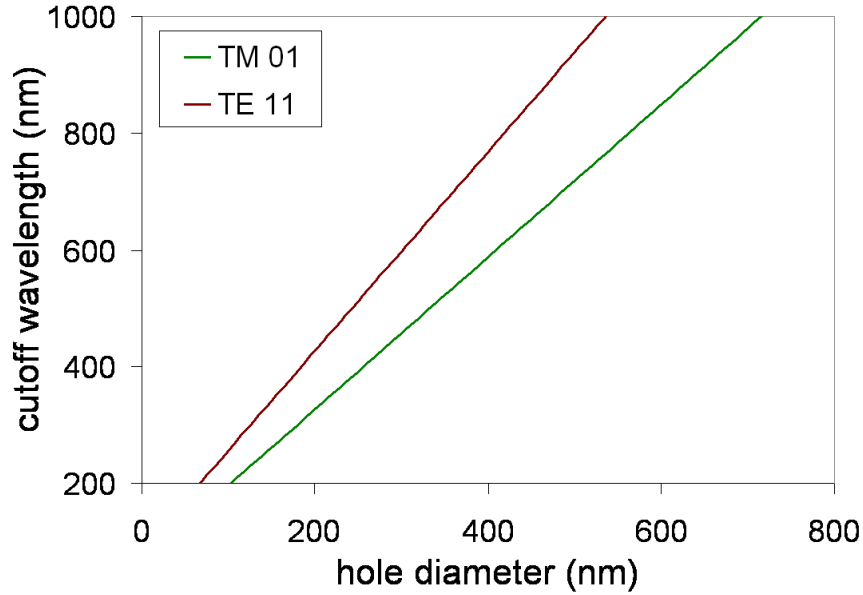


Figure 5.5: Cutoff wavelength as a function of hole diameter for the $TE_{1,1}$ and $TM_{0,1}$ modes in a circular waveguide.

wavelength λ and the hole diameter d of the guide as shown in Fig. 5.5. The fundamental mode in our case corresponds to the TE_{11} mode, as it has the smallest cutoff diameter ($d_c = \lambda z / \pi$) for a given wavelength. From this plot, it is easy to see for a given λ and d whether the hole is below or above the cutoff. Consequently the mode is either propagating when k is real or evanescent when k turns imaginary. In this work, we essentially follow a given resonance (fixed λ_{res}) and approach the cutoff condition by progressively increasing the hole diameter. We define the transmission T as the ratio between the input and output fluxes of the Poynting vector of a plane wave through such a waveguide. In other words, the holes are considered isolated and all the implications of the holes forming an array are knowingly neglected. The transmission for diameters smaller than d_c is mainly governed by how the electromagnetic field is attenuated inside the guide as a function of diameter and depth, whereas above d_c all the light that enters the holes is transmitted. To account for the penetration of the electromagnetic field into the metal, we increase the diameter d of each waveguide by twice the corresponding skin depth ($2s_d$) evaluated at λ_{res} , while we still use the real hole diameter to determine the input

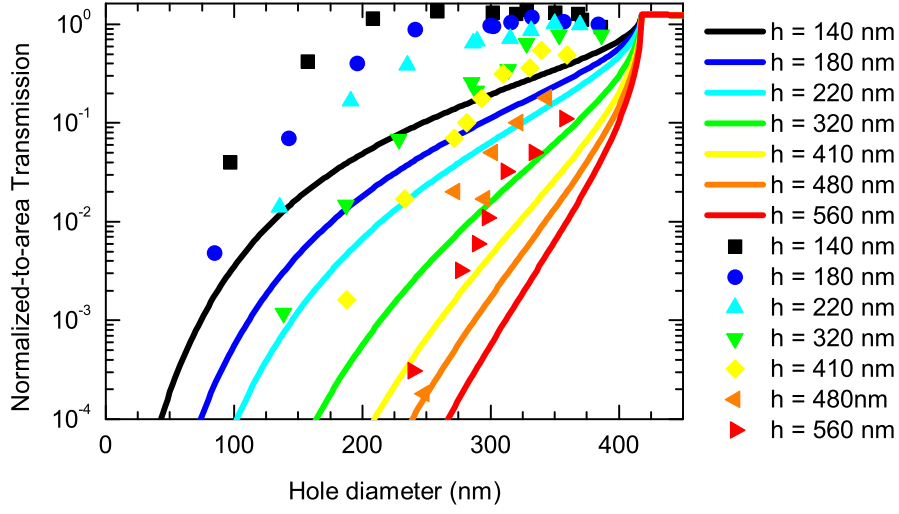


Figure 5.6: Normalized transmission peak intensities that were measured for varying hole diameters and depths. The continuous lines give the transmission expected through subwavelength cylindrical waveguides at 800nm, as given by Eq.(5.2).

flux in order to have the same normalization as for our experimental data. The transmission T is then given by:

$$T = \begin{cases} \frac{(d+2s_d)^2}{d^2} e^{-2\sqrt{\left(\frac{2z}{d+2s_d}\right)^2 - \left(\frac{2\pi}{\lambda_{res}}\right)^2} h} & \text{if } d < d_c \\ \frac{(d+2s_d)^2}{d^2} & \text{if } d > d_c \end{cases} \quad (5.2)$$

In Fig. 5.6, the transmission peak intensities that were measured for different hole diameters and depths are plotted on a logarithmic scale together with the calculated transmissions through subwavelength cylindrical waveguides following Eq.(5.2). In this classical analysis, all the calculated curves meet at the cutoff (~ 410 nm hole diameter) which is larger than all the experimental hole diameters. The general evolution of the curves follows well the trends of the experimental data, especially in the limit of films which are thick compared to the hole diameter. Nevertheless, the transmission intensities found from the calculation are 2-3 orders of magnitude smaller than what is measured in the experiments.

More sophisticated waveguide models than Eq.(5.2) have been proposed to describe the optical behavior of holes in metal films. For instance Catrysse *et al.* [112] studied the effect of a plasmonic metal on the propagating modes inside a cylindrical hole. In the range of wavelength and hole diameters considered in our study, their

results indicate that the plasmonic metal does not change the underlying physics of the waveguiding process, but merely leads to a shift in the cutoff to smaller radii. It should however be noted that one important limitation of their model is the neglect of losses in the metal. Other studies [67,68] have addressed the modes at the cutoff in a real metal, but the considered hole shapes do not apply directly to the present data.

Most importantly, our waveguide approach does not include collective effects which is precisely why arrays of holes, having SP resonances, generate far higher transmissions than single apertures as the comparison in Fig. 5.6 shows.

5.3 Fano analysis

Although the general evolution of the intensities at resonance seems to follow a waveguide behavior, it is obvious that it is not possible to explain this complex phenomena thoroughly without considering the influence of SP modes excited at the surface of the array. This is particularly clear for the small depths (see Fig. 5.2 and 5.6). At this point the SPs induced by the periodicity of the holes are considered together with the direct scattering generated by each hole. In fact, the transmission process through an array of holes can be seen as an interference between a non-resonant contribution given by the transmission through each hole, taken as isolated, and a resonant contribution stemming from the excitation of an SP mode. This contribution amounts to a coupling between the holes in the extended array [73–77,113]. This picture clearly oversimplifies the problem as supplementary contributions do affect the phenomenon [68,114], but yet, it can provide some interesting insight into the transmission process as we will see below.

As in our study we concentrated on the most isolated mode $(1,0)$, we only need to consider one SP resonance. This interference broadens the resonance and shifts its spectral position in the transmission spectrum (Fano-type redshift). The resonance width Γ is related to the lifetime of the SP mode and as such to the propagation length of the surface plasmon on the array. As the scattering of the excited SP mode on the holes induces radiative loss and limits the SP propagation, Γ is a direct measure of the coupling strength between the resonant SP contribution and the non-resonant one. The stronger the SP scatters on the holes, the shorter its lifetime and the smaller its propagation length.

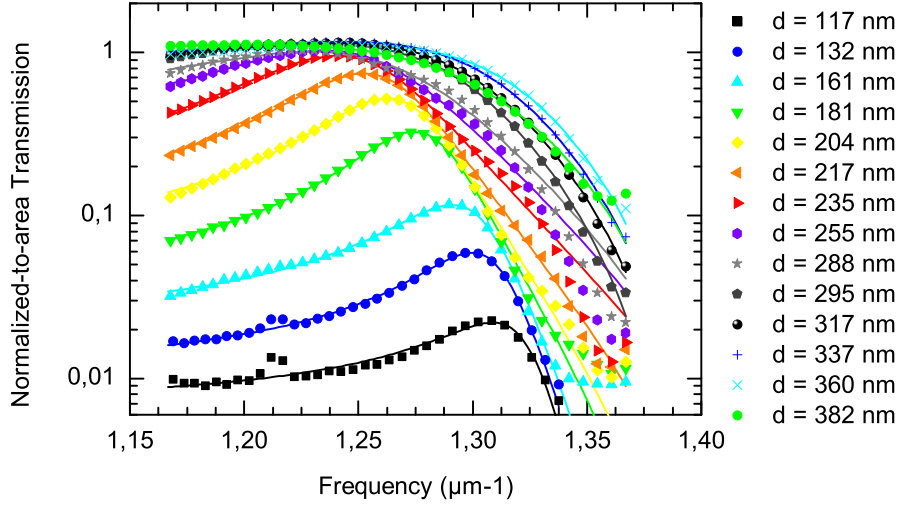


Figure 5.7: Normalized transmission spectra measured for different hole diameters in a 190nm thin Au film deposited on a glass substrate. The numbers on the right-hand side of the graph give hole diameters in nanometers. In the chosen spectral bandwidth, each spectrum is fitted using Eq.(5.3).

Following this picture and as detailed in [74,75], the profile of the transmission coefficient T takes the specific shape as a function of the frequency ω of the field:

$$T = \alpha \frac{[\omega - (\omega_0 + \Delta) - \rho]^2}{[\omega - (\omega_0 + \Delta)]^2 + \Gamma^2}. \quad (5.3)$$

Here, ω_0 corresponds to the natural (uncoupled) SP resonance, as given by Eq.(3.6) and Δ to the shift from this position. The parameter ρ corresponds to the ratio of the strengths from both contributions. The global prefactor α is proportional to the transmittance of the isolated hole. When accounting for the interplay between the two contributions, the shift Δ and the width Γ (FWHM) of the resonance are related through a dispersion relation:

$$\Delta_\omega = \frac{1}{2\pi} P \int d\omega' \frac{\Gamma_{\omega'}}{\omega - \omega'}. \quad (5.4)$$

It should be noted that the formula given by Eq.(5.3) closely resembles other formulas that have been used to describe this interaction [75–77,113]. The approach originally proposed by Kim et al. [113] and used by de Dood et al. [77] has been proven very valuable as it can be extended to more than one resonant contribution.

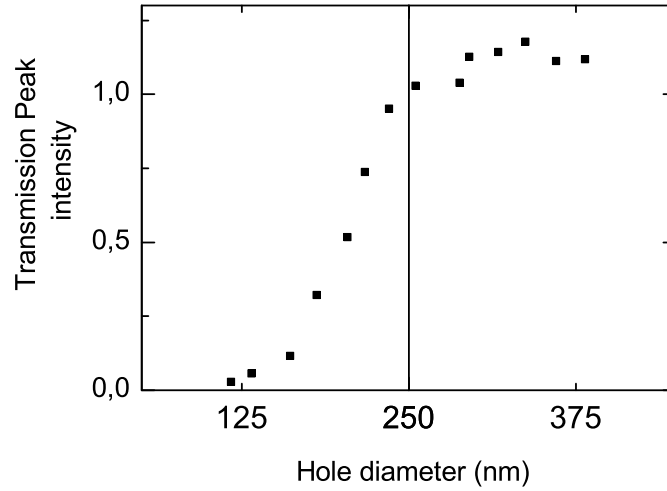


Figure 5.8: Normalized transmission peak intensity measured as a function of hole diameter.

However by comparing their formula with ours, we found that a supplementary parameter appeared in their model, related to the phase difference between both contributions. As we understand it, this phase factor is already accounted for by Fano through his rigorous calculation [73] and hence reduces the number of parameters in our model which follows closely Fano's original description. The approach presented by Bravo *et al.* [76] relies on the same basic principles and clearly details how the electromagnetic field amplitude as a single hole is to be modified when this holes is placed in a 2D array. This theoretical approach eventually distinguishes between a resonant and an interference contribution in terms of field amplitude which we can not access in our experimental study. However, as we will see below, the spectral results of the simulations by Bravo *et al.* do compare well with our experimental results.

We now use our model given by Eq.(5.3) to fit the transmission spectra that were measured for hole arrays defined with different hole diameters at a given hole depth ($h = 190\text{nm}$), taking α , ρ , Γ and Δ as independent parameters. As can be seen in Fig. 5.7, the experimental curves can be fitted for the whole range of hole diameters. Nevertheless at high frequencies, Eq.(5.3) doesn't provide such a good fit of the data. We relate this to the emergence of other SP resonances, which are not accounted for in our fitting formula limited to a single resonance.

Figure 5.8 displays the variation of the transmission peak intensity as a function

of the hole diameter. It increases with the hole diameter until about 250nm, from where it starts to saturate. First assuming the peak positions as globally stationary as the holes get larger, the data shown on Fig. 5.8 is grossly reminiscent of what is expected for a waveguide with a cutoff diameter around 250nm (at a fixed wavelength).

This can be refined, by analyzing the evolution of all the fitting parameters. Their specific variations provides further evidence for a transition that occurs for hole diameters around 250nm for the chosen hole depth.

First, the resonance peak broadens with increasing hole diameter as can be seen in the resonance width Γ (Fig. 5.9a) which measures the coupling strength between the two contributions to the transmission process [74]. Widths broaden when the non-resonant contribution increases as the attenuation inside the waveguide is rapidly reduced when hole diameters approach the cutoff limit. Thus, a clear inflexion point of Γ is found around a diameter of 250nm. Simultaneously, the shift in the peak position Δ goes through a minimum as can be seen in Fig. 5.9b. It is interesting to note that the theoretical and experimental analysis of the EOT in the THz regime by Bravo *et al.* observed very similar peak shifts [76].

Interestingly, while these two parameters are adjusted independently from each other, they turn out to be related in a dispersive way. The evolution of the parameter Δ as a function of wavelength is related to Γ through Eq.(5.4). From our observations in the previous section, it is clear that the general evolution of the transmission follows the same trends as expected for a waveguide. If we now consider a spectral window that is small enough to neglect any dispersive effect of the Au film, the variation of the different parameters (and Γ in particular) as a function of hole diameter at a fixed resonance λ_{res} is expected to be equivalent to what is obtained by changing the resonance wavelength at fixed hole diameter. Hence the evolution of Δ and Γ as a function of the hole diameter at a fixed λ_{res} should also verify a similar relation as the one given in Eq.(5.4) for a fixed diameter d . To check this, we can approximate roughly the curve obtained for Γ by the *arctan* function given in Fig. 5.10(a). We computed the principal value integral for different distances to the central inflexion point of the *arctan* function and the corresponding results are plotted in Fig. 5.10(b). It is not surprising that the curve presents a minimum at the same position as the inflexion point of the *arctan* function exactly as can be observed in Fig. 5.9. The fact that the evolution of the fitted parameter

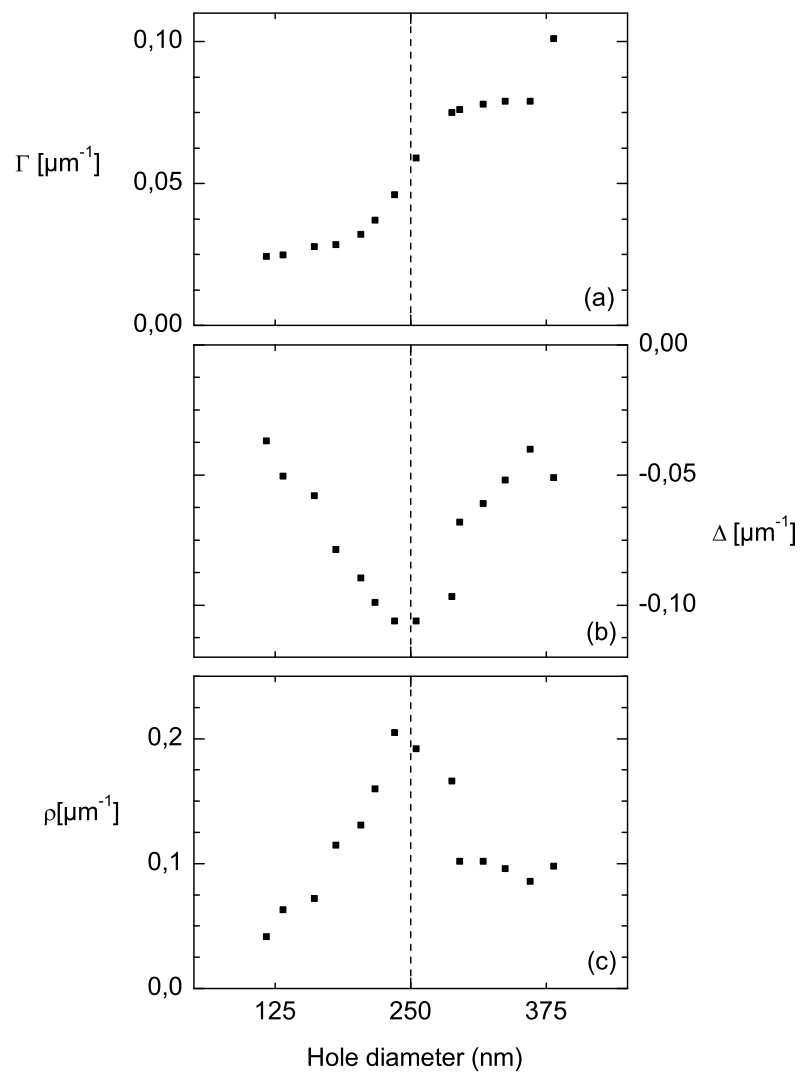


Figure 5.9: Evolution of the fitting parameters (a) width Γ (FWHM of the resonance), (b) spectral shifts Δ from the natural resonance position ω_0 and (c) strength ratio ρ between the two contributions as a function of the hole diameter.

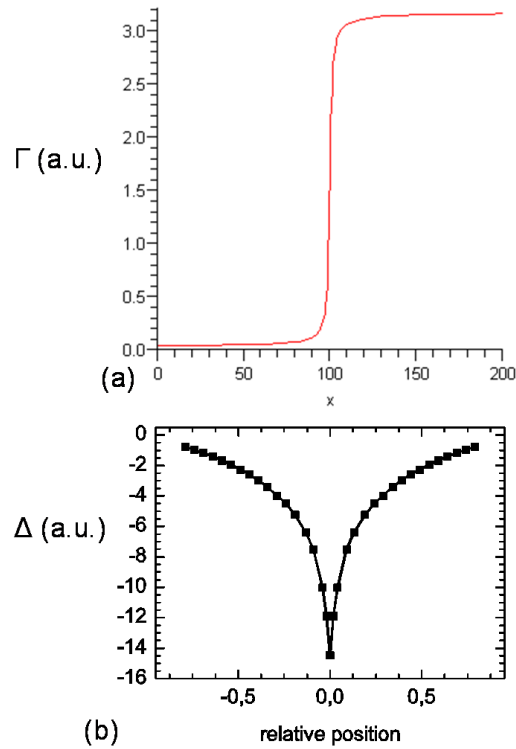


Figure 5.10: (a) The *arctan* function used to approximate the evolution of Γ shown in Fig. 5.9. (b) Evolution of Δ for a Γ function shown in (a), with the minimum position exactly at the same position than the inflexion point in the *arctan* function.

Δ corresponds closely to what is expected for the fits obtained for Γ shows that the dispersion relation given by Eq.(5.4) is still verified in our fit without being specifically accounted for. This coherence in our results validates our analysis and the observation of this cutoff transition.

The ratio between the SP contribution and the non-resonant transmission through the holes characterized by the ρ parameter is plotted in Fig. 5.9c and again has a clear maximum at 250nm. If the holes are small, the diffraction of the incoming light is weak and hence does not excite surface plasmons efficiently. With increasing hole diameter, the coupling between the incoming light and the SP waves increases much faster than the direct transmission channel related to each hole. However beyond 250nm, the situation changes: holes scatter more efficiently the propagating SP mode into free space on the output surface and the aperture becomes propagative. As a consequence the transmission becomes dominated by the non-resonant

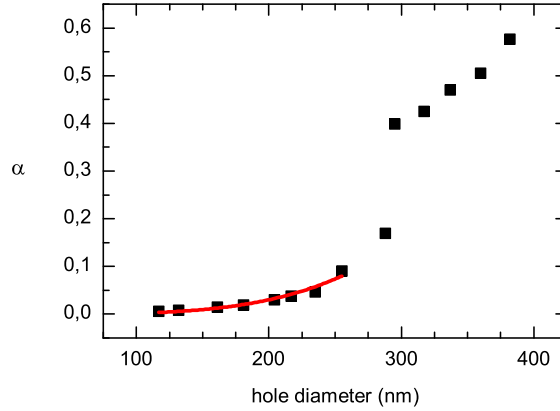


Figure 5.11: Evolution of the global prefactor α associated to the (non-resonant) transmittance through each hole. Fitting results given from Eq.(5.3) are plotted as black squares. The red line displays a simple (d/λ_{res}^4) dependence.

contribution. It thus turns out that the best SP excitation condition is achieved at the transition, although the highest transmission efficiency can still occur for larger holes (see Fig. 5.8). We compared our results with a recent study by Baudrion *et al.* [115] which concentrated on the SP excitation efficiency of single holes through leakage microscopy. Although the experimental setup is different (hole array vs individual holes), a common trend between this experiment and their work appears with their optimal condition found for holes sizes in the range of 200 – 250nm (experimental) and around 300nm (theoretical).

Finally, the fitting results for the global prefactor α are plotted in Fig. 5.11. This prefactor reflects the transmittance of the isolated hole. Bethe originally suggested that upon normal illumination, subwavelength holes in infinitely thin PEC films can be described by an in-plane magnetic dipole. Although this model has been extended to holes of finite depth [104, 116–118], we actually approach the idealized picture of Bethe for the smallest holes ($d = 100 - 250\text{nm}$) as the hole depth (190nm) is much smaller than the resonance wavelength ($\lambda_{res} \sim 800\text{nm}$). In addition it should be noted that at λ_{res} (800nm), the PEC approximation provides a valid description of the properties of Au. This can explain why the evolution of our global prefactor follows a $(d/\lambda_{res})^4$ scaling associated with Bethe’s dipolar model as can be seen in Fig. 5.11. This scaling fails for larger holes and this discrepancy is an additional signature of the differences in the transmission process between small and

large holes, the qualitative change being again located around a diameter of 250nm. In a recent study, Nikitin *et al.* [109] have addressed this problem theoretically in the context of isolated holes milled in a perfect metal films of various thickness. The optical properties of very small holes milled through thin films are essentially dictated by a large induced dipole moment. For larger holes however, multipole moments must be accounted for. As these latter terms are associated with higher waveguide modes, it is not surprising to see an abrupt increase in the global prefactor α at the cutoff transition.

The cutoff issue has been addressed in various theoretical studies [66–68, 110, 119], which already predicted that the interaction of the electromagnetic field with the metal enables the propagation of much longer wavelengths inside a metal waveguide than what can be expected in the PEC approximation. Our results are in good agreement with those studies. It should be noted that such a transition does not only have repercussions on the transmission process, but also strongly modifies non-linear effects, such as increasing second harmonic generation (SHG) [120]. In the Nieuwstadt *et al.* study, a boost in SHG generation is observed for specific widths of rectangular holes which was interpreted in terms of the existence of a non-propagative mode in the holes near the cutoff that had been predicted [66, 68]. While we find that the optimal excitation of SPs occur at the cutoff, we have not found any sharp signature of such mode in our data as such a mode only weakly modifies the linear transmission [120]. It is worth noting that working at a wavelength of 800nm, Nieuwstadt *et al.* also report evidence for the cutoff transition for hole widths around 250nm, in good agreement with our results.

5.4 Conclusion

In this study, we have shown that the transmission through subwavelength hole arrays undergoes important variations in several inherent parameters when the diameter of the holes is increased across the cutoff limit. In particular, we were able to precisely determine the underlying physics that govern this transition by describing the transmission as a combination of a resonant and a non-resonant contribution. It also confirms earlier studies that in a real metal the cutoff occurs at much longer wavelengths than in the PEC approximation. It is worth noting that such a transition appears to be linked to the optimal SP excitation condition on the hole array

which is important for such applications as sensing, molecules and surface plasmons coupling and non-linear effects. Tailoring a hole array for a specific application is however not just limited to defining the optimal diameter and depth of the holes, other parameters must also be considered such as hole geometry, array geometry and material properties. We believe our results will contribute to the understanding of the underlying physics of hole arrays and be useful for future developments.

Chapter 6

Diffraction of single apertures in a real metal

As already discussed in Chapter 1 and 3, diffraction of light through small apertures is one of the most fundamental processes in optics. Understanding this phenomenon in the context of subwavelength holes is of particular interest for many applications in modern nano-optics. The model that is generally used to describe the diffraction of holes much smaller than the wavelength was first proposed by Bethe [62] and associates the aperture to a magnetic dipole as explained in Chapter 3. This model based on the PEC approximation clearly underestimates the role of a real metal in the process. Therefore it is perhaps not surprising that experimental results involving apertures at metal-coated fiber tips [70, 71] (see Fig. 6.1(a) and (b)) revealed significant deviations from this classical model. Differences to Bethe's diffraction model were also observed by Degiron *et al.* [56] (see Fig. 6.1) and Pryzbilla *et al.* [72] in their measurements of subwavelength apertures in flat metal films. In addition it has been shown that the emission profile of individual apertures is strongly modified if the metal film on the emission side is structured with periodic grooves [93–95].

In order to verify in detail these results for subwavelength apertures in a real metal and explore possible limits of classical diffraction theory, we built a new experimental setup dedicated to such measurements. The challenge lies in realizing the necessary sensitivity for such small holes while preserving an acceptable angular resolution. Considerable amount of time and effort was required to build a system that meets these requirements. This could only be achieved at the expense of long

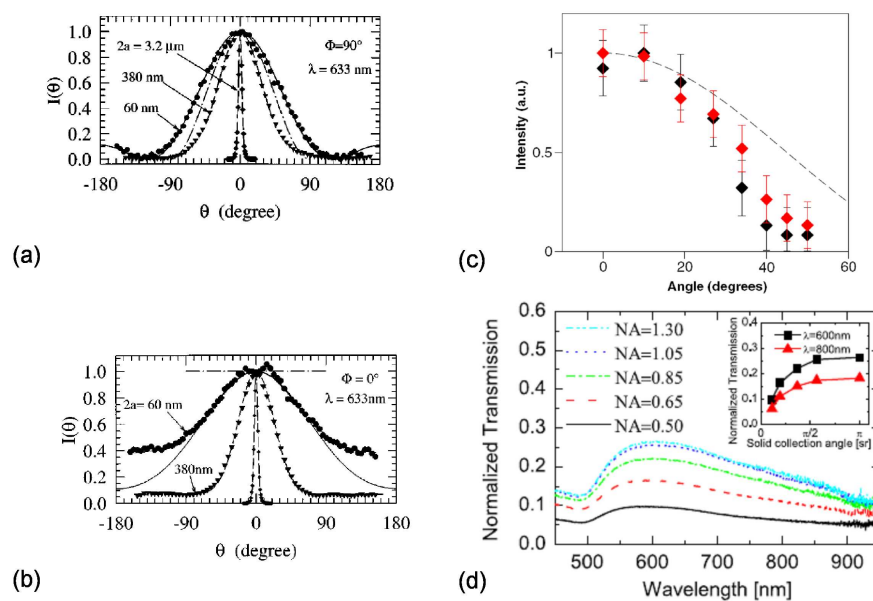


Figure 6.1: Experimental studies of diffraction through subwavelength aperture. (a) and (b): Circular apertures for two different polarization from Obermuller *et al.* [70]. (c): Rectangular aperture for unpolarized light through a rectangular aperture from Degiron *et al.* [56](d): Measurement of transmission spectrum through a single hole in an optically thick Au film for different numerical apertures of the collection objective. The inset shows the intensity evolution for two wavelengths giving an indication of the angular distribution of the diffracted signal from [72]

acquisition times which forced us to automate the whole measurement process.

In this chapter we first present in detail the optical setup and the corresponding control program written in Labview code. As a consequence of the time that was invested to build the system, the planned measurements have not yet been completed. We will therefore only present some of the preliminary results of the diffraction measurements of nanoscale holes. Nevertheless these data already confirms the earlier studies and indicates that the metal response must play an important role in the diffraction process. We expect that the further experimental studies, that are being pursued, will eventually provide a better understanding of the physics involved.

6.1 The experimental setup

Building a good setup dedicated to the measurement of diffraction of subwavelength holes is demanding and different approaches were pursued before settling down on a specific design. In a first step, we checked whether it was possible to refine the system used in [56] and [93] that relied on a microscope connected to a spectrometer (same as described in Chapter 4 for the acquisition of transmission spectra). In this approach, illumination is achieved through a multimode optical fiber and the resolution of the detection can be adjusted by placing different pinholes between the aperture and the collecting microscope objective. The high signal-to-noise ratio of this setup comes at the expense of a low angular resolution (3° in [93], 12° in [56]). In addition the system does not give access to high angles because of steric hindrance.

Due to these problems, we proceeded to build a dedicated optical setup. At first, a standard HeNe Laser was used as the light source and a photodetector connected to an optical power meter was mounted on a rotating rail. This approach failed to provide the necessary sensitivity to adequately measure the diffracted signal as the noise threshold of the photodetector was too high. Next we tried to collect the signal with the end of an optical fiber connected to a CCD camera. Although this approach provided sufficient sensitivity, the measurement was very noisy due to speckle formation. In a further attempt, we followed the same approach as Obermuller and Karrai *et al.* [70, 71], mounting a photodiode on the rotating rail and using a lockin detection system. Although this provided a good resolution (ca. 0.5° depending on the distance of the detector to the aperture), the electric noise induced by the detection system masked the diffraction signal of small holes.

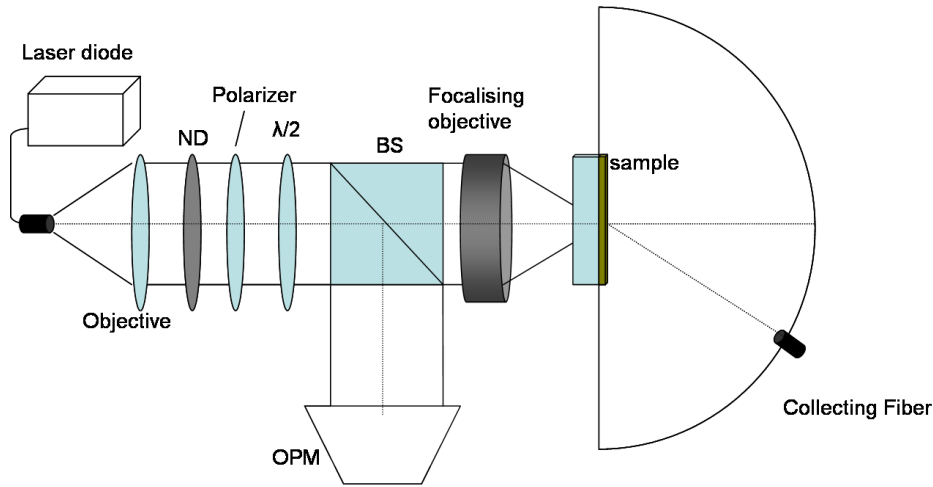


Figure 6.2: Sketch of the experimental setup.

6.1.1 The optics

After such preliminary tries, we finally managed to come up with a system that fulfilled the necessary requirements. This setup is illustrated in Fig. 6.2. As light source a Hitachi HL6501MG fiber pigtailed laser diode emitting at 660nm was fixed to a temperature-controlled Thorlabs TCLDM9 mount which reduces intensity fluctuations during operation. The light-emitting end of the fiber is placed in the focal plane of a Melles Griot objective of focal length 4mm (LSL series) to obtain a collimated light beam. A motorized rotating wheel NSR1 from Newport with different neutral density (ND) filters is placed in the optical path to modify the illumination intensity so that the detector is never saturated. The polarization state of the incident light is controlled with a polarizer (Thorlabs LPVIS) and a zero-order $\lambda/2$ plate.

A 50/50 intensity beam-splitter is introduced into the optical path to redirect part of the incident beam to an Newport 818-SL photodetector connected to a Newport 1830-C Controller. The continuous measurement of the optical power (OPM) is used to normalize the experimental data with respect to any intensity fluctuations.

A microscope objective focuses the incident beam on the diffracting aperture to avoid illuminating a large area of the surrounding metal film. Even though optical thick films (over 10 times the skin depth) transmit very little light, a large

illumination area can lead to a significant background signal when comparing to the light transmitted of the brighter but much smaller hole. The sample with the single apertures is mounted on a micro-positioning stage at the focal plane of the objective.

The signal is detected by an optical fiber fixed on the rotating rail controlled by a Thorlabs CR1-Z7 motorized rotation stage, driven by a Thorlabs T-Cube DC motor unit. This device moves the rail with a minimal step of 0.014° and together with the optical fiber provides a resolution as low as 0.1° without difficulty. The optical fiber is connected to an Avantes Avaspec 2048-TEC spectrometer with Peltier cooling for noise reduction. The advantage of the spectrometer lies in the fact that it is possible to acquire the data over an extended period of time, increasing the sensitivity. At the same time, only the intensity at the wavelength of the illuminating laser diode is considered, minimizing the contribution from stray light, further improving the signal to noise ratio.

6.1.2 Automatizing the acquisition process

In order to clarify the complete experimental procedure, we will describe in detail the different tasks that need to be accomplished during such a measurement. Those tasks are fulfilled by a Labview program that had to be written specifically for this use. This was required considering the duration of a complete measurement. Indeed a typical recording time for each spectrum is 60s. If necessary, several acquisition are undertaken and averaged to further reduce the noise leading to a an acquisition time of 5 to 10 minutes for each angle. Consequently, using a step of 0.5° inside the limits of -30° and 60° , the complete diffraction measurement can take several hours or even a day.

Before the acquisition program could be written, subroutines were needed to communicate with the different motors (rotation axis, ND filter wheel) and detectors (Newport 1830C, Avantes spectrometer). While for the rotation motor the code had to be written from scratch, Labview control programs were provided for the other devices. Nevertheless, these programs too needed specific modifications to fulfill the required tasks. We will avoid going into too much technical detail about these subroutines which are detailed in Appendix C.

The mainframe of the central control program is illustrated in Fig. 6.3. In a first

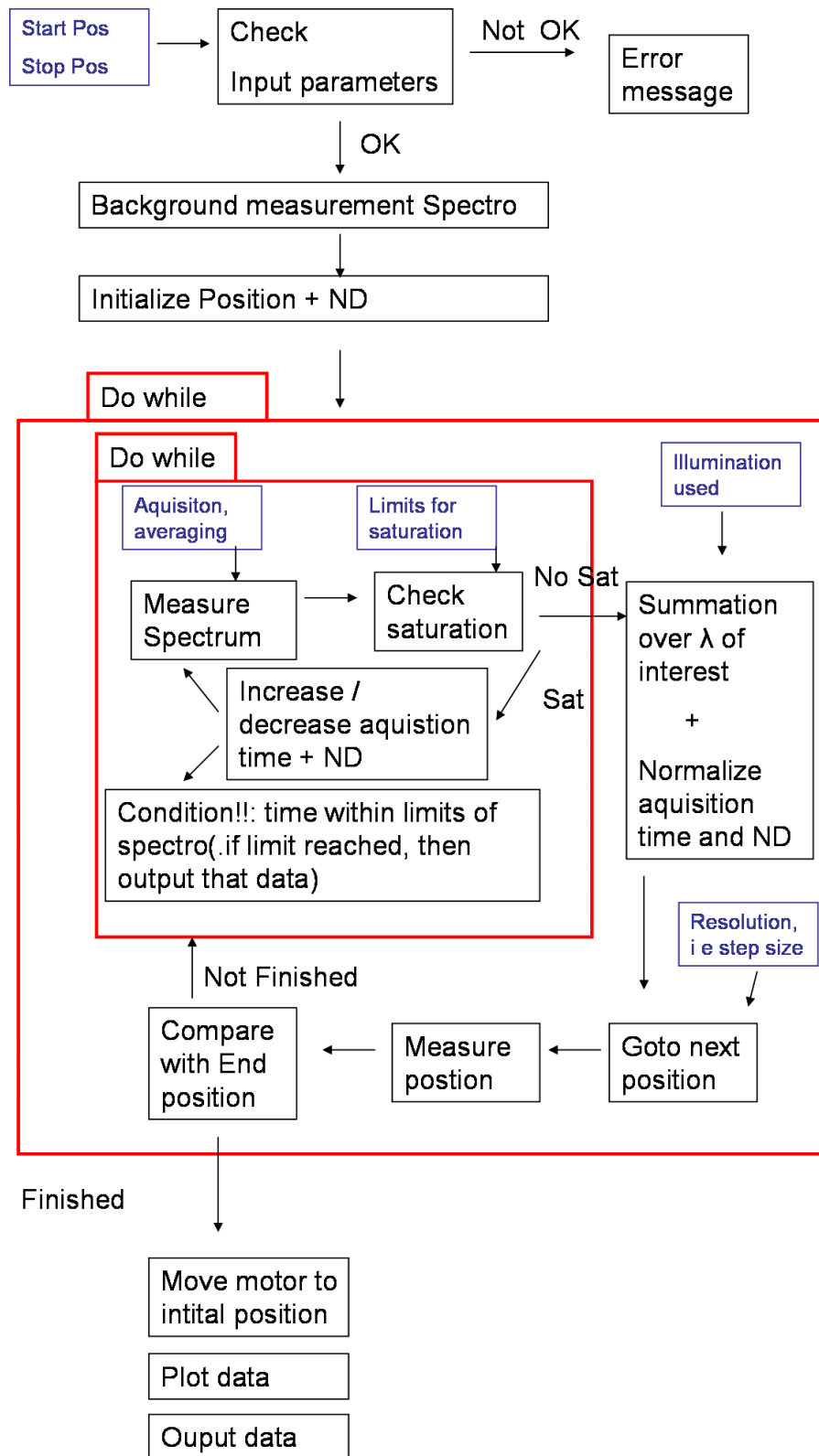


Figure 6.3: Sketch of the different experimental steps accomplished by the measuring program. The blue text boxes correspond to the information input provided by the user.

step the input parameters (Start position and Stop position) are checked in order to make sure that they are all set in the appropriate angular ranges. Then the program proceeds to background measurements (dark) of the spectrometer which are later subtracted for each acquired spectrum. The system then moves the detector into starting position corresponding to the first measured angle. After acquiring the spectrum and subtracting the dark noise, the program verifies that the intensities are within an acceptable range. If the signal is too low, the measurement is repeated with a higher acquisition time or a weaker neutral density in the illumination path. If the measured intensities are too high and the detector saturates, the adjustments are reversed. These steps are repeated until a valuable data point is collected or the limits of the setup are reached (lowest density, i.e. no density and longest acquisition time or highest density and shortest acquisition time). In the latter case, the system informs the user that the result might not be meaningful. For instance, if the signal is too low, one possibility is to further increase the precision by proceeding to multiple acquisitions and averaging them.

If an acceptable spectrum is recorded, it is summed up over the wavelengths that compose the emission line of the laser diode and normalized with respect to acquisition time and the intensity fluctuations of the source. Then the same steps are repeated for all the different angular positions of the detector. Finally the system plots the diffraction pattern and saves them for further processing.

6.1.3 Validation of the equipment

In order to verify our experimental setup, a single macroscopic slit of length $150\mu\text{m}$ and of width $15\mu\text{m}$ was fabricated in a 300nm thick Ag film using FIB milling. Based on the ratio between the wavelength, the aperture size and the distance between the aperture and the detector (25cm), the Fresnel number is very low and the Fraunhofer formula for far-field diffraction should be valid [14, 60]. The measured diffraction pattern together with a fit using the theoretically predicted formula is shown in Fig. 6.4. It should be noted that for this experiment the focussing objective was unmounted to avoid having an illumination spot smaller than the dimensions of the slit.

It can be seen that the measured diffraction pattern shows very good agreement with the theoretical curve for small angles. However for large angles the observed

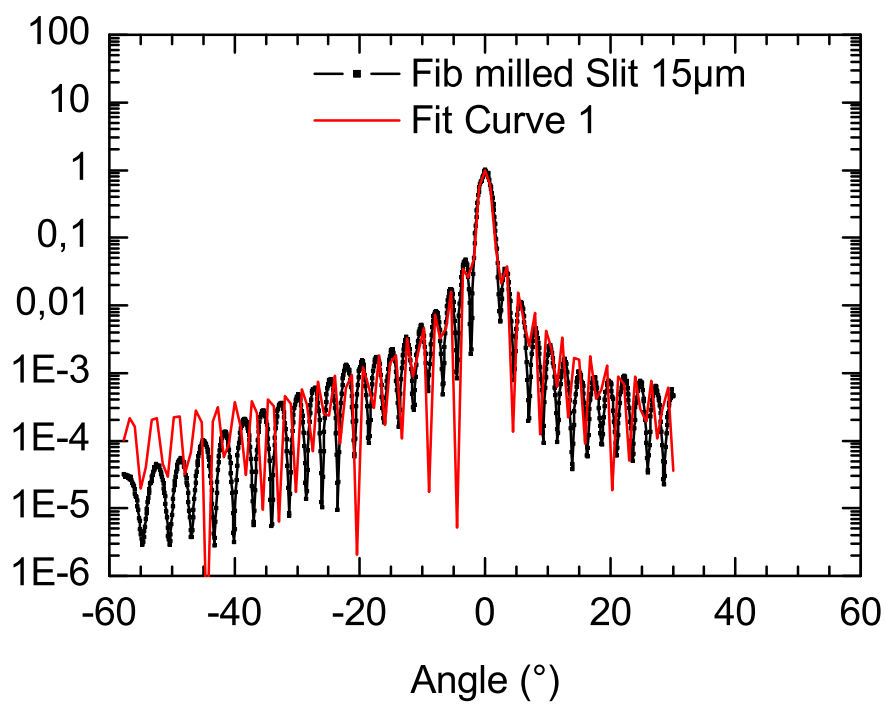


Figure 6.4: Sketch of the different experimental steps accomplished by the measuring program. The blue text boxes correspond to the information input provided by the user.

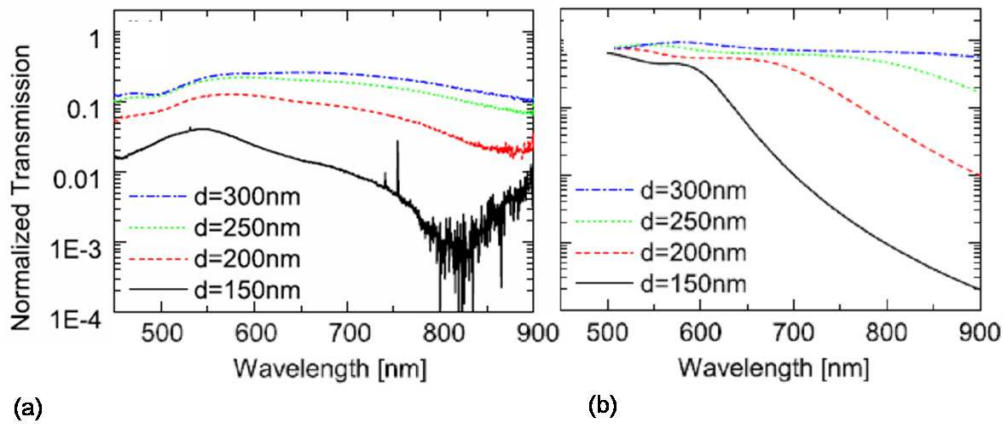


Figure 6.5: (a) Transmission spectra for single holes in a Au film of thickness of 295nm and of increasing hole diameter ($d = 150, 200, 250$ and 300 nm). The film was deposited on a glass substrate and covered with an index matching fluid ($n = 1.53$). For all the structures, the transmitted light as been collected using the same objective (Nikon Plan Fluor 100) with numerical aperture fixed to 1.3. (b) Transmission spectra of a $d = 300$ nm single hole milled in a 295nm thick Au film obtained by increasing the numerical aperture of the collecting objective. . Inset: Measured transmission as a function of the solid angle of collection evaluated at 600nm and 800nm. Each curve is an average of the spectra of 3 isolated holes of the same dimensions. All data are from [72].

deviation is expected since the theoretical formula is only valid within the Fresnel approximation, i.e. for small angles. This measurement not only confirms the high resolution of our setup, but also underlines the high dynamic range of the setup. The fit gives a slit width of $16\mu\text{m}$, which is in good agreement with the measured value.

6.2 Towards the study of single subwavelength apertures

6.2.1 Spectral characterization

Having checked the apparatus for macroscopic apertures, we proceeded to characterize the diffraction of subwavelength holes. As these measurements are accomplished at a fixed wavelength, the analysis of these patterns requires a precise understand-

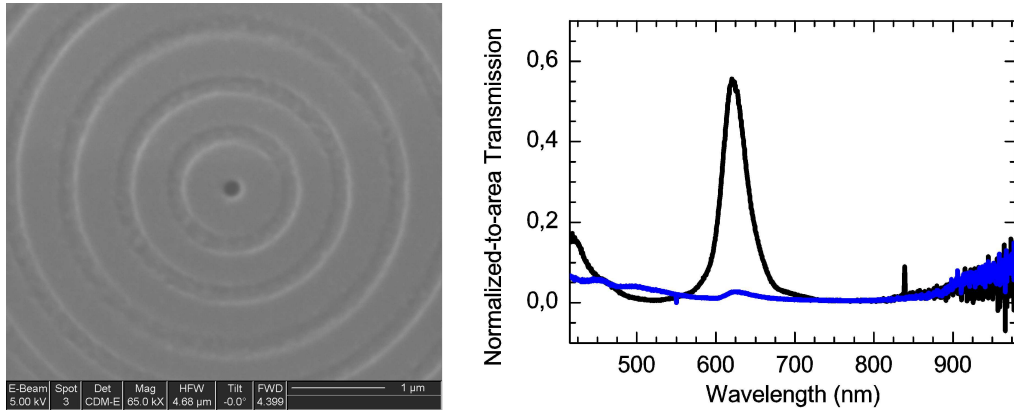


Figure 6.6: SEM image of a single hole surrounded by concentric circular grooves (Period $P = 570\text{nm}$, film thickness $h = 300\text{nm}$, surrounded by 10 grooves of width $P/3$ and depth $gd = 80\text{nm}$) together with the corresponding transmission spectrum. The black curve corresponds to the transmission spectrum when illuminated on the textured side and the blue curve corresponds to illumination through the glass side.

ing of the spectral properties of such single apertures. For this reason we will first review some results on single apertures from recent works.

In a study by Degiron *et al.* [56], it was shown that the transmission of single apertures in free-standing Ag films shows signatures of localized modes. These non-dispersive modes are best observed when both interfaces are index-matched. Przyilla *et al.* [72] also measured such transmission spectra for subwavelength holes in the context of holes milled in an Au film (300nm) deposited on a glass substrate and covered with an index-matching liquid. The experimental results of this study are shown in Fig. 6.5 together with the corresponding theoretical results obtained through modal expansion formalism. It can be seen that the transmission spectra are broad and modulated by the cutoff function of the apertures.

The transmission through such single holes can be strongly enhanced by surrounding the aperture with concentric grooves [88–91] as already explained in chapter 3. In order to precisely tune such structures to our wavelength of interest, we fabricated bull's eye structures as the one shown in Fig. 6.6 and optically characterized them. The transmission spectra were recorded for different focal planes to correct for chromatic aberrations using the same approach as explained by Przybilla *et al.* [72]. As can be seen in Fig. 6.6, the transmission through such a structure is strongly enhanced at the resonance wavelength when illuminated on the struc-

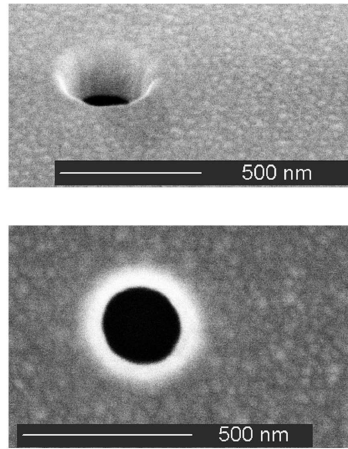


Figure 6.7: SEM images of a single hole of hole diameter 250nm milled in an optically thick Ag film of thickness 300nm.

tured side. However if the film is illuminated through the non-structured surface, the spectrum is mostly flat except for a small peak at the resonance wavelength of the output corrugation [92].

The given transmission intensities should however be considered carefully as only the light contained within the acceptance angle of the collecting microscope is measured. Therefore our measurement probably underestimates the total light transmitted. However the exact quantification of the collected light fraction for a given solid angle (i.e. given numerical aperture) requires precise knowledge of the diffractive properties of such apertures, justifying yet again the need for the diffraction measurements.

6.2.2 First experimental measurements of diffraction

For the diffraction study, isolated holes as the one illustrated on Fig. 6.7 were milled in an optically thick Ag film (thickness $h = 300\text{nm}$). The recorded diffraction pattern of a single hole of radius $r = 150\text{nm}$ at a wavelength of 660nm is shown in Fig. 6.8. A narrow peak is seen at small angles which is related to the transparency of the metal and will be discussed further down. The diffraction pattern is systematically measured for two orthogonal polarizations. To understand how we define the polarization orientations, it should be noted that the detector always scans the

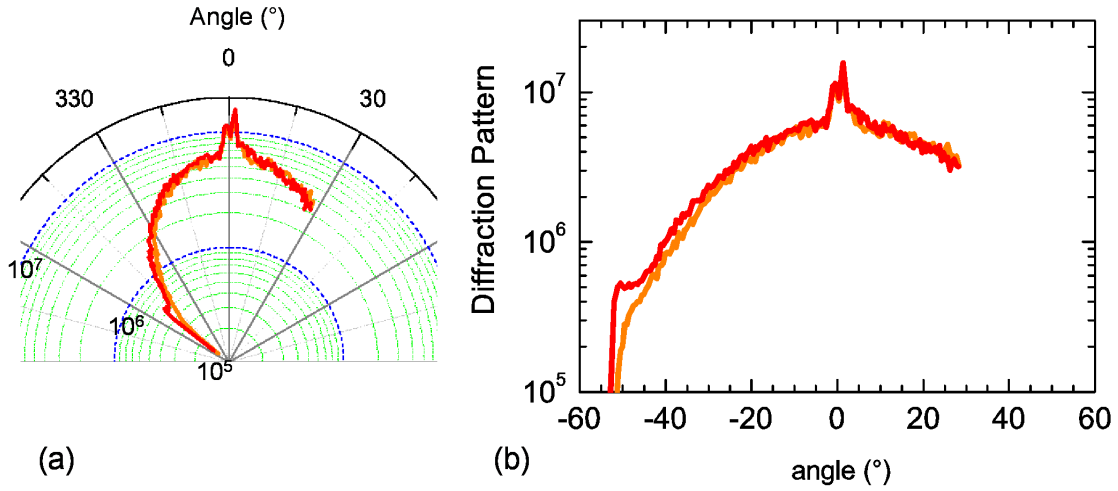


Figure 6.8: Diffraction pattern of a single aperture in a 300nm thick Ag film. The hole diameter is 300nm and the diffraction pattern is evaluated at a wavelength of 660nm. The orange curve corresponds to polarization perpendicular to the direction of measurement and the red one to parallel polarization.

emitted signal in a plane parallel to the optical table. Considering this, we define parallel or perpendicular polarization with respect to this detection plane. From the measurement in Fig. 6.8, it seems there is no difference between both polarizations. To understand the measured signal we compared the results with classical models describing holes in the small aperture ($r \ll \lambda$: Bethe [62]) and the large aperture ($r \gg \lambda$: Fraunhofer [13, 14, 60]) limit. In the subwavelength limit, the hole is usually associated with a magnetic dipole. In such a case, the corresponding diffraction pattern is independent of the hole size (approximation $r \ll \lambda$) and expected to follow a $\cos^2(\theta)$ dependence for perpendicular polarization and to be isotropic in the other direction, as already discussed in Chapter 3. We compared the measured angular dispersion with the Bethe formula and it can be clearly seen in Fig. 6.9 that the real diffraction does not follow this prediction. To check whether the model for larger holes is more adequate, we compared the experimental results also with the Fraunhofer far-field formula which provides an accurate description for holes much larger than the wavelength in the range of low Fresnel numbers and which is given by :

$$I(\theta) = I_0 \left[\frac{2J_1(kr \sin\theta)}{kr \sin\theta} \right]^2 \quad (6.1)$$

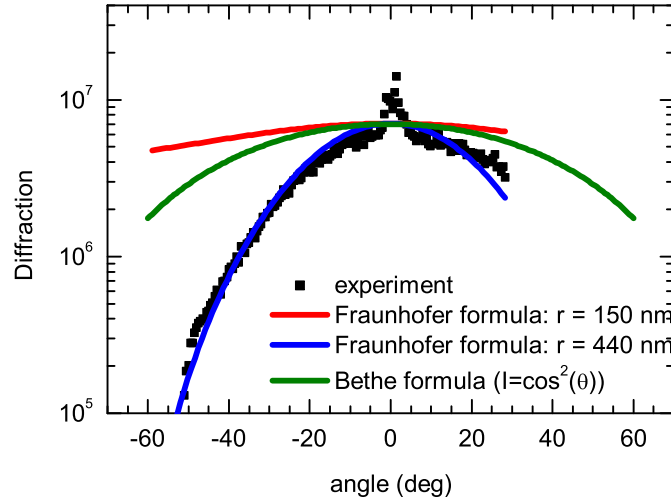


Figure 6.9: Experimental diffraction as already shown in Fig. 6.8 together with different theoretical solutions. Red curve : Fraunhofer far-field diffraction formula expected for a hole of radius 150nm. Blue curve: fit using the Fraunhofer formula giving a hole size of radius 440nm. Green curve: Bethe solution giving a dependance in $\cos^2(\theta)$.

where $k = 2\pi/\lambda$ is the wavevector of the illuminating light and J_1 the first order Bessel function. As can be seen in Fig. 6.9, this model also fails to describe the observed signal. By fitting eq. (6.1) to the data, a hole with a radius of 440nm is extrapolated, confirming that neither the Bethe nor the Fraunhofer formula provides an accurate description of the diffraction properties of such a single hole.

Using the same setup, we also measured the signal diffracted through a propagating hole which on the exit side is surrounded by concentric grooves. The recorded diffraction patterns for such a bull's eye with a central hole radius of 300nm is shown in Fig. 6.10 together with measurements for the isolated hole of the same size. As can be seen the grating only modifies the diffraction for angles below 10° where beaming becomes apparent in agreement with earlier observations [93–95]. In addition we observe that these beaming properties depend on the polarization of the incident light leading to minima at angles around 5° for parallel polarization. It is not yet clear how the size of the hole relative to the wavelength influence such results.

These first measurements already raise many questions about the diffraction through subwavelength holes in a real metal. For instance in the diffraction patterns

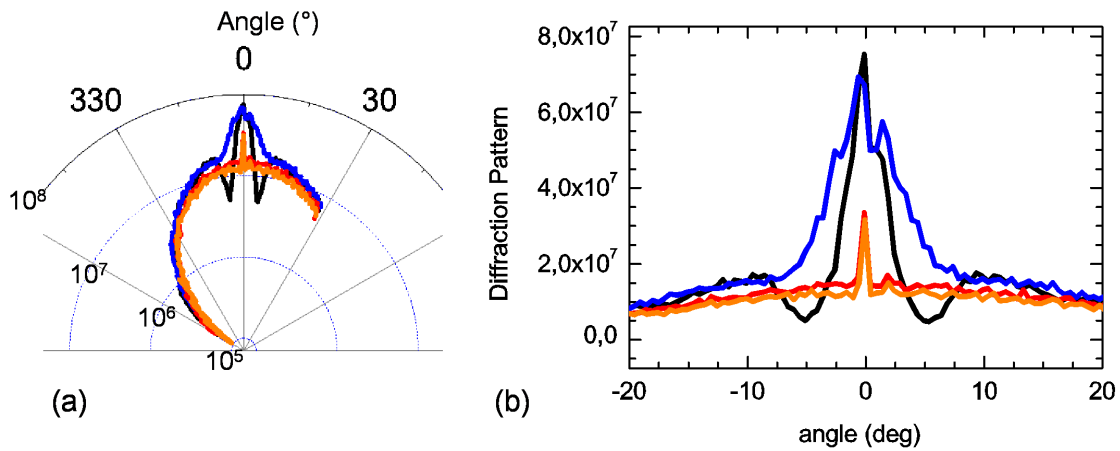


Figure 6.10: Diffraction pattern of a single aperture of radius 300nm in a 300nm thick Ag film surrounded on the exit side with circular concentric grooves (10 grooves, period $P = 570\text{nm}$, width $P/3$, depth $gd = 80\text{nm}$) for two polarizations (blue: perpendicular polarization, black parallel polarization) and without corrugation (orange: perpendicular polarization, red: parallel polarization).

in Fig. 6.8 and for the single hole in Fig. 6.10 a peak appears around 0° . This was visible for all the different measurements on small holes and it is related, as already discussed, to the residual transparency of the metal. The illuminated area being much larger than the hole (factor of ca. 100), a small amount of leakage through the optically thick metal film will be significant when compared to the small hole. A simple subtraction of the metal transparency shows that it cannot account for the experimental deviations from the classical models shown in Fig. 6.9.

However there are a number of parameters that might influence the diffraction of such small apertures. Bethe's analysis already assumes a single dipole when $r \ll \lambda$ which would result in a specific diffraction pattern as already discussed. There must other modes present in our experimental conditions specially since $r < \lambda$. As indicated by a number of theoretical studies [65–69, 109, 110], localized modes play an important role in the transmission characteristics of individual holes. Furthermore localized SP modes at the rims of the holes are also present [56]. Together these modes will no doubt modify the diffraction pattern and its polarization dependence. It has been shown that the state of polarization can be used to couple to specific aperture modes [121]. Therefore it will be important to measure the diffraction as a function of wavelength and the state of polarization of the incident beam. An-

other factor that probably effects our measurements is the choice of the illumination objective. Indeed in our setup the illumination has a specific angular distribution defined by the numerical aperture of the setup. It remains to be explored how much a diffracted light beam is influenced by the angular distribution of incident beam. Needless to say that the role of the shape, depth and size of the aperture, probably together with the dielectric properties of the real metal, must also be evaluated.

With the present equipment it is possible to launch a a systematic study of the diffraction as a function of the parameters just discussed. The automation of the measurement, the high signal to noise ratio together with high dynamic range ensures that this can be achieved. Not only single holes but also decorated holes, such as bull's eye structure will be the subject of detailed studies in the future.

Chapter 7

Plasmonic photon sorters for spectral and polarimetric imaging

Color cameras mimic the human eye and record only a small part of the information contained in the incoming light. Modern image sensing techniques which subdivide the light spectrally in a wider range or record information about the polarization of the incoming light can extract much more information and have been proven to be useful in applications ranging from biological studies to remote sensing [122–128].

A perfect system would be able to collect on each pixel of a given image not only the intensity of the incoming light but a complete spectrum enabling an intensity mapping at each wavelength. Digital spectral imaging techniques [129] typically rely on systems of filters or interferometers combined with scanning or subsampling to record a spectral image "cube" (see Fig. 7.1).

Here, we address the possibility of using surface plasmon structures to improve spectral and polarimetric imaging. By combining into a lattice different unit structures sensitive to individual colors, we first demonstrate that photon sorting can be achieved without subsampling or scanning. In a second step we study arrays which are also sensitive to the polarization by modifying the unit structure in the lattice. The novel approach presented here show that it is possible to combine spectral and polarimetric imaging in extremely compact and simple devices using plasmonics.

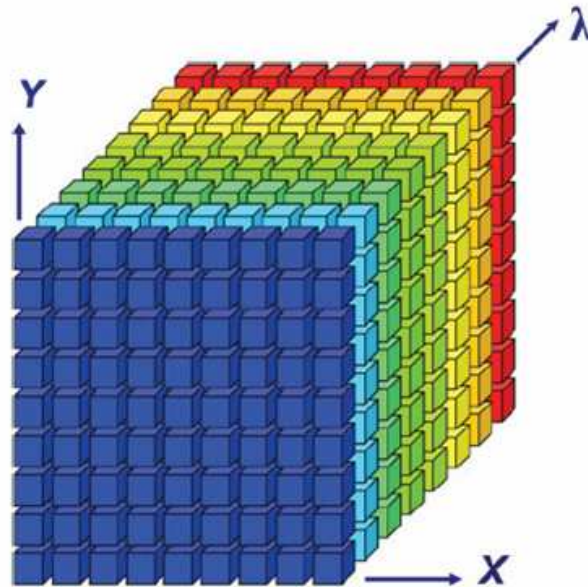


Figure 7.1: Spectral imaging concentrates on the techniques that enables the acquisition of the image cube, which means that for each pixel of the image, the complete spectrum of the light that illuminates this pixel is desired. Image from [127].

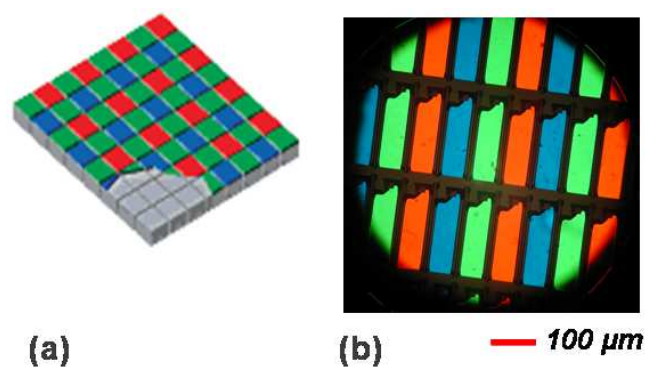


Figure 7.2: (a) The Bayer spectral imaging filter. On each pixel, a different wavelength range or color is collected. from [130] (b) Microscope photograph of the Bayer filter used in the NEC AccuSync LCD71Vm LCD computer screen.

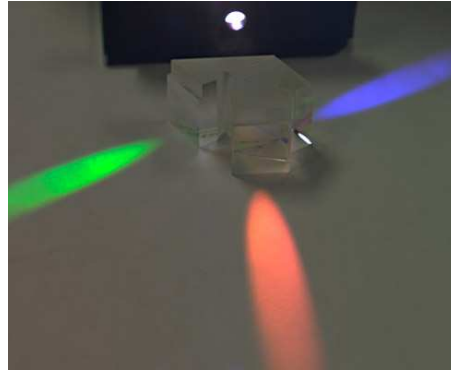


Figure 7.3: Setup consisting of 3 prisms that redirect the light through refraction and reflexion into 3 different directions based on wavelength.

7.1 Spectral imaging using SPs

Depending on the application, there are different techniques that are employed to collect image cubes, each having their own advantages and limitations. The most common one relies on a mosaic of filters, called the Bayer filter, covering the array of photodetector pixels [131], in such a way that each pixel is only sensitive to one color as illustrated in Fig. 7.2. This implies that for this classical approach (see Fig. 7.2a), 1/2 of the pixels collect green light whereas 1/4 are sensitive to the red or the blue light. This puts a simple geometrical limit to the maximum collection efficiencies for each color. To quantify the overall efficiency, we unmounted a Bayer filter shown in Fig. 7.2b of a commercially available flat screen and measured the corresponding absolute transmissions and found it to be in the range of 20 to 30% for visible wavelengths. This is related to the specific geometry of Bayer approach as for each individual filter efficiencies in the range of 80 to 90% could be measured. Another limitation of this approach is the issue of registration, due to the lateral displacement of the array of pixels corresponding to each color. In other words, each color is recorded for a different fraction or part of the image. This thus imposes a limit on the resolution which is not defined by the size of an individual pixel, but by a superpixel sensitive to all the colors. To mitigate these limitations in the real devices, the actual image is generated by analysis of the different pixels signals using data processing algorithms. Although this is by far not perfect, it is still largely sufficient for such applications as low-cost digital cameras or mobile phones.

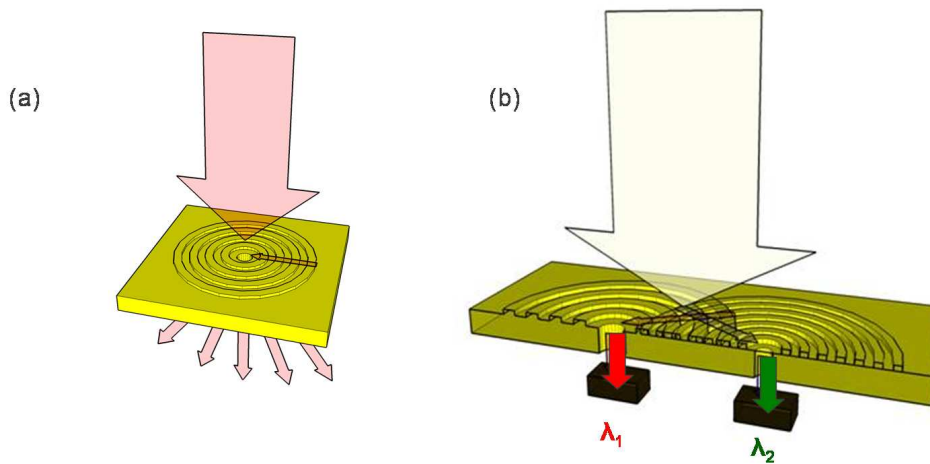


Figure 7.4: Spectral filtering by plasmonic structures. (a) A single bull's eye acts as a plasmonic filter increasing the light transmission through the central hole for the resonances wavelength defined by the grating. (b) Two overlapping bull's eye structures, where each structure is sensitive to a different wavelength (red or green), collects it and redirects it to different photodetectors based on the wavelength.

More sophisticated cameras and spectral imaging devices typically rely on integrating several CCDs. Using proper alignment of dispersive elements as illustrated on Fig. 7.3, it is possible to redirect an incoming white light beam into different directions according to wavelength which are then collected by the CCDs. On the downside it should be noted that such a system is clearly less robust and much more cumbersome than a Bayer filter. Nevertheless such systems have recently been put to use in high-end hand-held cameras. Similar setups are also used in hyperspectral imaging, where the number of bands is often increased above 3, notably into the infrared (IR) for military and agricultural purposes [126].

A novel approach that has been proposed by the company Foveon involves stacked photodetectors. At a given spatial location, each color is recorded according to its penetration into the photodetector stack [132]. The shorter wavelengths are collected close to surface and the longer wavelengths deeper inside the semiconductor layer. With this method, it is possible to increase the resolution and limit registration issues as compared to the Bayer filter.

Generally speaking, it should be noted that there exist a lot of different approaches to achieve spectral imaging and have been proven useful in a variety of domains. Nevertheless each one has its flaws and there is always interest for new

devices that might be more adequate for specific applications.

7.1.1 Concept of plasmonic photon sorting

The basic unit that we will use in our approach consists of a bull's eye structure, namely a single aperture surrounded by a periodic grooves. By coupling the light to SPs through the grating, it is possible to generate intense electromagnetic fields at the central hole. The flux per unit area through the aperture can thus be larger than that of the incident light, confirming that the grooves act as an antenna as already discussed in Chapter 6 [89,90]. The EOT phenomenon is important here as it allows for useful light collection efficiencies even though the apertures represent only a small fraction of the surface of the structure.

The class of devices that we propose consists of overlapping such light collection structures as illustrated in Fig. 7.4. The key concept is that each structure would collect light over a certain frequency range and be able to redirect it to its central aperture even from the region where it overlaps with other collectors. With photodetectors placed underneath the apertures, we would then obtain a miniature "spectrometer" capable of recording the spectral information of the light incident on the overlap area. An array of such collectors could be placed in the focal plane of an imaging lens, resulting in a compact spectral imaging system. The specific advantage of our approach as compared to the Bayer filter is that the registration and resolution limits are reduced by the collection of different wavelength from one location.

7.1.2 First tests on bi-eye and tri-eye structures : the need for groove depth gradient

In order to check the feasibility of such an approach to photon-sorting, we fabricated by FIB-milling on Ag substrates bi-eye structures, composed of two overlapping bull's eye structures as well as tri-eye structures composed of three bull's eyes. It should be noted that the depth of the grating was adjusted to be constant over the whole grating. In other words, at a point where two grooves overlap the depth is the same as if only one groove was present. In a similar way, the area between the hole and the first groove is milled at the same depth as the grooves in such a way that each hole has the same structure in its immediate surroundings. This essentially

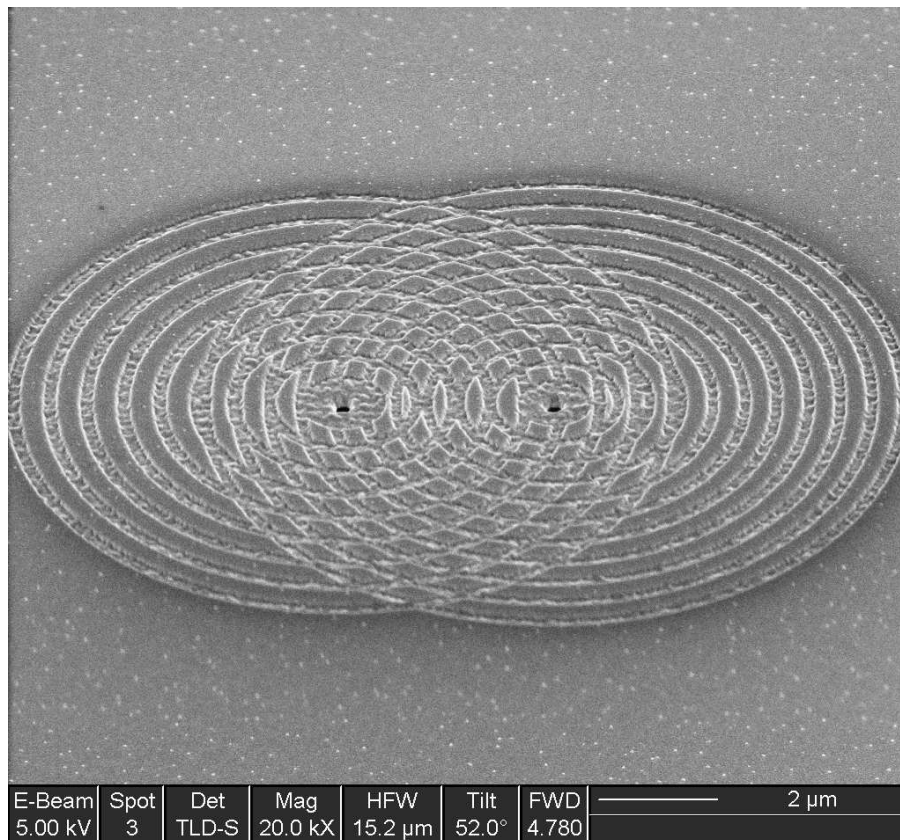


Figure 7.5: SEM image of a double bull's eye (bi-eye) structure fabricated by FIB milling in a 300nm thick Ag film. The left one has a period of 700nm the right one of 600nm. The depth of the grooves is 100nm and the width $P/3$, while the central hole has a diameter of 250nm. The distance between both hole corresponds to $4\mu\text{m}$.

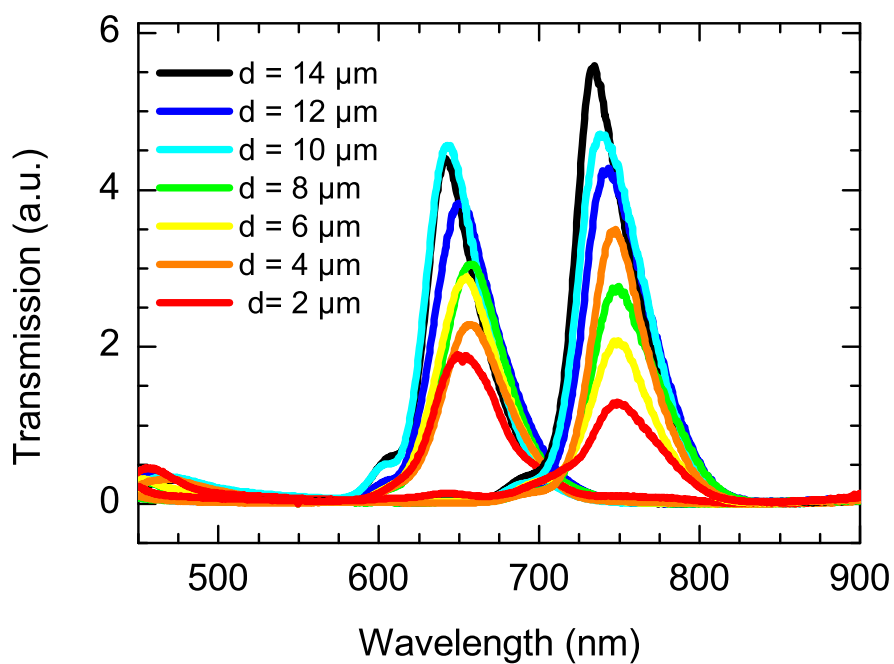


Figure 7.6: Transmission spectra of the two holes of a bi-eye structure for different hole-to-hole distances d (and consequently different overlap). The other structural parameters are the same as those on Fig. 7.5. The period is different for each bull's eye and given by P

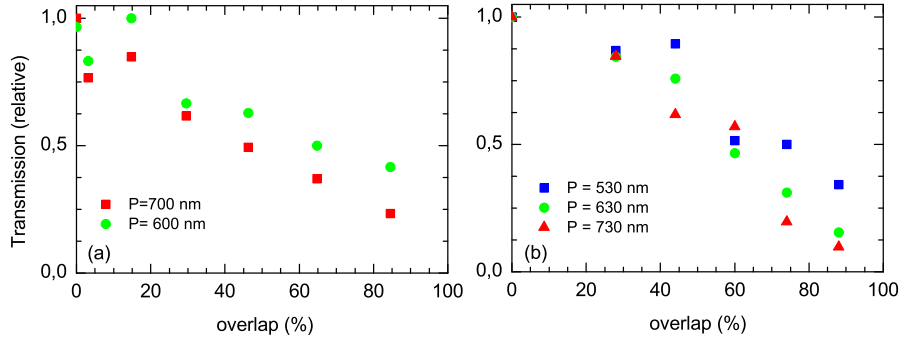


Figure 7.7: Relative transmission peak intensity for bieve (a) and trieye (b) structures as a function of overlap. The overlap is defined as the area percentage of one bull’s eye that is covered by a grating of different periodicity. The transmission is normalized to the transmission intensity that is obtained for an isolated bull’s eye. The period is different for each bull’s eye and given by P .

ensures that the transmission of each hole is determined by SPs and not perturbed by local scattering effects at the level of each individual hole. The choice of Ag as plasmonic material was motivated by the high transmissions that can be obtained in the full range of the visible spectrum [99, 100].

Such a spectral filtering structure is visible on Fig. 7.5 involving two overlapping bull’s eyes. The corresponding transmission spectra were measured for each hole in the same way as for a normal single bull’s eye and are shown on Fig. 7.6. It can be seen that the peak position undergoes only slight variations as a function of overlap. At the same time each bull’s eye does not transmit any significant amount of light corresponding to the other periodicity.

However the transmission peak intensity goes down as the overlap is increased as can be seen in Fig. 7.6 and 7.7 for both bi-eye and tri-eye structures, showing clearly the limitation of these kind of structures for spectral imaging as one would like to preserve signal strength at higher overlaps.

7.1.3 Single and multiple bull’s eye structures with groove depth gradient

The most likely reason for the decrease in the transmission at high overlap being the perturbation introduced by the grooves of one bull’s eye near the hole of the other, we decided to introduce a groove depth gradient. We designed the structure

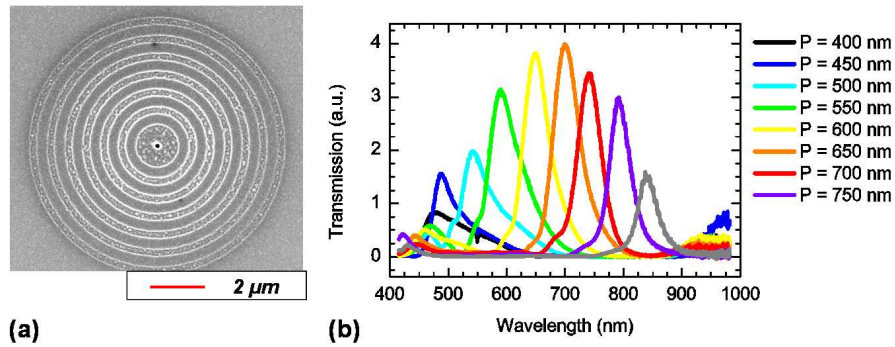


Figure 7.8: Single bull's eye with a groove depth gradient. (a) Single bull's eye structure milled by FIB in a 300nm thick Ag film on glass substrate. Dimensions: Central hole diameter $d = 170\text{nm}$, with 6 circular grooves (width 150nm, period 800, depths varying linearly from 150nm (central ring) to 10nm (outer ring)). (b) Transmission spectrum for bull's eye structures with the same dimensions as in (a) for groove periods varying from 400 to 800nm.

in such a way that the groove depth follows a linear variation with the deepest grooves close to the central hole as illustrated in Fig. 7.8 for a single bull's eye. In a first step we fabricated such single bull's eye and changed the periodicity in order to verify that the transmission properties remain comparable to what can be obtained for regular bull's eyes.

Their transmission spectra show a peak at wavelengths slightly larger than the period, similar to what is obtained without a gradient. However the peaks are broader and the intensity is reduced by roughly 25% compared to the normal bull's-eye (compare largest distance bi-eye structure in Fig. 7.7 and Fig. 7.8).

In a second step, we fabricated tri-eye structures with groove gradients as shown in Fig. 7.9. The corresponding transmission spectra for different overlaps were measured and are shown on Fig. 7.10. The transmission peak intensities at the 3 resonances hardly change up to overlaps of 60% before decreasing. This significant improvement confirms that the introduction of shallower grooves reduces the scattering perturbation of one structure on the other. This result shows that properly designed overlapping plasmonic gratings can simultaneously couple light from a given location and redirect the different wavelengths to specific apertures. Each grating can be individually tuned for given color or resonance. Hence these features fulfill the necessary condition for spectral filtering with improved registration and resolution compared to the standard Bayer filter. The tri-eye structure can be

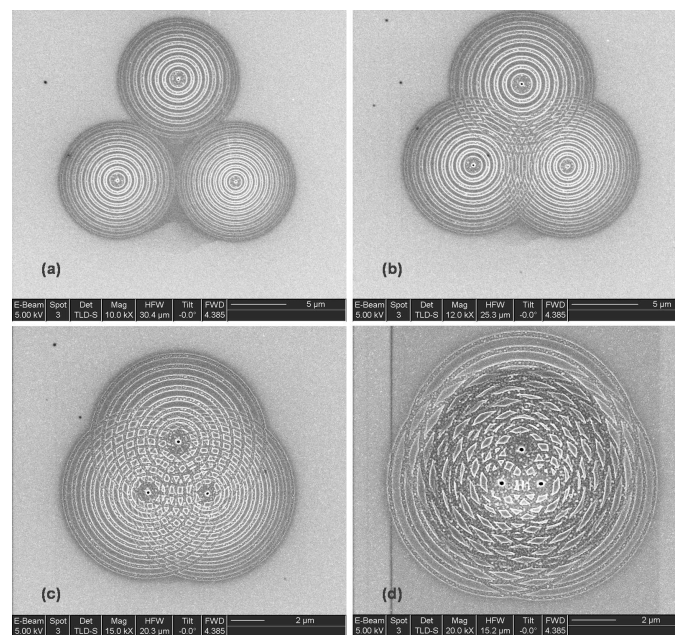


Figure 7.9: Trieye structures, each composed of 3 bull's eye structures of different periods ($P = 530, 630$ and 730nm respectively). The groove depth varies linearly from 100nm (close to hole) to 20nm (far away from hole) and each hole has a size of 170nm . The distance between the holes varies: (a) $14\mu\text{m}$ (isolated) (b) $8\mu\text{m}$ (c) $4\mu\text{m}$ and (d) $2\mu\text{m}$.

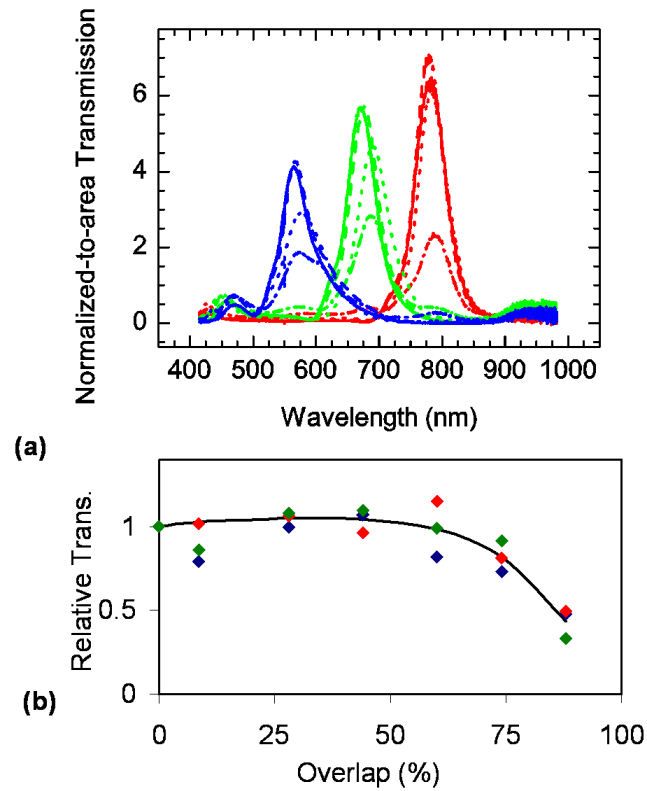


Figure 7.10: (a) Transmission spectra for the tri-eye structures shown in Fig. 7.9 (bold lines: separated bull's eye structures, dashed line: 44% overlap, dashed-dotted: 77%, dotted lines: 88%). The colors correspond to the 3 different periods P of the gratings (blue: $P = 530\text{nm}$, green: $P = 630\text{nm}$, red: $P = 730\text{nm}$). (b) Transmission peak intensities normalized to the isolated bull's eye peaks shown in (a) as a function of overlap.

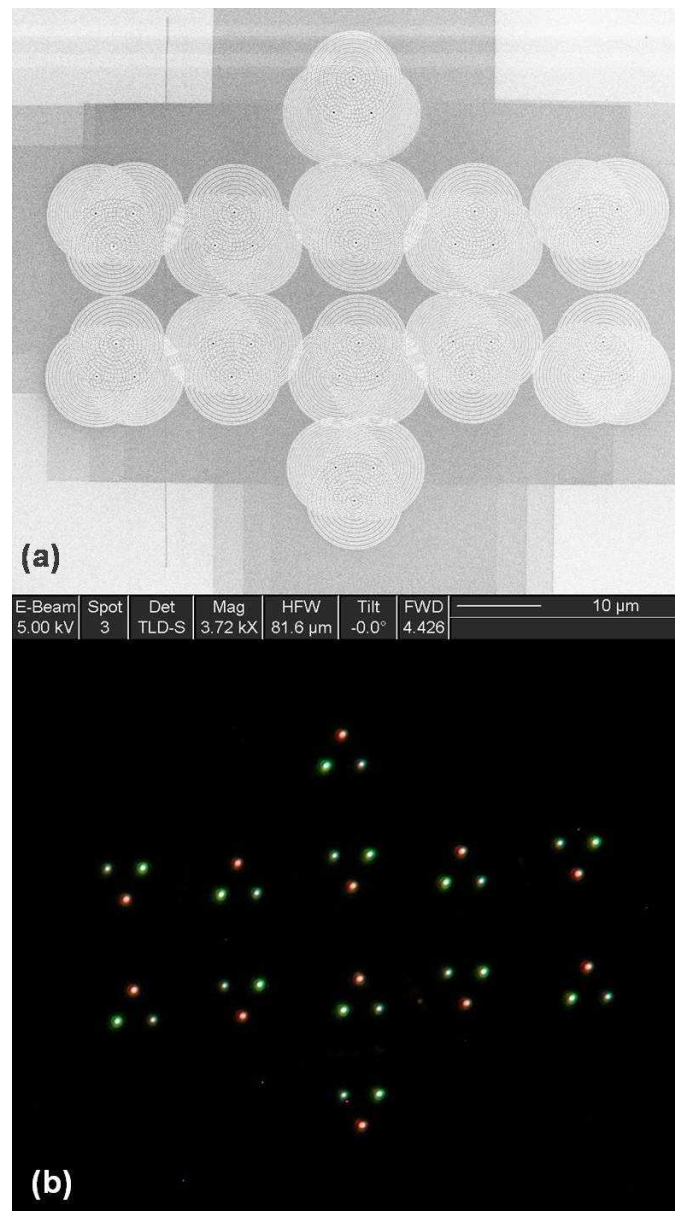


Figure 7.11: Arrays of tri-eyes. (a) SEM image of an array of tri-eye structures fabricated by ion beam milling on an 300nm thick Ag film. (b) Photograph through a microscope of the structure shown in (a) when illuminated with a collimated white light beam.

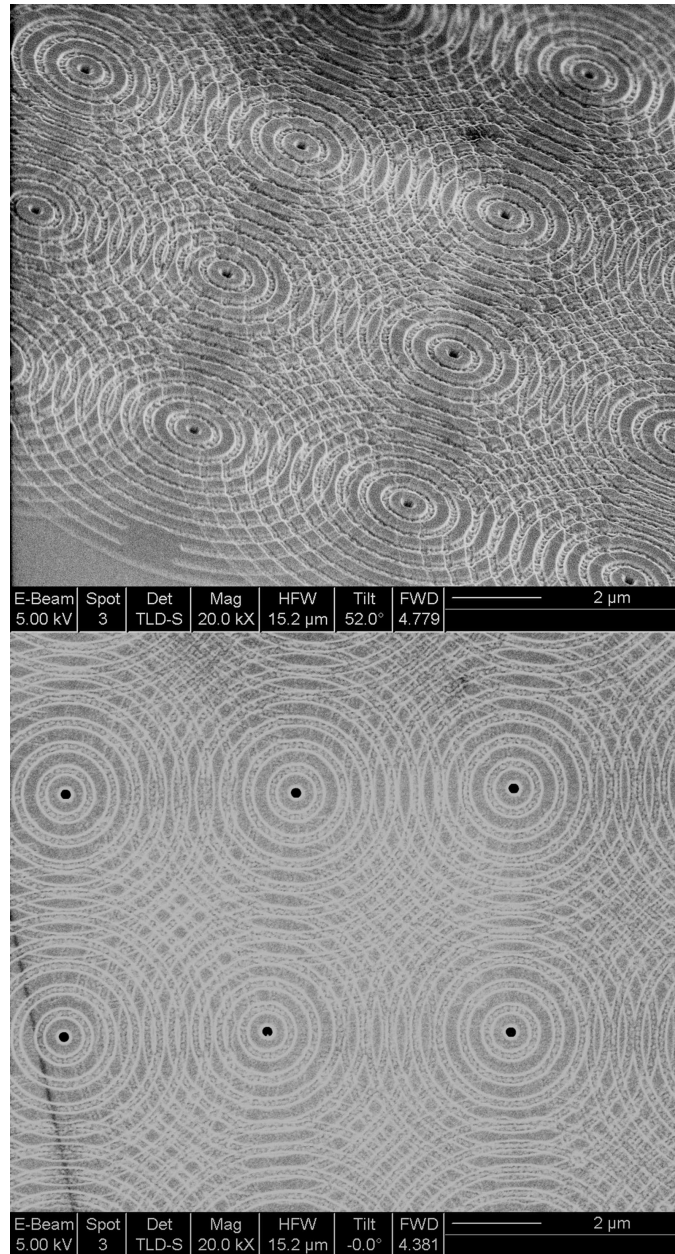


Figure 7.12: Array of bull's eyes. Each bull's eye has a period of 600nm, with 9 grooves of varying depth (100nm close to central hole, 10nm far away). The bull's eyes are placed in a square lattice of length $6\mu\text{m}$. The central holes have a diameter of 170nm.

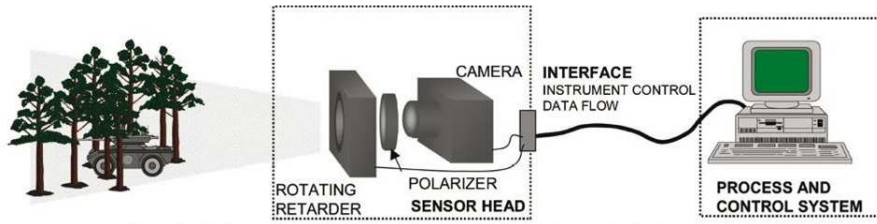


Figure 7.13: Rotating element polarimetric imaging device. from [128].

fabricated repeatedly as shown in Fig. 7.11.

Nevertheless, for real world applications such structures need to be integrated into a regular 2-D lattice. By milling bull's eyes next to each other, it was possible to achieve a regular array that can fill up the entire plane as illustrated in Fig. 7.12. For an array having the same periodicity surrounding each eye, one can easily characterize the absolute transmission and it is only 0.5%, much lower than what can be achieved through traditional techniques. Although further optimization of the bull's eyes can lead to much stronger transmittance enhancements [133], it remains doubtful if such bull's eye arrays can be of real use for imaging applications. Therefore we proceeded to a more efficient structure relying on slits with grooves as unit structures as explained below. A supplementary feature of these slits is their polarization sensitivity opening the door for polarimetric filtering with SPs.

7.2 Imaging polarimetry using SPs

Image recording is not always limited to measuring the intensity and the spectral features. Analyzing the state of polarization can extract supplementary information and is a powerful tool for remote imaging systems [128]. One of the simplest way to measure the polarization of the incoming light is to use a rotating element like an analyzer in front of a CCD (see Fig. 7.13). Although such a system has the advantage to be small and robust, the acquisition of the different polarizations is not achieved simultaneously. This consequently reduces the applicability of such a device to moving targets.

Other techniques involve splitting the incoming light beam and redirecting it to different detectors based on polarization (Division of amplitude). The beam-splitting block of such devices typically relies on polarizing beam-splitter cubes

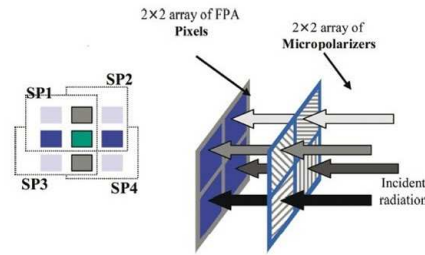


Figure 7.14: Rotating element polarimetric imaging device from [128].

and requires proper alignment of the optical components. This results in large and expensive devices, which in addition are not very robust. Finally, it is also possible to detect the different polarizations on each pixel in a CCD camera, similar to the approach used in the Bayer filter. This can be achieved by placing an array of micropolarizers in front of a detector array (see Fig. 7.13), and has the same limitations as the Bayer filter regarding registration and spatial resolution. Although such devices are small and rugged, the fabrication and alignment of such micropolarizers is more difficult than for the spectral counterpart.

7.2.1 The subwavelength slit as polarization analyzer

In order to design a plasmonic structure that is suitable for both spectral and polarimetric applications, we use a subwavelength slit surrounded by periodic corrugations (period P) as a basic unit [92]. Such a structure can be used as polarization analyzer as its enhanced transmission strongly depends on the polarization of the illuminating light.

In order to achieve a 2 D lattice, the standard slit and groove structure (Fig. 7.15(a)) was modified to fit a diamond shape as shown in Fig. 7.15(b). In a second step, the groove depth gradient was added so that the grooves close to the slit are the deepest (with depths decreasing continuously from $\sim 100\text{nm}$ to $\sim 5\text{nm}$), as shown in Fig. 7.15(c). Test structures combining different basic units were prepared (see Fig. 7.15(d)) in order to characterize and optimize the optical properties before making larger arrays.

The corresponding transmission spectra of such slit and groove (slit length $L = 15\mu\text{m}$, width $sw = 170\text{nm}$, $P = 600\text{nm}$) structures are shown in Fig. 7.16. The fact that the transmission does not vary significantly when the grating is changed

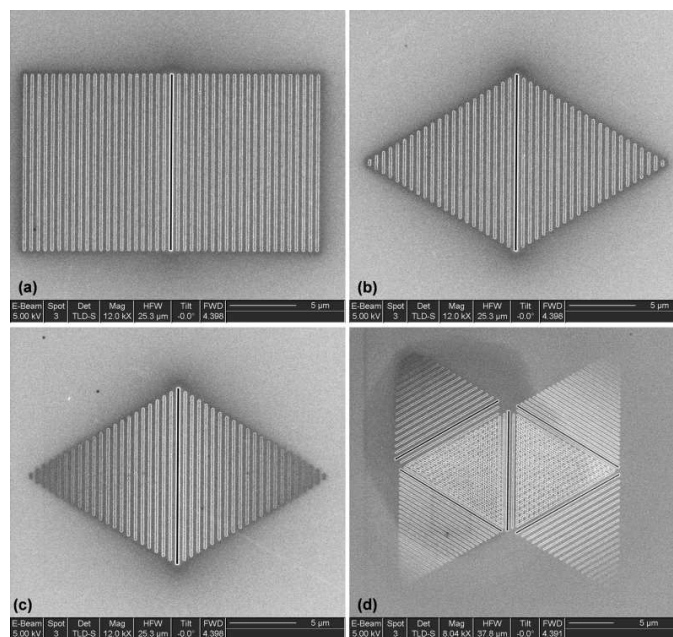


Figure 7.15: Slit and groove structure for different geometries. All structures consist of a central slit of length $15\mu\text{m}$ and width $sw = 170\text{nm}$ in a 360nm thick Ag film and grooves of period $P = 600\text{nm}$. The grooves all have a width of 150nm . (a) Slit with linear grooves of constant depth and length. (b) Slit with grooves of constant depth and diminishing length. (c) Slit with grooves of diminishing depth and length. (d) Slit with grooves of diminishing depth and length combined with other slits surrounded by gratings of different periods (500nm and 700nm) in a triangular lattice such that the gratings overlap 100%.

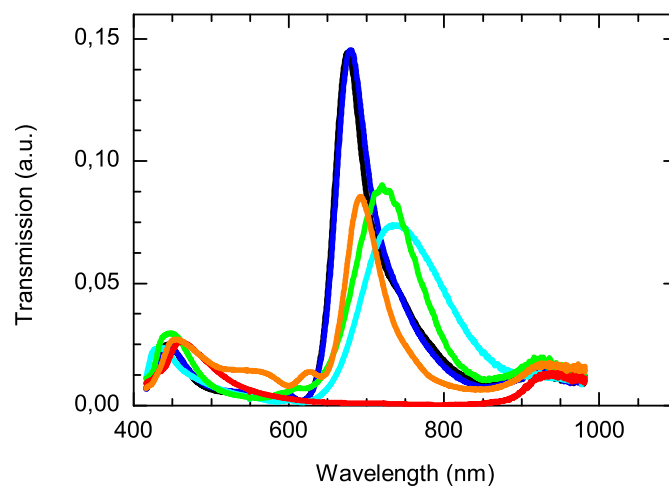


Figure 7.16: Transmission spectra for different geometries of a slit with surrounding grooves. All structures consist of a central slit of length $15\mu\text{m}$ and width 170nm in a 360nm thick Ag film. The grooves all have a width of 150nm . The illumination is polarized perpendicular to the slit except for the red curve. black curve: Structure 7.15(a), blue curve: Structure 7.15(b), cyan curve (perpendicular polarization) and red curve (parallel polarization): Structure 7.15(c), green curve: Structure 7.15(d), and the orange curve corresponds to the same structure with constant groove depth.

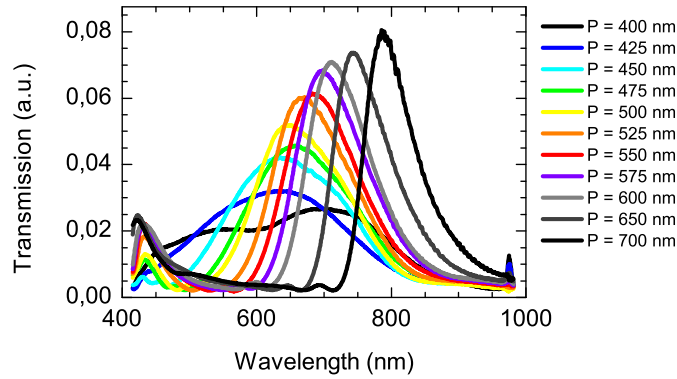


Figure 7.17: Transmission spectra for slit and groove structures with groove depth gradient as shown in Fig. 7.15(c) as a function of the period of the grating. The distance from the central aperture to the gating corresponds to the period.

from the regular shape to a triangular shape is related to high number of grooves ($n = 15 - 20$). It is known that the transmission increases with the number of grooves, but rapidly saturate at around 10 for these wavelengths and structural parameters [134]. In view of the short SP propagation length on the grating, the outer grooves contribute sparsely to the field buildup at the slit.

Introducing a linear gradient in the groove depth reduces and broadens the transmission peak (Fig. 7.16). As can be seen when the polarization is parallel to the slit, the transmission is strongly reduced and the corresponding extinction ratio is around 1 : 100 at the resonance wavelength. This however not results from the disappearance of the SP mode. Indeed the slit has subwavelength dimensions only in one direction and consequently there exist propagative modes inside such an aperture. In particular the reflection of these propagative modes at the interfaces can generate standing waves such as Fabry-Perot modes [85, 87, 92, 135–137]. By changing the polarization from perpendicular to parallel, the cutoff limit of the slit is thus modified in such a way that only the short wavelengths can be transmitted.

The particular advantage of the groove depth gradient structures becomes clear when they are placed in a lattice as illustrated on Fig. 7.15(d). In this case the transmission efficiency is hardly changed within experimental error even though three gratings are overlapping inside each triangle. In the absence of the gradient, the transmission intensity lies in a similar range but the background transmission for wavelengths ranging from 500 – 650nm is much higher and the extinction ratio

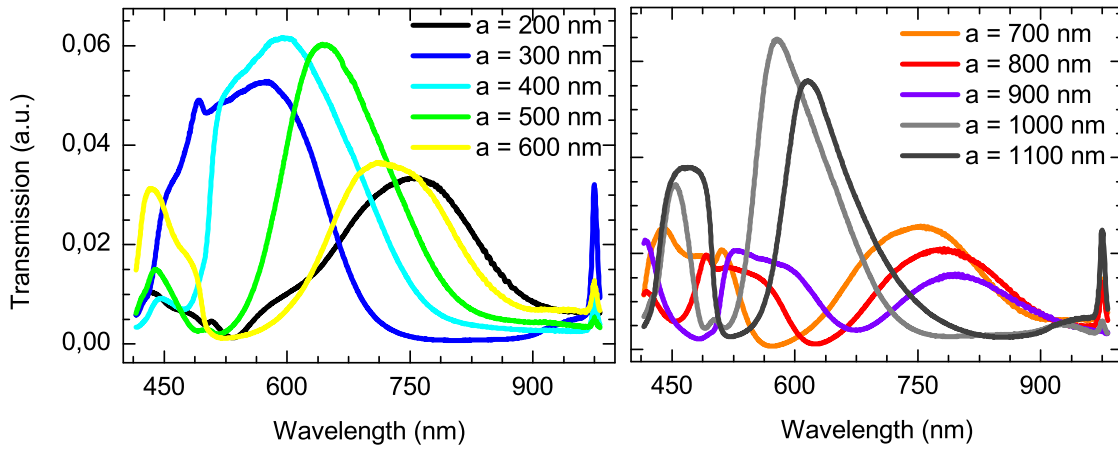


Figure 7.18: Transmission spectra for slit and groove structures with groove depth gradient as shown in Fig. 7.15 (c) as a function of the distance between the slit and the grating.

at the peak wavelength for this configuration is around 1 : 15. Again we relate this to larger perturbation induced the deeper gratings around the slits. Furthermore it should be noted that in the absence of the gradients, the 3 overlapping gratings end up resembling an arrangement of triangular dots sticking out of the surface, increasing the probability of individual scattering events at these bumps.

The enhanced transmission properties can be adjusted by modifying the structural parameters. The main transmission peak is to a large part determined by the SP resonance of the grating, following the same basic coupling relation as in the case of a bull's eye. In order to tune the color of the transmitted light, slit and groove structures with varying period were fabricated. In Fig. 7.17 the corresponding transmission spectra are represented for perpendicular polarization at normal incidence. While for large periods an intense peak can be observed, the transmission spectra associated with the smaller periods broadens. The main resonance even begins to split for the shortest period shown ($P = 400\text{nm}$). This is most likely due to the presence of a Fabry-Perot mode which typically occurs at wavelengths twice the depth (360nm). This appears to be the case judging from the maximum round 700nm .

The results in Fig. 7.17 indicate that it is difficult to design a structure that provides a transmission peak at small wavelengths in the visible by only adjusting the period. That is why in a second step, we fabricated slit and grooves structures

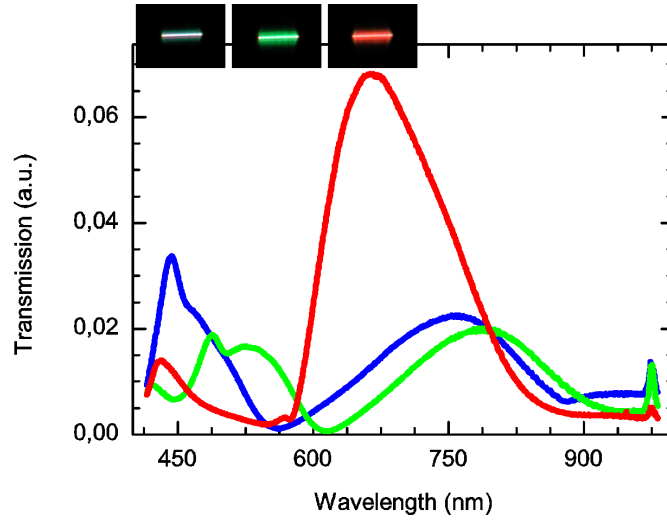


Figure 7.19: Transmission spectra for slit and groove structures in a 360 nm thick Ag film adjusted to have transmission peaks for blue ($P = 450\text{nm}$ $a = 700\text{nm}$), green ($P = 500\text{nm}$ $a = 775\text{nm}$) and red light ($P = 575\text{nm}$ $a = 500\text{nm}$).

for which the distance a from the grating to the central aperture was varied. As can be seen on Fig. 7.18, the transmission spectra are strongly affected by such modifications leading to a displacement of the resonances. This is related to a change in the phase and therefore in the constructive interference conditions at the position of the slit ([114, 138, 139]. This has been confirmed by other studies in the laboratory [134]. We will at this point not discuss in further detail the underlying physics of this process but rather concentrate on the experimentally observed results and its implications for our study.

After completing a certain number of tests, a choice of the parameters P and a was found that enables high transmission at the wavelengths corresponding to the three main colors of the visible spectrum: blue, green and red. The transmission spectra are shown on Fig. 7.19, together with microscope pictures of the structures when illuminated with white light.

7.3 Combining slits in a honeycomb array

As already discussed, in order to use such slit and groove structures for spectral imaging and polarimetry, the basic unit structures need to be tested in a large

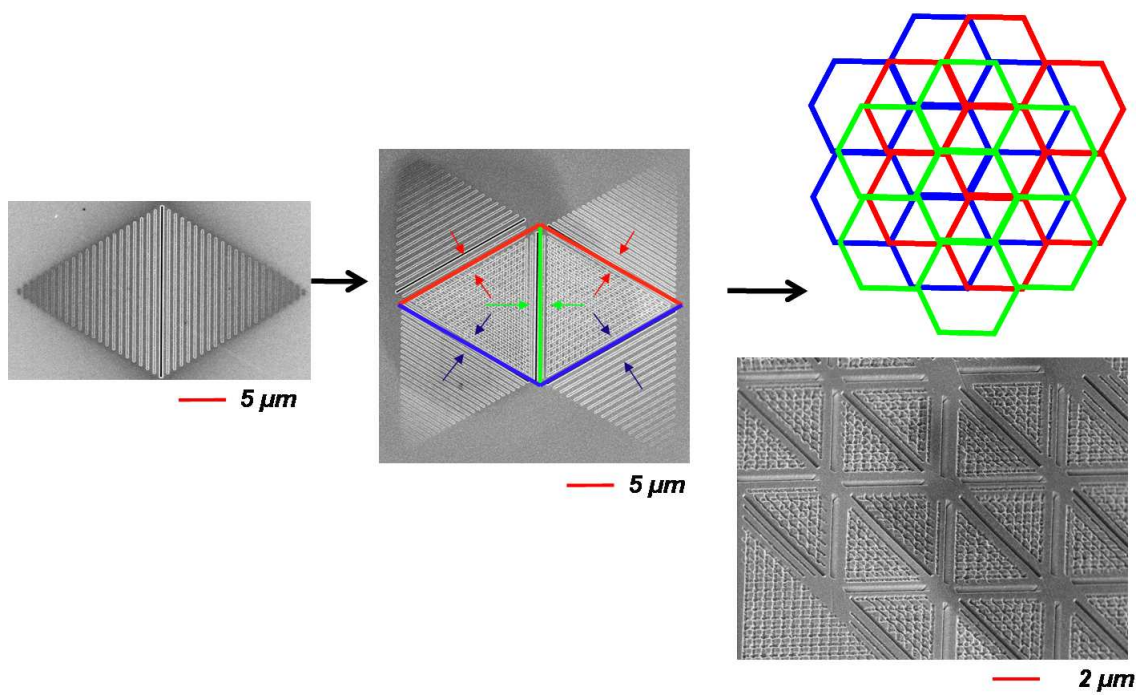


Figure 7.20: Polarimetric image sensing architectures using slit and groove structures in a honeycomb array.

array. The three basic colors can be fit into a triangular lattice as shown in Fig. 7.20. Different arrays of such multiple slit structures were fabricated like the one shown on Fig. 7.21. The photograph recorded through the microscope in Fig. 7.21 illustrates that the spectral selectivity is preserved inside the lattice.

By using the same approach as for the bull's eye structures, it was possible to determine the absolute transmission of such an array and the corresponding efficiencies are given in table 7.1.

	overall	red	blue (450nm)	green (500nm)	green (550nm)	orange (600nm)	red (650nm)
width 170nm Length 15 μ m	1.17%	1.18%	1.73%	1.86%	0.59%	0.98%	1.36 %
width 250nm Length 5 μ m	3.7%	3.75%	14.45%	9.22%	6.26%	6.17%	9.02 %

Table 7.1.

For structures like those shown in Fig. 7.21 having slit length of 15 μ m and slit width of 170nm, the transmission is in the range of 1 to 2 %, again far smaller than what is achieved by traditional techniques. One way to increase this overall transmission is to downsize the whole structure by reducing the size of each slit and consequently the number of grooves. For the lattice with a 15 μ m slits, there are typically about 20 grooves in the triangular gratings. Considering this high number of grooves, it should be possible to reduce the size of the triangular lattice and thereby increase the slit density and the absolute transmission of the device. It was checked that the transmission of these structures remained efficient for smaller slit lengths or for small modifications of the slit width as shown in Fig. 7.22. It can be seen that the spectral response is also preserved. It should also be noted that such a size reduction results in a higher resolution for the total device as the effective pixel size is much smaller. A corresponding lattice composed of slits of length 5 μ was is shown in Fig. 7.23.

As expected, the absolute transmission of such an array is significantly larger, especially if the width of the central slit is slightly increased (see Table 7.1). The measured transmission intensities for a downsized structure are in the range of 10 – 15% at the peak wavelengths. Although this is still slightly smaller than

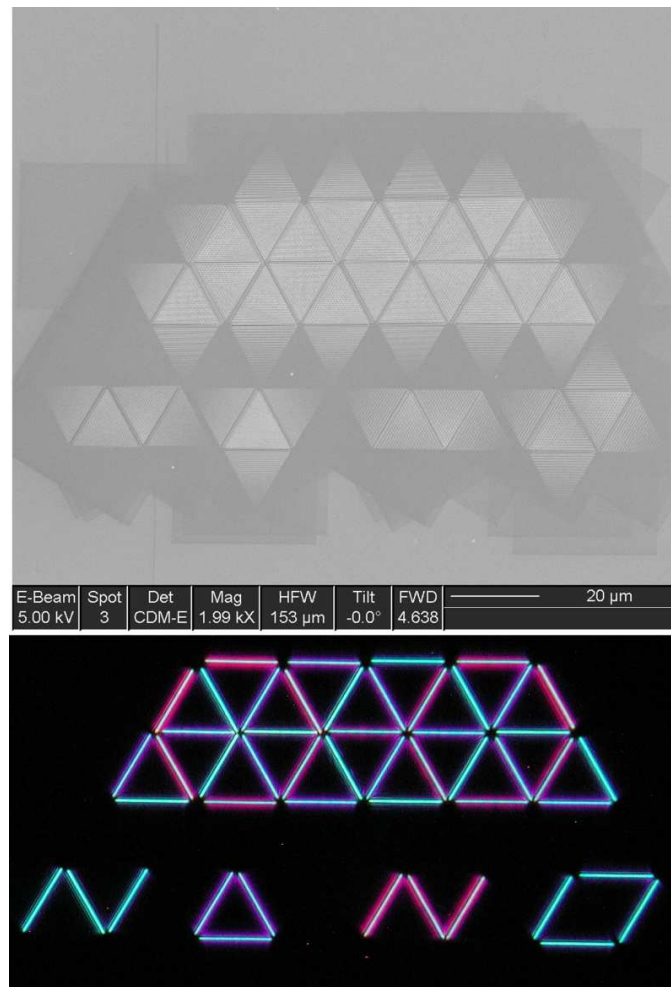


Figure 7.21: SEM and photograph image through a microscope when illuminated with unpolarized white light of a regular lattice of slit and groove structure. The length of each slit is $15\mu\text{m}$, width is 170nm , depth $h = 360\text{nm}$, the grooves have a varying depth and a width of 150nm . The parameters of the grating are the same as in Fig. 7.19.

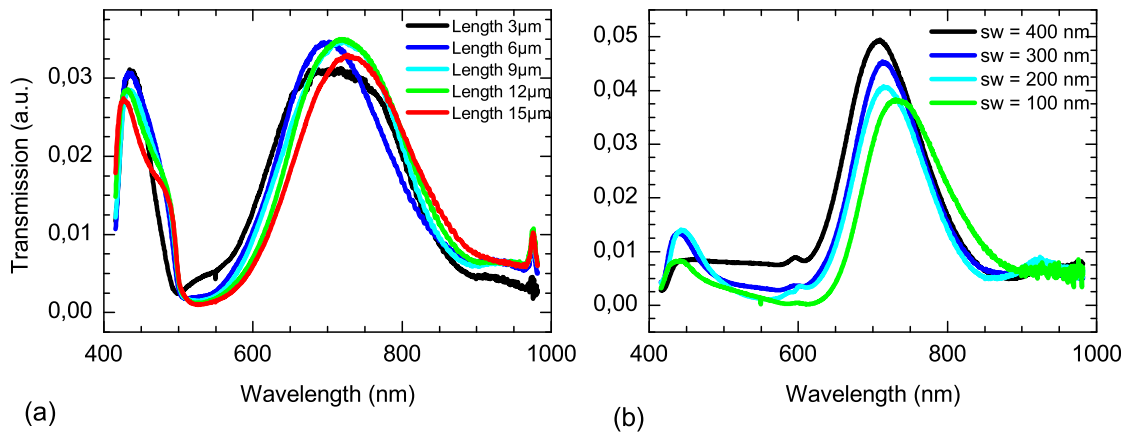


Figure 7.22: (a) Transmission spectra for slit and groove structures of period 500nm and a 700nm for slits of different lengths. (b) Transmission spectra for slits of different widths. The transmission spectra are normalized to the area of the aperture showing that the transmission per unit area is preserved.

what can be obtained with the Bayer filter, it is to be expected that even higher efficiencies are possible through careful optimization of the different parameters as in the case of bull's eyes [133].

The transmission through such slit lattices was also studied as a function of the polarization of the incident light as can be seen in Fig. 7.24. As the polarization is rotated, different slits light up, giving maximum transmission when the electric field is perpendicular to the slit. When the polarization is parallel, only the short wavelengths below the cutoff wavelength of the slit are transmitted, giving a blue hue in the image as explained previously. The lattice is designed in such a way that a color that can not be not collected at a particular slit because of its polarization will be collected in neighboring slits oriented at different angles. This is a result of our specific lattice design giving 3 complementary directions for each color at regular spacings.

Among the myriads of spectral and polarimetric imaging techniques [127, 128], the concept proposed here is one of the few which allow simultaneous acquisition of a complete spectral image. This is also the case for commercial color cameras based on Bayer filter arrays [131], stacked photodetector structures [140] or "3-CCD" techniques using beam splitters and separate detector arrays, as well as many-band techniques based on tomographic reconstruction [141] or image replication [129].

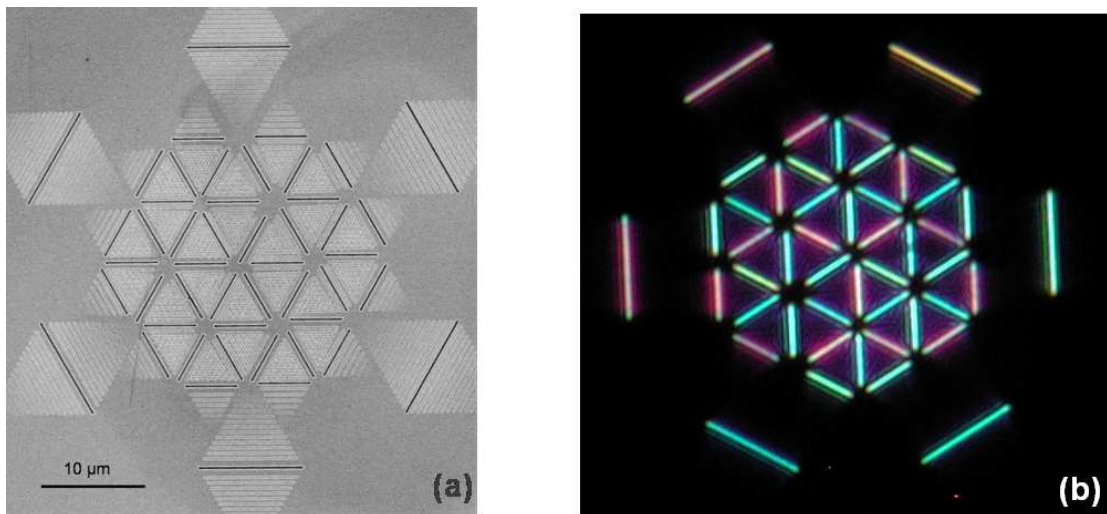


Figure 7.23: Downsized lattice of slit and groove structures. The length of one slit is $5\mu\text{m}$, the width 170nm , with 5-6 grooves of varying depth and length. The outer slits have a length of $10\mu\text{m}$ and have parameters adjusted to transmit light at different wavelengths from blue to red. (a) SEM image of a the lattice. (b) Microscope image of the lattice when illuminated with unpolarized white light.

However, these techniques have disadvantages due to incomplete sampling of the image, limited photon efficiency or complex fabrication. Conventional color imaging techniques do not scale well to more than three spectral bands. Most many-band spectral imagers employ some form of scanning, which leads to spectral artifacts for nonstationary scenes and/or loss of throughput. The in-plane photon sorting capacity of surface plasmons offers new opportunities for improvement in spatial resolution, band registration, band count, throughput, simultaneity or simplicity, depending on what technology it is compared with.

There is an obvious potential for extending the concept to more spectral bands, especially into the near-IR where surface plasmon resonances become sharper with higher Q factors. As in conventional imaging techniques, the practical limit on the number of bands feasible with plasmonics-based spectral imaging will depend on system tradeoffs involving transmission efficiency, band registration and the numerical aperture of the collection lens. Introducing plasmonic structures on the exit surface of the aperture can achieve potentially useful beaming and lensing effects [92, 94, 95]. Furthermore, it is important to note that the antenna effect of the plasmonic structure permits reduction in the underlying photodetector size, with

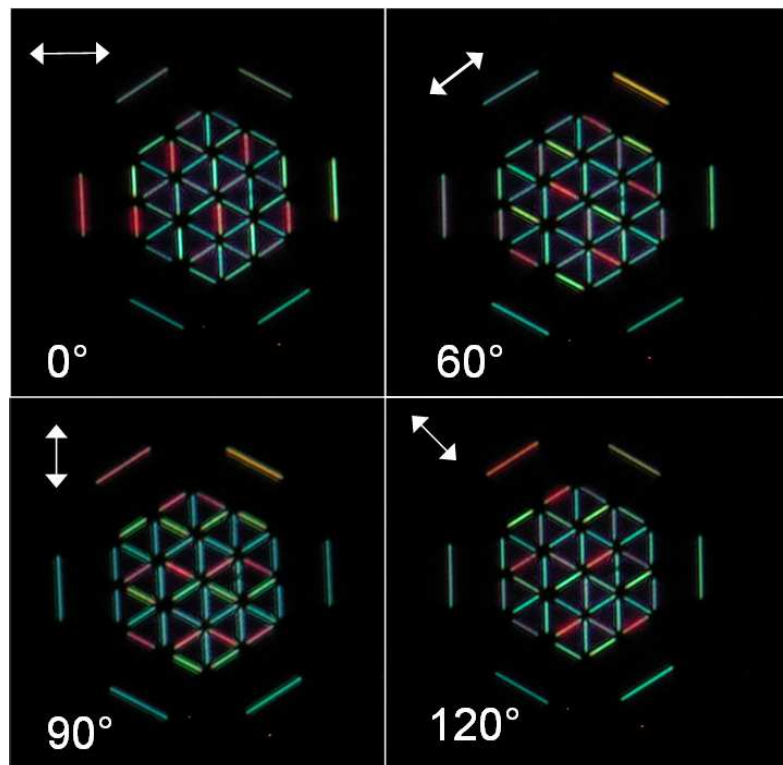


Figure 7.24: Microscope images of the structure shown in Fig. 7.23 for different polarization of the incident light. The polarization direction is indicated by the white arrows.

potential gains in speed [142] and/or chip dimensions. Mass production of photon sorting structures should be feasible using current fabrication techniques, which involve structuring on tens of nanometer scales. Like all spectral and polarimetric imaging techniques, the concept presented here is subject to limitations, but it has unique advantages due to the capacity of surface plasmons to be sorted in the detector plane and therefore opens a new design path worth exploring [82, 143].

Chapter 8

Conclusion and outlook

The work presented in this thesis addressed some fundamental questions concerning the light transmission through subwavelength holes as well as a new application of plasmonic structures to spectral and polarimetric imaging.

The study of arrays of subwavelength holes as a function of the hole diameter and depth enabled to clarify some specific aspects of the EOT phenomenon. Through a systematic analysis it was possible to precisely characterize the whole range of transmission intensities that can be achieved through simple modification of these geometrical parameters of the hole. Understanding how an array can be tailored to feature a specific transmittance is of increasing importance considering the amount of interest that hole arrays have received in recent years. We could also observe that the evolution of the transmission follows similar trends as classical waveguides in the non-propagative limit, but it became obvious that an accurate description needs to consider surface resonances. This could be taken into account by describing the transmission process as an interference effect of the direct transmission through each hole and the SP related resonant transmission. Through this analysis the transmission peaks could be fitted for a specific hole depth and the evolution of the fitting parameters revealed the presence of a transition. This transition that we related to the cutoff limit of the hole showed specific signatures in peak position shift, peak width and corresponds to an optimum ratio between the direct and the resonant contribution. This can be of particular interest for the design of hole arrays in a variety of applications such as filtering or SP-molecule interactions.

In the following part we took interest in the diffractive properties of subwavelength apertures, which also need to be considered when designing structures for a

given application, especially those involving individual holes. Although this study could not be completed as planned, the experiment that was set up already enabled number of interesting observations. Subwavelength apertures do not diffract as predicted by classical models in agreement with previous studies. The preliminary measurements on holes surrounded by periodic corrugations indicate that the polarization of an incoming light beam is a determining factor in the resulting diffraction pattern. With the optical system that was built, the pursuit of these measurements is expected to clarify the role of various factors that probably influence the diffraction pattern of such small holes. It should be noted that the use of this specific experimental setup will not be limited to the study of the diffraction of single apertures, but will also be of valuable use in the laboratory for diffractive characterization of any future nanostructure. Understanding diffraction at small scales is ever more important considering the emergence of nano-optics.

Finally the combination of different gratings in a single plasmonic structure suggest a new path for photon sorting. The novel structures that we designed have the unique properties to excite at a given location different individually controllable SPs which are directed to specific locations where the light can be transmitted through subwavelength apertures. This spectral filtering capacity of surface plasmons is even preserved when the unit structures are made polarization sensitive. The efficiencies that could be observed for such arrays combining spectral and polarimetric filtering lie in a range that justifies applicability to real-world devices. It should however be noted that our approach has its own limitations. Nevertheless as none of the existing systems are perfect, there is a real potential for plasmonic photon sorters. This is motivated among other things by the possibility of expanding the concept to the infra-red where higher SP propagation lengths and transmission intensities should be possible. The implementation and optimization of such structure on real photodetectors will no doubt be tested in the future considering the rise in interest for plasmonics in photodetector industry.

Appendix A

Acquisition of dispersion curves

As explained in Chapter 3, the dispersion of surface plasmons can be measured by tilting the sample with respect to the optical axis. Some transformation of the experimental data points is therefore required to plot the curves as a function of the more physical variables energy E and wavevector k_x .

We will describe the procedure for a typical hole array (period $P = 460\text{nm}$, hole diameter $d = 150\text{nm}$) of 30×30 holes in a 180nm thick Au film deposited on a glass substrate. To measure the dispersion, transmission spectra were recorded for polarization along the rotation axis for different angles of illumination θ using the setup explained in Chapter 4. For this measurement the angle was varied continuously from -20° to 35° with a step of 1° . The corresponding data points are consequently evenly spread over a discrete grid of λ and θ ($I = f(\lambda, \theta)$) as shown in Fig. A.1. This corresponds to an irregular grid of E and k_x which are related to λ and θ by:

$$k_x = \frac{2\pi}{\lambda} \sin\theta \quad (\text{A.1})$$

$$E = \hbar \frac{2\pi c}{\lambda} \quad (\text{A.2})$$

where \hbar is the reduced Planck constant. In a first step the data points $I = f(\lambda, \theta)$ are interpolated on a regular grid of λ and k_x which leads us to the set of data points shown in Fig. A.2. In a second step, this data points are interpolated in also in the other dimension leading to a regular grid of E giving the usual dispersion curve as illustrated in Fig. A.3.

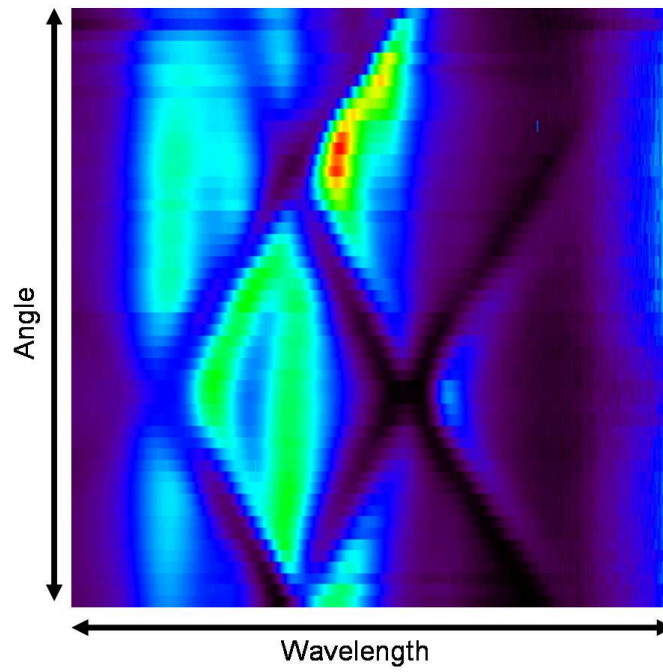


Figure A.1: Measured data points on a regular grid of λ and θ : $I = f(\lambda, \theta)$.

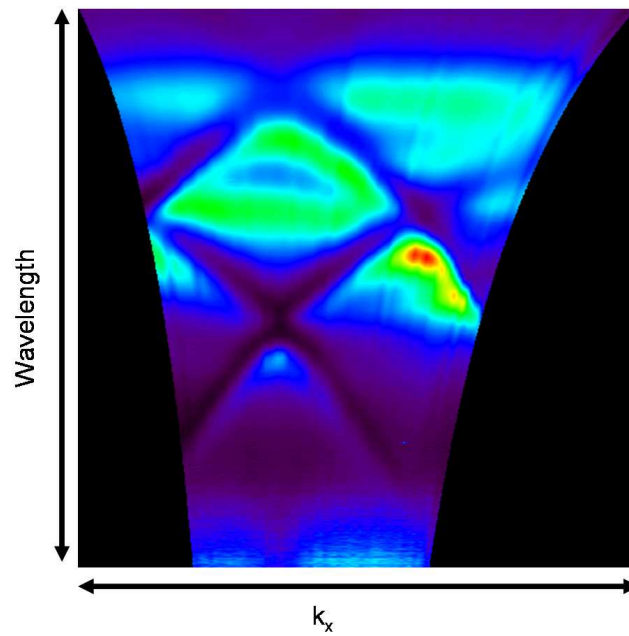


Figure A.2: Data points interpolated from the data shown in Fig. A.1 on a regular grid of k_x and λ $I = f(k_x, \lambda)$.

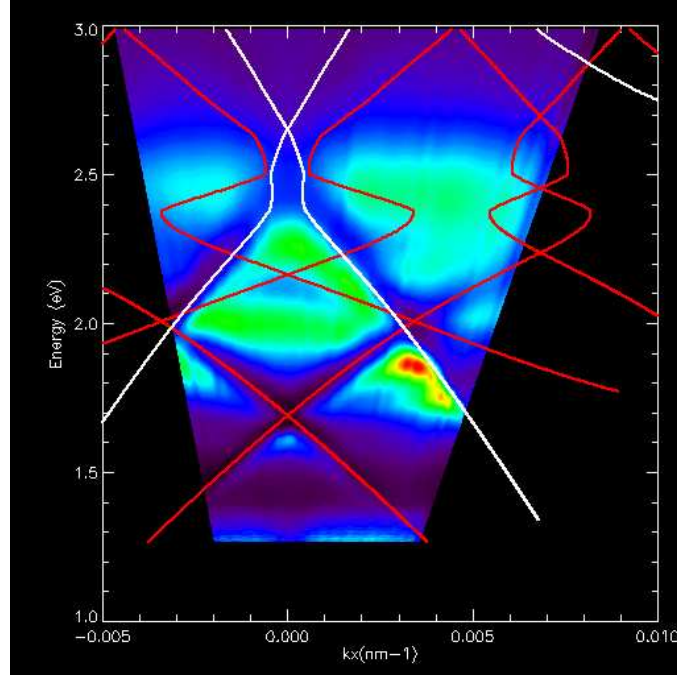


Figure A.3: Data points obtained from interpolating the data of Fig. A.2 on a regular set of E . The white and red curves correspond to the interpolated solutions of Eq.(A.3).

Determining the corresponding theoretical resonance position also requires some computational work. The resonance condition given by Eq.(3.3) in Chapter 3 can be rewritten for an angle of illumination θ in the case of light polarized normal to the rotational axis of the sample as follows:

$$\sin\theta = \frac{\lambda}{2\pi} \left[\sqrt{\left(\frac{2\pi}{\lambda} \sqrt{\frac{\varepsilon_m \varepsilon_d}{\varepsilon_m + \varepsilon_d}} \right)^2 - \left(\frac{2j\pi}{P} \right)^2} - \frac{2i\pi}{P} \right] \quad (\text{A.3})$$

For a certain values of the indices (i, j) and the wavelength λ , a real solution of θ can be found describing a resonance condition. These curves given as a function of λ and θ are then interpolated on a regular grid of E and k_x in the same way as our experimental data. The corresponding curves are plotted as red (Au-glass) and white (Au- air) lines for the modes corresponding to the different metal interfaces in Fig. A.3.

Appendix B

Transmission through hole arrays with index-matching liquid

In Chapter 5, the transmission of hole arrays was studied as a function of hole diameter and depth in the case of non symmetric interfaces. The transmission through the corresponding hole arrays was nevertheless also measured in the symmetric case by covering the metal film with an indexmatching liquid ($n = 1.54$) and the results are presented in this appendix.

In Fig. B.1, the transmission spectra of hole arrays (period $P = 460\text{nm}$ film thickness $h = 180\text{nm}$) are shown for different hole sizes. The transmission intensities are much larger than for the hole arrays in the nonsymmetric configuration discussed in Chapter 5. This is expected from the coupling of the modes on both interfaces [77, 78, 102, 103] and also leads to the peak splitting that can be observed in Fig. B.1 for the larger holes. EOT can be obtained in this case already for small holes. However as the transmission peak increases much stronger with hole size, the peak also becomes much broader to the point where it clearly spreads to wavelengths that can not be accessed with our setup. This limits strongly our analysis for large holes as not all the spectral information relied to one transmission peak can be obtained.

The dispersion curves were also measured for holes of different sizes and are shown in Fig. B.2. Due to the coupled interfaces, the number of minima and peaks is reduced and the intensity of the remaining peaks is enhanced.

The transmission spectra were also acquired for a whole set of hole depth and the corresponding curves are plotted in Fig. B.3. The general evolution follows a

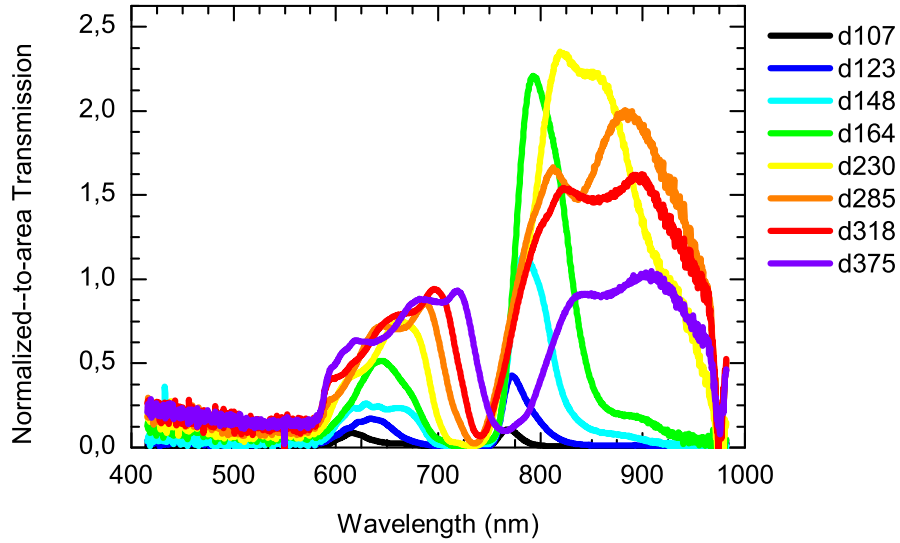


Figure B.1: Transmission spectra of hole arrays (30×30 holes) of period $P = 460\text{nm}$ in a Au film of thickness 180nm deposited on a glass substrate and covered with an index-matching liquid. The hole size is varied continuously from 100 to 360nm .

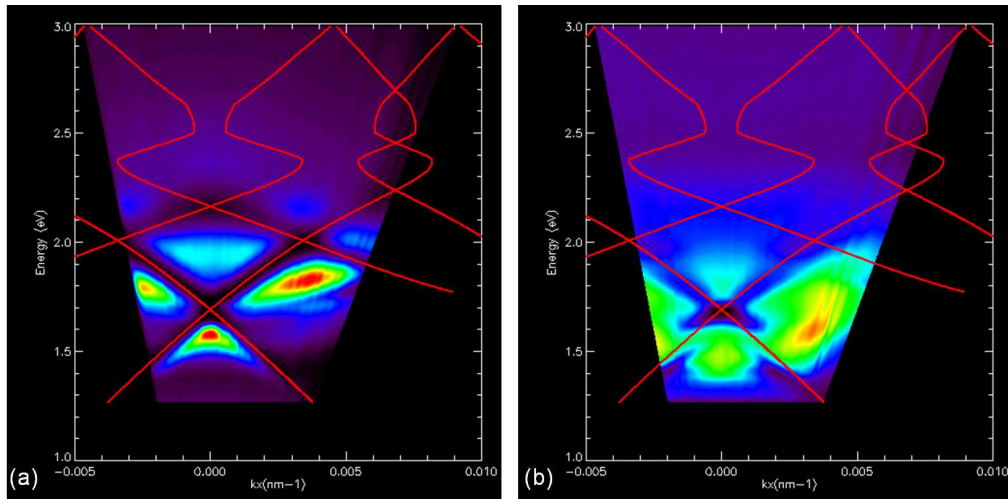


Figure B.2: Dispersion curves of different hole arrays (period $P = 460\text{nm}$) in a metal film deposited on a glass substrate covered with index-matching liquid together with the theoretical peak positions according to equation (5.16). (a) hole size $d = 150\text{nm}$, hole depth $h = 190\text{nm}$, (b) $d = 350\text{nm}$ and $h = 190\text{nm}$, The color scale is different for each dispersion curve and optimized to produce the best possible contrast.

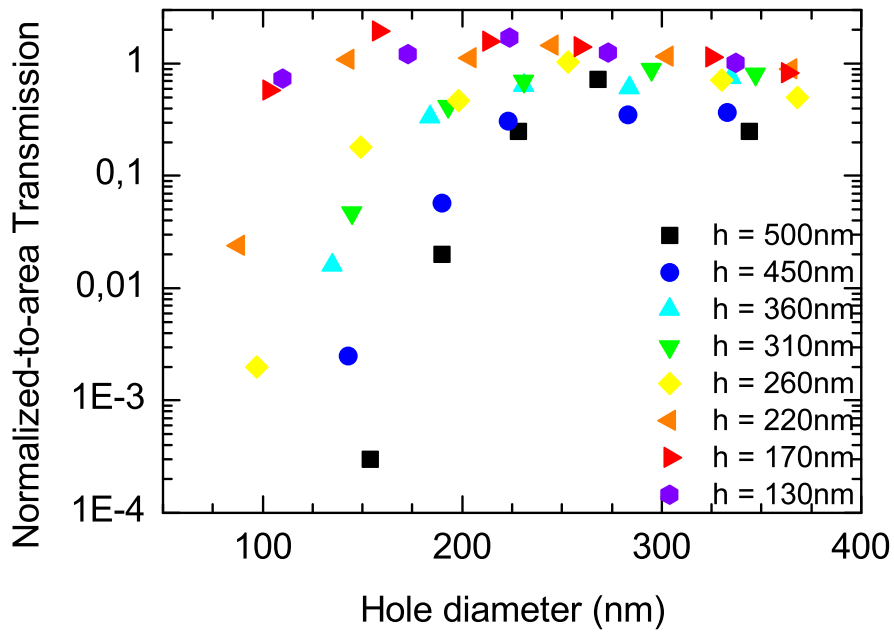


Figure B.3: The points correspond to the transmission peak intensities of the (1, 0) mode for hole arrays milled in Au films of varying thickness deposited on glass substrates and covered with an indexmatching liquid ($n = 1.5$).

different behavior than in the non-symmetric case. For the smaller holes however an evolution is similar than what could be observed in the non-symmetric case. This changes above a certain hole size as could also be predicted by theoretical studies [103] and confirmed by previous experimental studies [102].

A detailed study as the one in Chapter 5 could however not be achieved in this case as we do not have precise knowledge of the part of the transmission peak that spreads too far into the IR to be detected with our setup.

Appendix C

Labview program control panels and code schemes

As explained in Chapter 6, the experimental data acquisition of the diffraction measurements was accomplished by an all-automated Labview program. On the following pages the different control panels and code diagrams can be found for the main acquisition program as well as for the subroutines used to communicate with the different apparatus. The programs for the data acquisition as well as the control of the rotation unit were written from scratch. For the other subroutines, control programs were provided with the devices and were modified to fit our specific tasks.

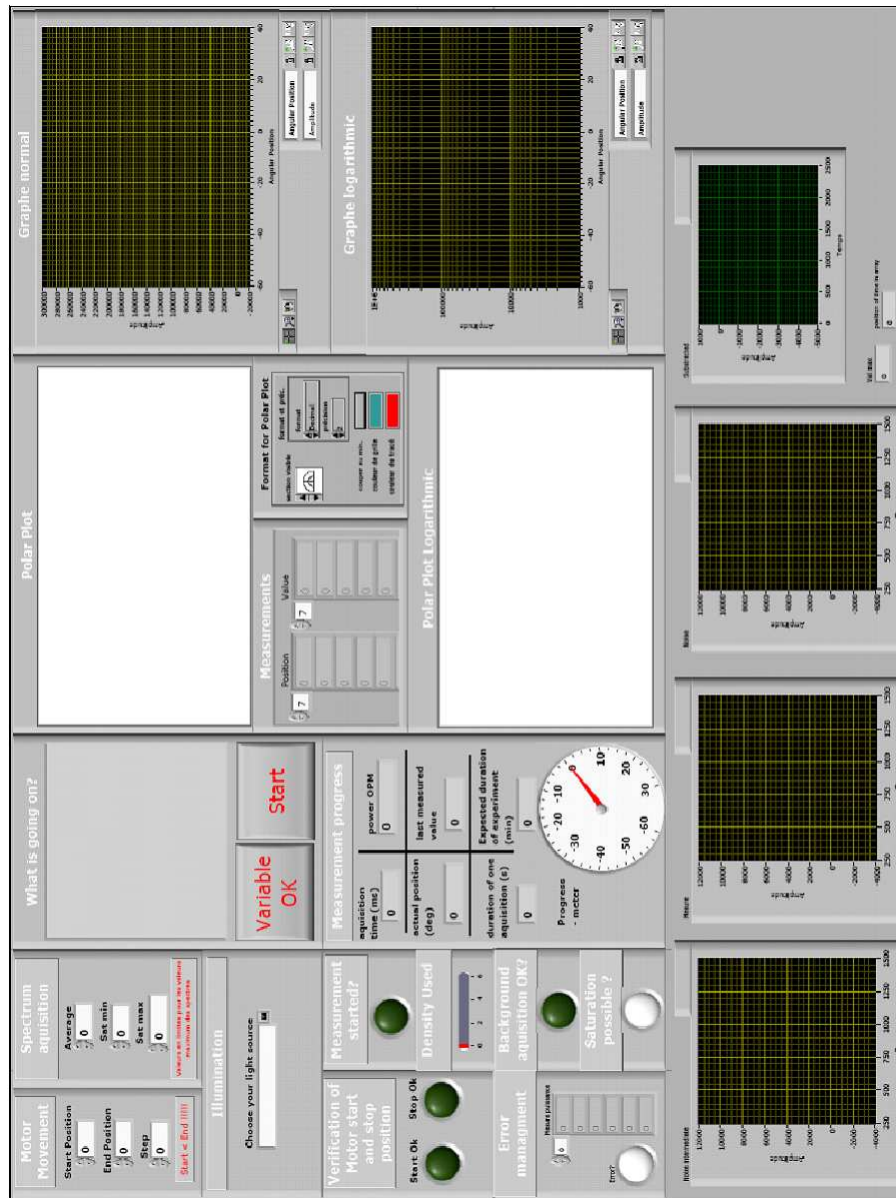


Figure C.1: Front panel of the Acquisition program. Through this user interface, the different acquisition parameters (angles, angular step, averaging,...) are input. In addition it provides the user with a constant progress report of the measurement as well with an estimated duration. In the different graphs, the experimental data is plotted after measurements and it also enables the output of the data as ascii files.

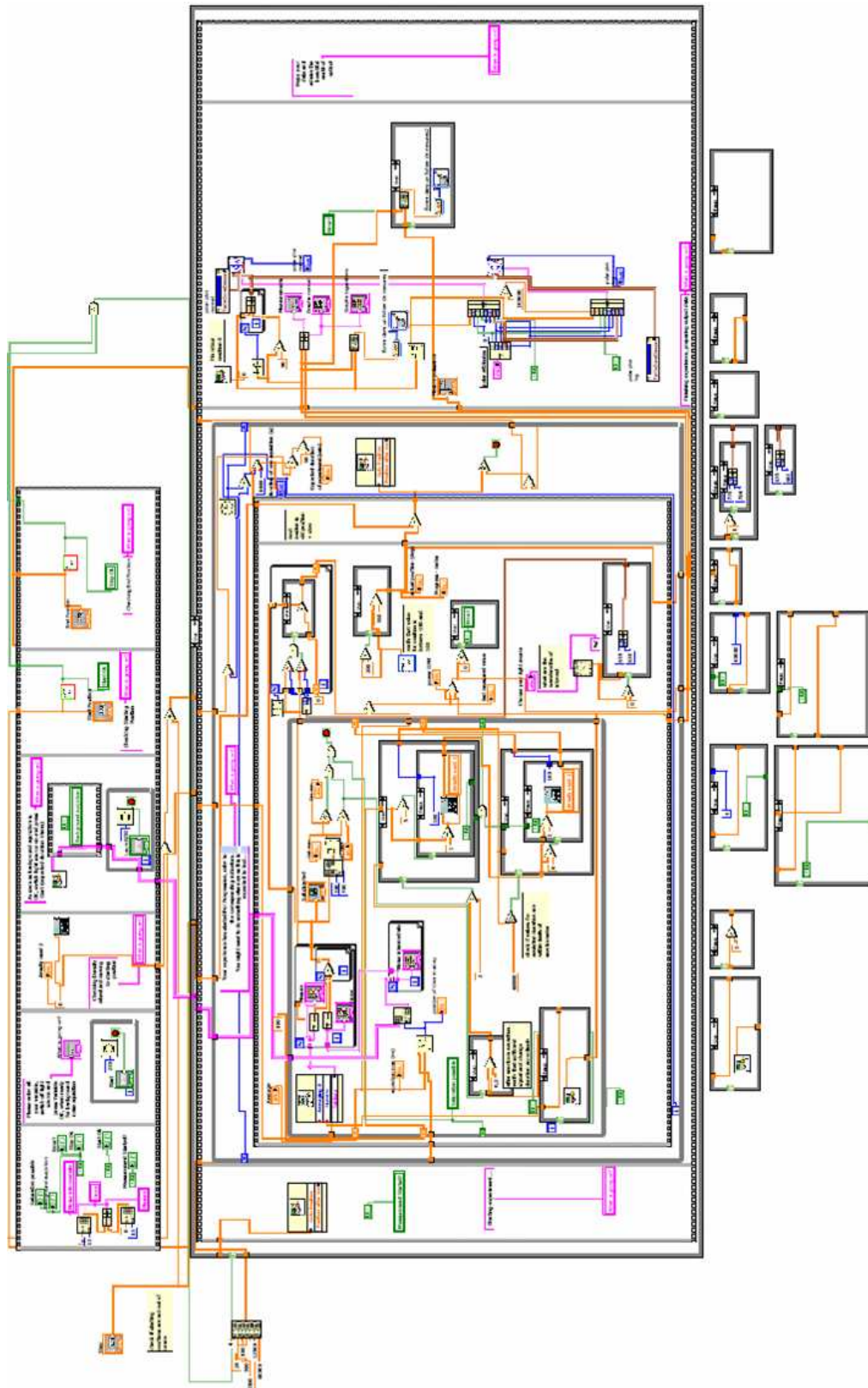


Figure C.2: Code scheme of the program dedicated to the control of the acquisition as explained in Chapter 6.

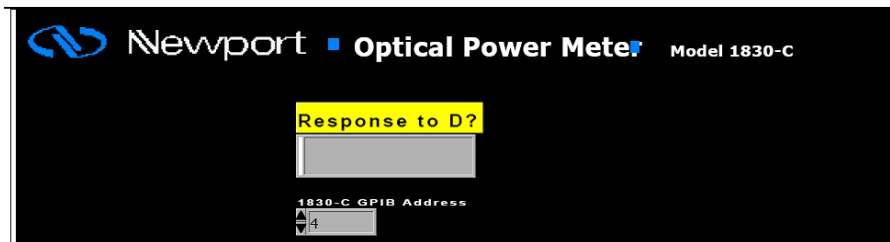


Figure C.3: Control panel of the subroutine program dedicated to the control of the optical power meter 1830-C from Newport.

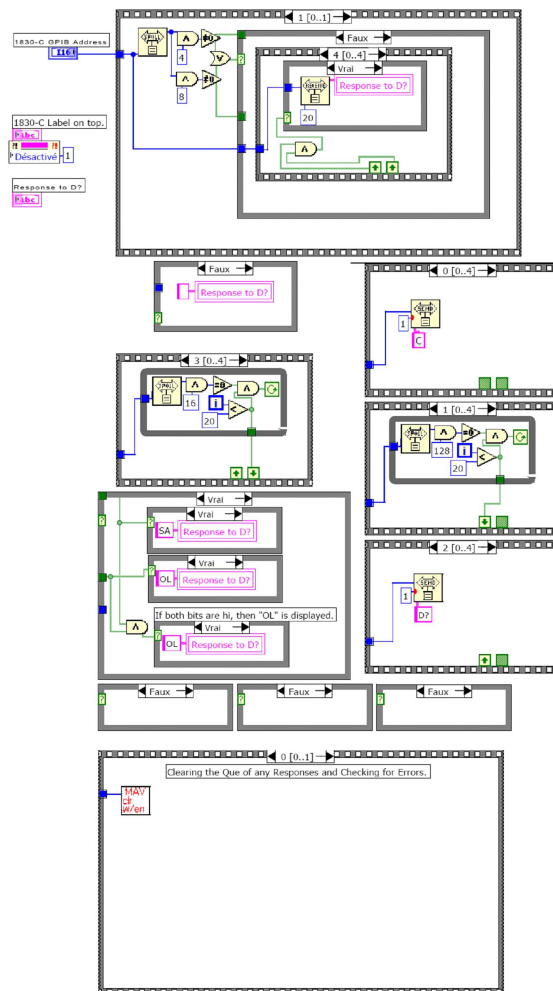


Figure C.4: Code scheme of the subroutine program dedicated to the control of the optical power meter 1830-C from Newport.



Figure C.5: Control panel of the subroutine program dedicated to the control of the filter wheel.

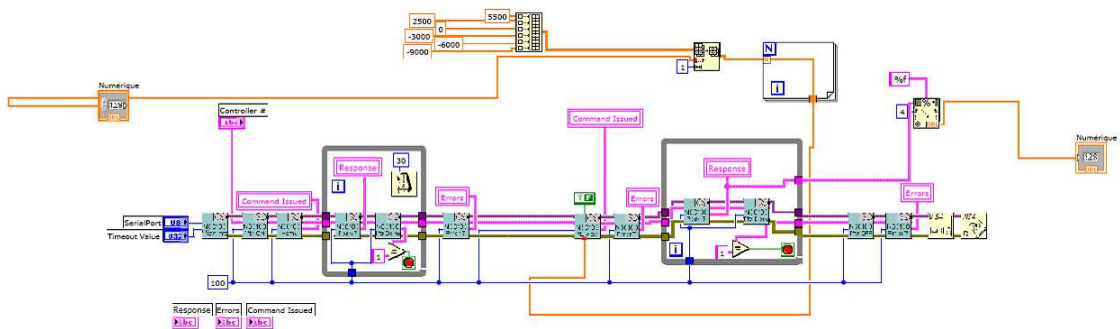


Figure C.6: Code scheme of the subroutine program dedicated to the control of filter wheel.



Figure C.7: Control panel of the subroutine program dedicated to the control of the rotation motor unit (Thorlabs T-cube TDC001).

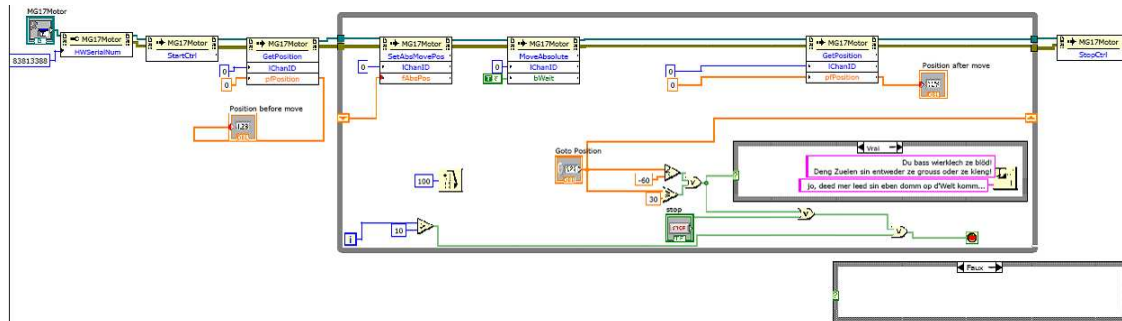


Figure C.8: Code scheme of the subroutine program dedicated to the control of the rotation motor unit (Thorlabs T-cube TDC001).

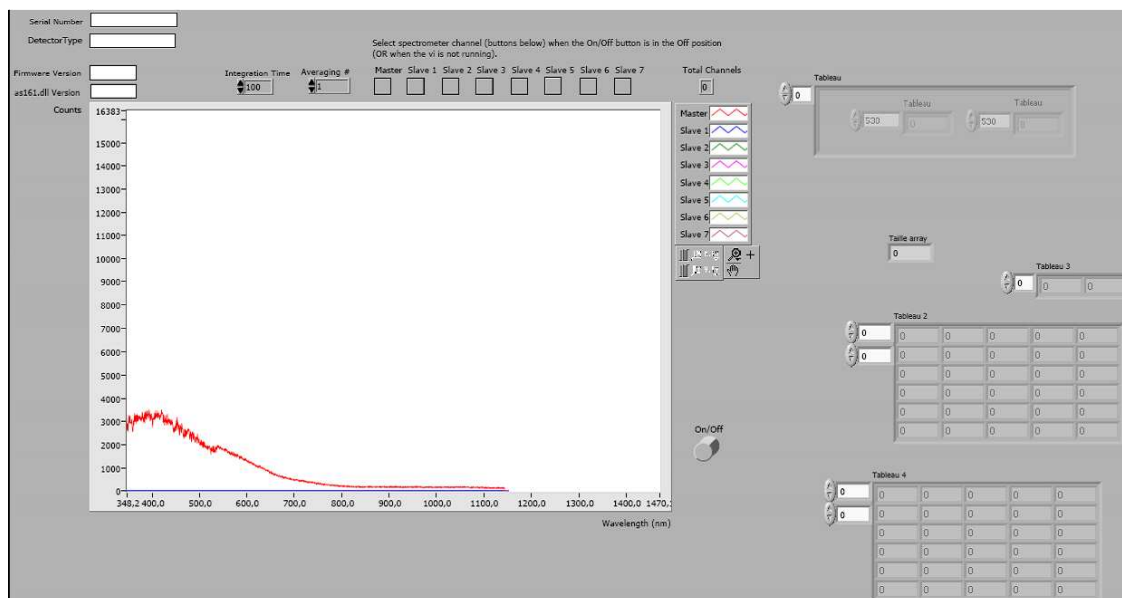


Figure C.9: Control panel of the subroutine program dedicated to the acquisition of spectra from the Avantes Avaspec 2048TEC spectrometer.

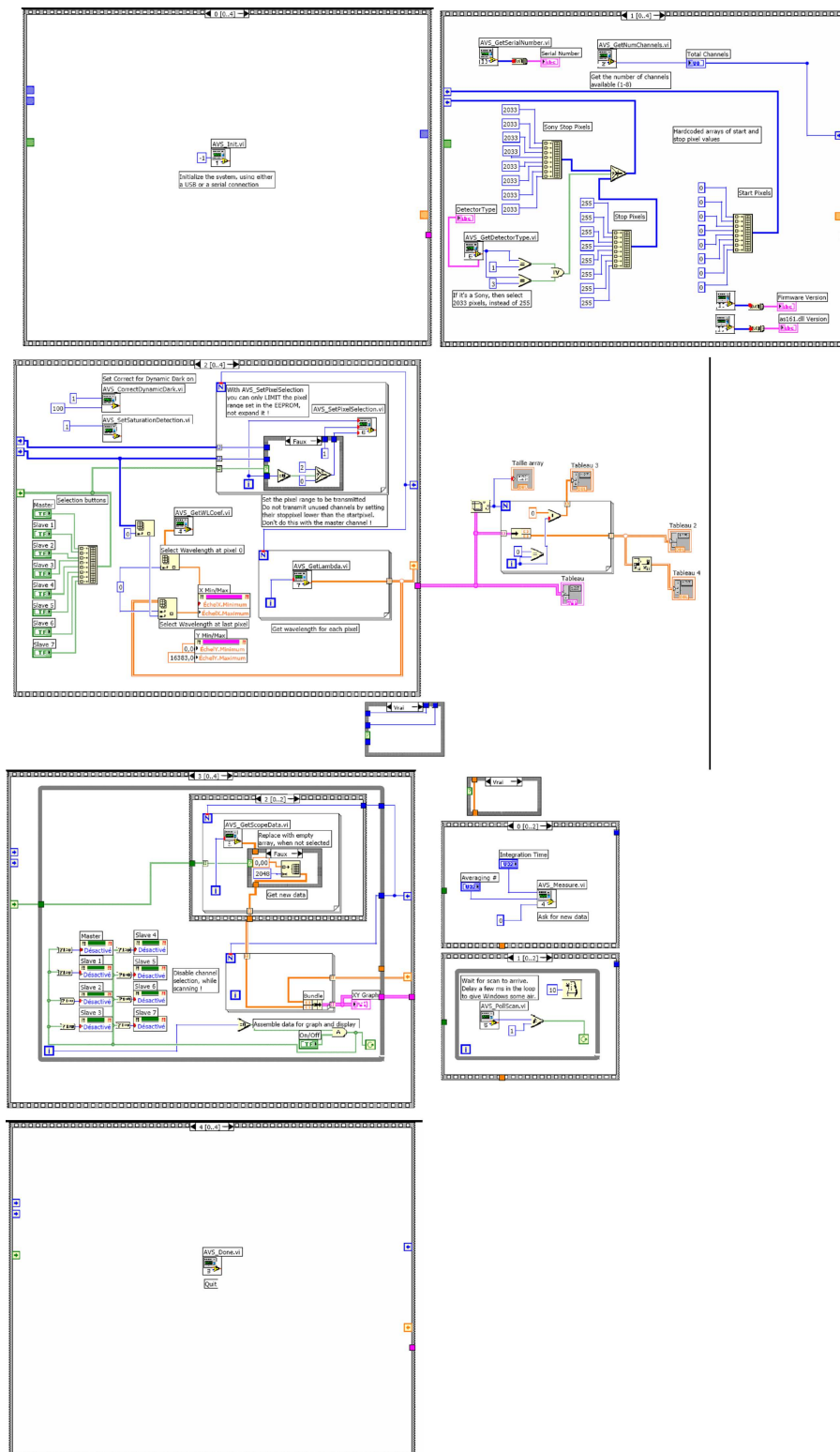


Figure C.10: Code scheme of the subroutine program dedicated to the acquisition of spectra from the Avantes Avaspec 2048TEC spectrometer.

Bibliography

- [1] J.H. Hammond. *The Camera Obscura. A Chronicle.* Adam Hilger Ltd., Bristol, 1981.
- [2] http://en.wikipedia.org/wiki/Camera_obscura.
- [3] <http://en.wikipedia.org/wiki/Mozi>.
- [4] <http://www.pa.ash.org.au/acetech/PAPERS/RHOKYM.HTM>.
- [5] Aristotle. *Problems I. Books I-XXI. With an English translation by W. S. Hett.* William Heinemann Ltd., M.A. London, 1936.
- [6] G. Frisius. *De Radio Astronomica et Geometrica.*
- [7] http://en.wikipedia.org/wiki/Ibn_al_Haytham.
- [8] R. L. Verma. *Al-Hazen: father of modern optics.* 1969.
- [9] http://en.wikipedia.org/wiki/Robert_Grosseteste.
- [10] http://en.wikipedia.org/wiki/Roger_Bacon.
- [11] Hooke. *Micrographia.* 1665.
- [12] http://en.wikipedia.org/wiki/History_of_optics.
- [13] M. Born and E. Wolf. *Principles of Optics.* Cambridge University Press, Cambridge, 2006.
- [14] E. Hecht. *Optics.* Pearson Education, San Francisco, 2002.
- [15] L. Novotny and B. Hecht. *Principles of Nano-Optics.* Cambridge University Press, Cambridge, 2006.

- [16] G. Libri. *Histoire des sciences mathematiques en Italie*. 1840.
- [17] L. Novotny. The history of near-field optics. *Progress in Optics*, 50:137, 2007.
- [18] J.A. Veerman, A.M. Otter, L. Kuipers, and N.F. van Hulst. High definition aperture probes for near-field optical microscopy fabricated by focused ion beam milling. *Appl. Phys. Lett.*, 72:3115, 1998.
- [19] E.H. Synge. A suggested model for extending microscopic resolution into the ultra-microscopic region. *Phil. Mag.*, year =.
- [20] A. V. Baez. Is resolving power independent of wavelength possible? an experiment with a sonic 'macroscope'. *J. Opt. Soc. Am.*, 46:901, 1956.
- [21] E.A. Ash and G. Nicholls. Super resolution aperture scanning microscope. *Nature*, 237:510, 1972.
- [22] D.W. Pohl, W. Denk, and M. Lanz. Optical stethoscopy: Image recording with resolution $\lambda/20$. *Appl. Phys. Lett.*, 44:651, 1984.
- [23] E. Betzig, J.K. Trautmann, T.D. Harris, J.S. Weiner, and R.L. Kostelar. Breaking the diffraction barrier: optical microscopy on a nanometric scale. *Science*, 251:1468, 1991.
- [24] E. Betzig, P.L. Finn, and S.J. Weiner. Combined shear force and near-field scanning optical microscopy. *Appl. Phys. Lett.*, 60:2484, 1992.
- [25] R. Toledo-Crow, P.C. Yang, Y. Chen, and M. Vaez-Iravani. Near-field differential scanning optical microscope with atomic force regulation. *Appl. Phys. Lett.*, 60:2957, 1992.
- [26] H. Raether. *Surface plasmons on smooth and rough surfaces and on gratings*. Springer-Verlag, Berlin, 1988.
- [27] S.A. Maier. *Plasmonics: Fundamentals and Applications*. Springer, New York, 2007.
- [28] G. Mie. Beitrage zur optik truber medien, speziell kolloidaler metallosungen. *Ann. D. Physik*, 25:377, 1908.

-
- [29] P. Debye. *Ann. d. Physik*, 30:57, 1909.
- [30] A. Sommerfeld. Über die fortpflanzung elektrodynamischer wellen langs eines drathes. *Ann. d. Physik und Chemie*, 67:233, 1899.
- [31] J. Zenneck. Über die fortpflanzung elektromagnetischer wellen langs einer ebenen leiterfläche und ihre beziehung zur drathlosen telegraphie, 1907.
- [32] R.H. Ritchie. Plasma losses by fast electrons in thin films. *Phy. Rev.*, 106:874, 1957.
- [33] A. Otto. Excitation of nonradiative surface plasma waves in silver by the method of frustrated total reflection. *Z. Physik*, 216:398, 1968.
- [34] E. Kretschmann and H. Raether. Radiative decay of non-radiativesurface plasmons excited by light. *Z. Naturforschung*, 23A:2135, 1968.
- [35] R.B.M. Schasfoort and J.T. Anna. *Handbook of Surface Plasmon Resonance*. Royal Society of Chemistry, London, 2008.
- [36] Fleischmann, P. J. Hendra, and A. J. McQuillan. Raman spectra of pyridine adsorbed at a silver electrode, 1974.
- [37] D.L. Jeanmaire and R. P. Van Duyne. Surface raman spectroelectrochemistry: Part i. heterocyclic, aromatic, and aliphatic amines adsorbed on the anodized silver electrode. *J. of Elec. Chem.*, 84:1, 1977.
- [38] K. Kneipp. Surface enhanced raman scattering. *Physics Today*, 60:40, 2007.
- [39] H.X. Xu, E.J. Bjerneld, M. Kall, and L. Borjesson. Spectroscopy of single hemoglobin molecules by surface enhanced raman scattering. *Phys. Rev. Lett.*, 83:4357, 1999.
- [40] W.L. Barnes, A. Dereux, and T.W. Ebbesen. Surface plasmon subwavelength optics. *Nature*, 424:824, 2003.
- [41] T.W. Ebbesen, H.J. Lezec, H.F. Ghaemi, T. Thio, and P.A. Wolff. Extraordinary optical transmission through sub-wavelength hole arrays. *Nature*, 391:667, 1998.

- [42] T.W. Ebbesen, C. Genet, and S.I. Bozhevolnyi. Surface plasmon circuitry. *Phys. Today*, page 44, May 2008.
- [43] A.V. Zayats, I.I. Smolyaninov, and A.A. Maradudin. Nano-optics of surface plasmon polaritons. *Phys. Rep.*, 408:131, 2005.
- [44] S. I. Bozhevolnyi, V. S. Volkov, J.-Y. Laluet, E. Devaux, and T. W. Ebbesen. Channel plasmon subwavelength waveguide components including interferometers and ring resonators. *Nature*, 440:508, 2006.
- [45] C. Genet and T.W. Ebbesen. Light in tiny holes. *Nature*, 445:39, 2007.
- [46] E. Altewischer, M.P. van Exter, and J.P. Woerdmann. Plasmon-assisted transmission of entangled photons. *Nature*, 418:304, 2002.
- [47] C. Kittel. *Solid State Physics*. Wiley, New York, 2002.
- [48] E.D. Palik. *Handbook of optical constants of solids*. Academic, London, 1985.
- [49] B. Hecht, H. Bielefeldt, L. Novotny, Y. Inouye, and D.W. Pohl. Local excitation, scattering and interference of surface plasmons. *Phys. Rev. Lett.*, 77:1889, 1996.
- [50] W.L. Barnes. Fluorescence near interfaces: the role of photonic mode density. *J. Mod. Opt.*, 45:661, 1998.
- [51] E. Kretschmann. Die bestimmung optischer konstanten von metallen durch anregung von oberflächenschwingungen. *Z. Physik*, 241:313, 1971.
- [52] A. Drezet, A. Hohenau, D. Koller, A. Stepanov, H. Ditlbacher, B. Steinberger, F.R. Aussensegg, A. Leitner, and J.R. Krenn. Leakage radiation microscopy of surface plasmon polariton. *Mat. Sci. and Eng. B*, 149:220, 2008.
- [53] H.J. Simon and J.K. Guha, 1976.
- [54] K.A. Willet and R.P. Van Duyne. Localized surface plasmon resonance spectroscopy and sensing. *Ann. Rev. Phys. Chem.*, 58:267, 2007.
- [55] V. Rastogi, S. Melle, O.G. Calderon, A.A. Garcia, M. Marquez, and O.D. Velev. Synthesis of light-diffracting assemblies from microspheres and

- nanoparticles in droplets on a superhydrophobic surface. *Adv. Mat.*, 20:4263, 2008.
- [56] A. Degiron, H.J. Lezec, N. Yamamoto, and T.W. Ebbesen. Optical transmission properties of a single subwavelength aperture in a real metal. *Opt. Comm.*, 239:61, 2004.
- [57] A. Degiron and T.W. Ebbesen. The role of localized surface plasmon modes in the enhanced transmission of periodic subwavelength apertures. *J. Opt. A: Pure Appl. Opt.*, 7:S90, 2005.
- [58] K.J. Klein Koerkamp, S. Enoch, F.B. Segerink, N.F. van Hulst, and L. Kuipers. Strong influence of hole shape on extraordinary transmission through periodic arrays of subwavelength holes. *Phys. Rev. Lett.*, 92:183901, 2004.
- [59] K.L. van der Molen, K.J. Klein Koerkamp, S. Enoch, F.B. Segerink, N.F. van Hulst, and L. Kuipers. Role of shape and localized resonances in extraordinary transmission through periodic arrays of subwavelength holes: experiment and theory. *Phys. Rev. B*, 72:045421, 2005.
- [60] B.E.A. Saleh and M.C. Teich. *Fundamentals of photonics*. Wiley, New York, 1991.
- [61] J.D. Jackson. *Classical Electrodynamics*. John Wiley & Sons, Hoboken, 1999.
- [62] H.A. Bethe. Theory of diffraction by small holes. *Phys. Rev.*, 66:163, 1944.
- [63] C.J. Bouwkamp. On the diffraction of electromagnetic waves by small circular disks and holes. *Philips. Res. Rep.*, 5:401, 1950.
- [64] C.J. Bouwkamp. Diffraction theory. *Rep. Progr. Phys.*, 17:35, 1954.
- [65] E. Popov and N. Bonod, M. Nevire, H. Rigneault, P.-F. Lenne, and P. Chaumet. Surface plasmon excitation on a single subwavelength hole in a metallic sheet. *Appl. Opt.*, 44:2332, 2005.
- [66] F.J. García-Vidal, E. Moreno, J.A. Porto, and L. Martín-Moreno. Transmission of light through a single rectangular hole. *Phys. Rev. Lett.*, 95:103901, 2005.

- [67] R. Gordon and A.G. Brolo. Increased cut-off wavelength for a subwavelength hole in a real metal. *Opt. Express*, 13:1933, 2005.
- [68] F.J. García-Vidal, L. Martín-Moreno, E. Moreno, L.K.S. Kumar, and R. Gordon. Transmission of light through a single rectangular hole in a real metal. *Phys. Rev. B*, 74:153411, 2006.
- [69] E. Popov, M. Nevire, A. Sentenac, N. Bonod, A.L. Fehrembach, J. Wenger, P.F. Lenne, and H. Rigneault. Single-scattering theory of light diffraction by a circular subwavelength aperture in a finitely conducting screen. *J. Opt. Soc. Am. A*, 24:339, 2007.
- [70] C. Obermuller and K. Karrai. Far field characterization of diffracting circular apertures. *Appl. Phys. Lett.*, 67:3408, 1995.
- [71] C. Obermuller, K. Karrai, G. Kolb, and G. Abstreier. Transmission radiated through a subwavelength-sized tapered optical fiber tip. *Ultramicroscopy*, 61:171, 1995.
- [72] F. Przybilla, A. Degiron, C. Genet, T.W. Ebbesen, F. de Lon-Prez, J. Bravo-Abad, F. J. García-Vidal, and L. Martín-Moreno. Efficiency and finite size effects in enhanced transmission through subwavelength apertures. *Opt. Exp.*, 16:9571, 2008.
- [73] U. Fano. Effects of configuration interaction on intensities and phase shifts. *Phys. Rev.*, 124:1866, 1961.
- [74] C. Genet, M.P. van Exter, and J.P. Woerdman. Fano-type interpretation of red shifts and red tails in hole array transmission spectra. *Opt. Commun.*, 225:331, 2003.
- [75] M. Sarrazin, J.-P. Vigneron, and J.-M. Vigoureux. Role of wood anomalies in optical properties of thin metallic films with a bidimensional array of subwavelength holes, 2003.
- [76] J. Bravo-Abad, L. Martín-Moreno, F.J. García-Vidal, E. Hendry, and J. Gomez Rivas. Transmission of light through periodic arrays of square hole: From a metallic wire mesh to an array of tiny holes. *Phys. Rev. B*, 76:241102, 2007.

- [77] M.J.A. de Dood, E. F. C. Driessen, D. Stolwijk, and M.P. van Exter. Observation of coupling between surface plasmons in index-matched hole arrays. *Phys. Rev. B*, 2008, 77.
- [78] A. Krishnan, T. Thio, T.J. Kim, H.J. Lezec, T.W. Ebbesen, P.A. Wolff, J. Pendry, L. Martín-Moreno, and F.J. García-Vidal. Evanescently coupled resonance in surface plasmon enhanced transmission. *Opt. Commun.*, 200:1, 2001.
- [79] W.L. Barnes, W.A. Murray, J. Dintinger, E. Devaux, and T.W. Ebbesen. Surface plasmon polaritons and their role in the enhanced transmission of light through periodic arrays of subwavelength holes in a metal film. *Phys. Rev. Lett.*, 92:107401, 2004.
- [80] E. Devaux, T.W. Ebbesen, J.C. Weeber, and A. Dereux. Launching and decoupling surface plasmons via micro-gratings. *Appl. Phys. Lett.*, 83:4963, 2003.
- [81] J.Y. Laluet, E. Devaux, C. Genet, T.W. Ebbesen, J.C. Weeber, and A. Dereux. Optimization of surface plasmons launching from subwavelength hole arrays: modelling and experiments. *Opt. Express*, 15:3488, 2007.
- [82] V. Mikhailov, G. Wurtz, J. Elliot, P. Bayvel, and A. V. Zayats. Dispersing light with surface plasmon polaritonic crystals. *Phy. Rev. Lett.*, 99:083901, 2007.
- [83] H.F. Ghaemi, Tineke Thio, D.E. Grupp, T.W. Ebbesen, and H.J. Lezec. Surface plasmons enhance optical transmission through subwavelength holes. *Phys. Rev. B*, 58:6779, 1998.
- [84] M. Sarrazin and J.P. Vigneron. Nonreciprocal optical reflection from a bidimensional array of subwavelength holes in a metallic film. *Phys. Rev. B*, 70:193409, 2004.
- [85] Y. Pang, C. Genet, and T.W. Ebbesen. Optical transmission through subwavelength slit apertures in metallic films. *Opt. Comm.*, 280:10, 2007.
- [86] U. Schrter and D. Heitmann. Surface-plasmon-enhanced transmission through metallic gratings. *Phys. Rev. B*, 58:15419, 1998.

- [87] Q. Cao and P. Lalanne. Negative role of surface plasmons in the transmission of metallic gratings with very narrow slits. *Phys. Rev. Lett.*, 88:057403, 2002.
- [88] D.E. Grupp, H.J. Lezec, T. Thio, and T.W. Ebbesen. Beyond the bethe limit: tunable enhanced light transmission through a single sub-wavelength aperture. *Adv. Mater.*, 11:860, 1999.
- [89] T. Thio, K.M. Pellerin, R.A. Linke, H.J. Lezec, and T.W. Ebbesen. Enhanced light transmission through a single subwavelength aperture. *Opt. Lett.*, 26:1972, 2001.
- [90] T. Thio, H.J. Lezec, T.W. Ebbesen, K.M. Pellerin, G.D. Lewen, A. Nahata, and R.A. Linke. Giant optical transmission of sub-wavelength apertures: physics and applications. *Nanotech.*, 13:429, 2002.
- [91] A. Degiron and T.W. Ebbesen. Analysis of the transmission process through single apertures surrounded by periodic corrugations. *Opt. Express*, 12:3694, 2004.
- [92] F.J. García-Vidal, H.J. Lezec, T.W. Ebbesen, and L. Martín-Moreno. Multiple paths to enhance optical transmission through a single subwavelength slit. *Phys. Rev. Lett.*, 90:213901, 2003.
- [93] H.J. Lezec, A. Degiron, E. Devaux, R.A. Linke, L. Martin-Moreno, F.J. García-Vidal, and T.W. Ebbesen. Beaming light from a subwavelength aperture. *Science*, 297:820, 2002.
- [94] F.J. García-Vidal, L. Martín-Moreno, H.J. Lezec, and T.W. Ebbesen. Focusing light with a single subwavelength aperture flanked by surface corrugations, 2003.
- [95] L. Martín-Moreno, F.J. García-Vidal, H.J. Lezec, A. Degiron, and T.W. Ebbesen. Theory of highly directional emission from a single subwavelength aperture surrounded by surface corrugations. *Phys. Rev. Lett.*, 90:167401, 2003.
- [96] D.E. Grupp, H.J. Lezec, and T.W. Ebbesen. Crucial role of metal surface in enhanced transmission through subwavelength apertures. *Appl. Phys. Lett.*, 77:1569, 2000.

- [97] T. Thio, H.F. Ghaemi, H.J. Lezec, P.A. Wolff, and T.W. Ebbesen. Surface-plasmon-enhanced transmission through hole arrays in Cr films. *J. Opt. Soc. Am. B*, 16:1743, 1999.
- [98] V. Halt, A. Benabbas, and J.-Y. Bigot. Optical response of periodically modulated nanostructures near the interband transition threshold of noble metals. *Opt. Express*, 14:2909, 2006.
- [99] F. Przybilla, A. Degiron, J.Y. Laluet, C. Genet, and T.W. Ebbesen. Optical transmission in perforated noble and transition metal films. *J. Opt. A: Appl. Opt.*, 8:458, 2006.
- [100] S.G. Rodrigo, F.J. García-Vidal, and L. Martín-Moreno. Influence of material properties on extraordinary optical transmission through hole arrays. *Phys. Rev. B*, 77:075401, 2008.
- [101] Y. Ekinici, H.H. Solak, and C. David. Extraordinary optical transmission in the ultraviolet region through aluminium hole arrays. *Opt. Lett.*, 32:172, 2007.
- [102] A. Degiron, H.J. Lezec, W.L. Barnes, and T.W. Ebbesen. Effects of hole depth on enhanced light transmission through subwavelength hole arrays. *Appl. Phys. Lett.*, 81:4327, 2002.
- [103] L. Martín-Moreno, F.J. García-Vidal, H.J. Lezec, K.M. Pellerin, T. Thio, J.B. Pendry, and T.W. Ebbesen. Theory of extraordinary optical transmission through subwavelength hole arrays. *Phys. Rev. Lett.*, 86:1114, 2001.
- [104] F.J. García de Abajo. Colloquium: light scattering by particle and hole arrays. *Rev. Mod. Phys.*, 79:1367, 2007.
- [105] K.L. van der Molen, F.B. Segerink, N.F. van Hulst, and L. Kuipers. Influence of hole size on the extraordinary transmission through subwavelength hole arrays. *Appl. Phys. Lett.*, 85:4316, 2004.
- [106] J.V. Coe, S.M. Williams, K.R. Rodriguez, S. Teeters-Kennedy, A. Sudnitsyn, and F. Hrovat. Extraordinary ir transmission with metallic arrays of subwavelength holes. 78:1384, 2006.

- [107] R. Gordon, D. Sinton, K.L. Kavanagh, and Alexandre G. Brolo. A new generation of sensors based on extraordinary optical transmission, 2008.
- [108] F.J. García-Vidal, L. Martín-Moreno, T.W. Ebbesen, and L. Kuipers. Light passing through subwavelength apertures.
- [109] A. Yu. Nikitin, D. Zueco, F.J. García-Vidal, and L. Martín-Moreno. Electromagnetic wave transmission through a small hole in a perfect electric conductor of finite thickness. *Phys. Rev. B*, 78:165429, 2008.
- [110] F.J. García de Abajo. Light transmission through a single cylindrical hole in a metallic film. *Opt. Express*, 10:1475, 2002.
- [111] J.P. Faroux and J. Renault. *Electromagnetisme 2*. Dunod, Paris, 1998.
- [112] P.B. Catrysse, H. Shin, and S. Fan. Propagating modes in subwavelength cylindrical holes. *J. Vac. Sci. Technol. B*, 23:2675, 2005.
- [113] C. Ropers, D.J. Park, G. Stibenz, G. Steinmeyer, J. Kim, D.S. Kim, and C. Lienau. Femtosecond light transmission and subradiant damping in plasmonic crystals. *Phys. Rev. Lett.*, 94:113901, 2005.
- [114] H. Liu and P. Lalanne. Microscopic theory of the extraordinary optical transmission. *Nature*.
- [115] A.-L. Baudrion, F. de Len Perez, O. Machboub, A. Hohenau, H. Ditlbacher, F.J. García-Vidal, J. Dintinger, T.W. Ebbesen, L. Martín-Moreno, and J.R. Krenn. Coupling efficiency of light to surface plasmon polariton for single subwavelength holes in a gold film. *Opt. Express*, 16:3420, 2008.
- [116] A. Roberts. Near-zone fields behind circular apertures in thick, perfectly conducting screens. *J. Appl. Phys.*, 65:2896, 1989.
- [117] A. Roberts. Electromagnetic theory of diffraction by a circular aperture in a thick, perfectly conducting screen. *J. Opt. Soc. Am.*, 4:1970, 1987.
- [118] F.J. García de Abajo and J.J. Saenz. Electromagnetic surface modes in structured perfect-conductor surfaces. *Phys. Rev. Lett.*, 95:233901, 2005.

- [119] S. Collin, F. Pardo, and J.-L. Pelouard. Waveguiding in nanoscale metallic apertures. *Op. Express*, 15:4310, 2007.
- [120] J.A.H. van Nieuwstadt, M. Sandtke, R.H. Harmsen, F.B. Segerink, J.C. Prangersma, S. Enoch, , and L. Kuipers. Strong modification of the nonlinear optical response of metallic subwavelength hole arrays. *Phys. Rev. Lett.*, 97:146102, 2006.
- [121] J. Kindler, P. Banzer, S. Quabis, U. Peschel, and G. Leuchs. Waveguide properties of single subwavelength holes demonstrated with radially and azimuthally polarized light. *Appl. Phys. B*, 89:517, 2007.
- [122] W. Groner, J. W. Winkelman, A. G. Harris, C. Ince, G.J. Bouma, K. Messmer, and R.G. Nadeau. Orthogonal polarization spectral imaging: A new method for study of the microcirculation. *Nat. Medicine*, page 1209, 1999.
- [123] R.E. Levenson and C.C. Hoyt. Spectral imaging and microscopy. *Am. Lab.*, 32:26, 2000.
- [124] M.E. Dickinson, G. Bearman, S. Tille, R. Lansford, and S.E. Fraser. Multispectral imaging and linear unmixing add a whole new dimension to laser scanning fluorescence microscopy. *Biotechniques*, 31:1272, 2001.
- [125] J.O. Stenflo and H. Povel. Astronomical polarimeter with 2d detector arrays. *Appl. Opt.*, 24:3893, 1985.
- [126] D.A. Landgrebe, S.B. Serpico, M.M. Crawford, and V. Singhroy. Introduction to the special issue on analysis of hyperspectral image data. *IEEE T Geosci. Remote*, 39:1343, 2001.
- [127] Y.Garini, I.T. Young, and G. McNamara. Spectral imaging: principles and applications. *Cytometry*, 69A:735, 2006.
- [128] J.S. Tyo, D.L. Goldstein, D.B. Chenault, and J. Straw. Review of passive imaging polarimetry for remote sensing applications. *Appl Opt.*, 45:5453, 2006.
- [129] A. R. Harvey and D.R. Fletcher-Holmes. High-throughput snapshot spectral imaging in two dimensions. *Proc. SPIE*, 4959:46, 2003.

- [130] <http://www.foveon.com/>.
- [131] B.E. Bayer. Colour imaging array. US Patent, 1976. 3.971.065.
- [132] www.foveon.com.
- [133] T. Ishi, J. Fujikata, and K. Ohashi. Large optical transmission through a single subwavelength hole associated with a sharp-apex grating. *Jpn. J. Appl. Phys.*, 44:L170, 2005.
- [134] O. Mahboub and E. Laux et al. in preparation.
- [135] F. Yang and J.R. Sambles. Resonant transmission of microwaves through a narrow metallic slit. *Phys. Rev. Lett.*, 89:063901, 2002.
- [136] X. Jiao, P. Wang, L. Tang, Y. Lu, Q. Li, D. Zhang, P. Yao, H. Ming, and J. Xie. Fabryperot-like phenomenon in the surface plasmons resonant transmission of metallic gratings with very narrow slits. *App. Phys. B*, 80:301, 2005.
- [137] S. Astilean, Ph. Lalanne, and M. Palamaru. Light transmission through metallic channels much smaller than the wavelength. *Opt. Comm.*, 175:265, 2000.
- [138] P. Lalanne and J.P. Hugonin. Interaction between optical nano-objects at metallo-dielectric interfaces. *Nat. Physics*, 2:551, 2006.
- [139] H.F. Shouten, N. Kuzmin, G. Dubois, T.D. Visser, G. Gbur, P.F.A. Alkemade, H. Blok, G.W. 't Hooft, D. Lenstra, and E.R. Eliel. Plasmon-assisted two-slit transmission: Young's experiment revisited. *Phys. Rev. Lett.*, 94:053901, 2005.
- [140] R.B. Merrill. Colour separation in an active pixel cell imaging array using a triple-well structure. US Patent, 1999. 5.965.875.
- [141] M. Descour and E. Dereniak. Computed tomography imaging spectrometer - experimental calibration and reconstruction results. *Appl. Opt.*, 34:4817, 1995.
- [142] T. Ishi, J. Fujikata, K. Makita, T. Baba, and K. Ohashi. Si nano-photodiode with a surface plasmon antenna. *Jpn J. Appl. Phys.*, 44:L364,.

- [143] E. Laux, C. Genet, T. Skauli, and T.W. Ebbesen. Plasmonic photon sorters for spectral and polarimetric imaging. *Nat. Photonics*, 2:161, 2008.